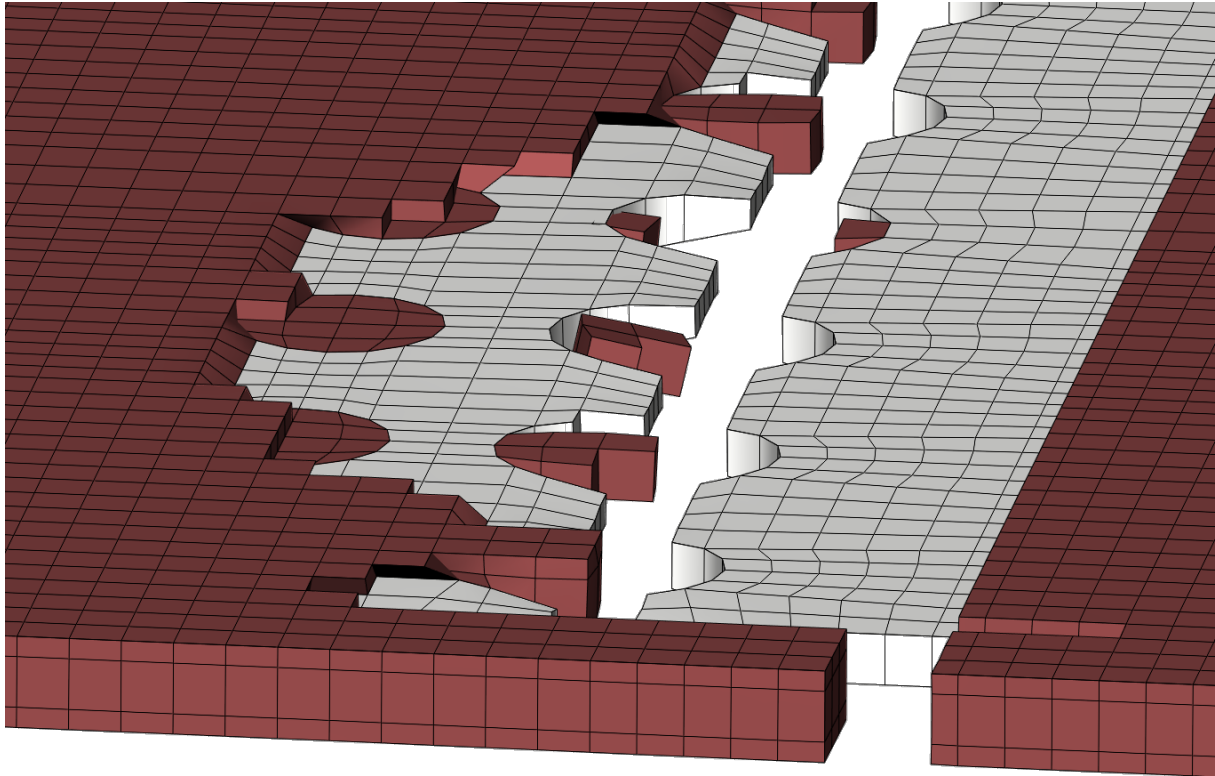




CHALMERS
UNIVERSITY OF TECHNOLOGY



FEM the Wood Revolution

In-depth FE-analysis of a wood-glue-steel joint in a wind turbine tower

Master's thesis in Master's Program MPAEM & MPAME

EMIL BORGLUND ASPLER
LINNÉA JERN

MASTER'S THESIS 2019:IMSX30

FEM the Wood Revolution

In-depth FE-analysis of a wood-glue-steel joint in a wind turbine tower

EMIL BORGLUND ASPLER
LINNÉA JERN



CHALMERS
UNIVERSITY OF TECHNOLOGY

Department of Industrial and Materials Science
Alten Sverige AB, Modvion
CHALMERS UNIVERSITY OF TECHNOLOGY
Gothenburg, Sweden 2019

FEM the Wood Revolution
In-depth FE-analysis of a wood-glue-steel joint in a wind
turbine tower
EMIL BORGLUND ASPLER, LINNÉA JERN

© EMIL BORGLUND ASPLER, 2019.

© LINNÉA JERN, 2019.

Supervisors: Francesc Corredera, Alten Sverige AB; Erik Dölerud, Modvion
Examiner: Ragnar Larsson, Industrial and Materials Science

Master's Thesis 2019:30
Department of Industrial and Materials Science
Chalmers University of Technology
SE-412 96 Gothenburg
Telephone +46 31 772 1000

Cover: Fracture of the glue and steel plate. Simulation.

Typeset in L^AT_EX
Printed by someone
Gothenburg, Sweden 2019

FEM the Wood Revolution

In-depth FE-analysis of a wood-glue-steel joint in a wind turbine tower

EMIL BORGLUND ASPLER, LINNÉA JERN

Department of Industrial and Materials Science

Chalmers University of Technology

Abstract

Modvion is a company that develop 150 m tall wind turbine towers made out of modules of Engineered Wood Products (EWP), specifically Laminated Veneer Lumber (LVL). One of the big challenges in their design is the joining of the modules, which is the focus of this thesis. The joint design was given from the beginning along with physical test data from tensile tests performed at Research Institutes of Sweden (RISE). In this thesis a Finite Element (FE)-model of the joint was created, with the aim to replicate the response obtained from the physical tensile tests using simulations. The main goal was to use the FE-model in order to describe the inner mechanics of the joint.

The joining of two LVL panels is made with Loctite CR 421 Purbond and a perforated steel plate. The joint and its materials are studied using physical testing and the commercial softwares ANSA as pre-processor, Abaqus Unified FEA as solver, and META as post-processor. The material parameters for the wood given by data sheets provided by the manufacturer are compared to physical test data. Remaining material parameters and simulation parameters are calibrated through material validation and parameter studies. Finally a small study was performed on whether the joint can be improved by making modifications to the perforated steel plate. The effects of these modifications were studied in order to find the critical areas of the joint.

The obtained results show that the number of holes in the steel plate are critical for the performance of the joint when it comes to its tensile strength. This is because the holes enables the glue to create adhesive anchors that facilitates the stress transfer from the glue to the steel. Since the steel plate is the component of the joint that can withstand the highest amount of loading, the efficiency of the stress transfer is crucial in order to prevent the glue from breaking entirely at relatively small loads, which would result in a lower ultimate tensile strength of the joint.

Although, some insecurities remains in the implementation of the FE-model, the results in this thesis can be used as a foundation for future research on this topic.

Keywords: Wood, FEA, FEM, LVL, Windpower, Gluejoint.

Acknowledgements

We would first like to thank Alten and our colleagues there for all the help and support, making it fun and interesting performing our thesis. In particular, we would like to thank our closest supervisor Francesc Corredera and the rest of the biotech team at Alten.

Mikael Almquist who gave us the opportunity to perform our thesis at Alten, and for managing us throughout the thesis.

Modvion and Chief Technology Officer Erik Dölerud who has provided the task and given us all the physical test material.

Our examiner Ragnar Larsson, who has advised us and provided useful input, that really helped us in the journey of achieving the final results.

Finally we would like to thank all the friends and teachers at Chalmers that has helped us through our entire education. Also a thank you to SSAB who willingly gave us stress-strain data for their steel.

May the Force be with you.

Gothenburg, June 10, 2019

Linnéa Jern, Emil Borglund Aspler

Contents

List of Figures	xi
List of Tables	xv
Glossary	xvii
Glossary	xvii
Acronyms	xvii
1 Introduction	1
1.1 Background	1
1.2 Aim	3
1.3 Limitations	3
1.4 Specification of issue under investigation	3
1.5 Societal, ethical and ecological aspects	4
1.6 Previous academic work on the topic	4
2 Theory	5
2.1 Basic introduction to wood	5
2.2 The joint developed by Modvion	7
2.2.1 Laminated Veneer Lumber, LVL	8
2.3 The joining of the wooden modules	9
2.3.1 Adhesive used in the joint	9
2.4 Similar projects	10
2.5 Softwares	10
2.5.1 Pre-processing	10
2.5.2 FEA solver	11
2.5.3 Post-processing	11
2.6 Coordinate systems	11
2.7 Constitutive modeling of the materials	12
2.7.1 Elasticity for orthotropic and isotropic materials	12
2.7.2 Elasto-plasticity for the glue and the steel	14
2.7.2.1 Isotropic hardening plastic behaviour	14
2.8 Fracture modeling of the glue and the steel	16
2.8.1 Element deletion	18
2.9 Simulation set-up	19
3 Analysis and validation of material data	21
3.1 Physical tensile test data for the joint	21

3.2	Data obtained from research and tests	23
3.2.1	Wood tensile tests of single veneers	25
3.2.2	Glue tensile tests	30
3.2.3	Cross section cuts of the test samples	31
3.3	Recreation of the material behaviours	34
3.3.1	Material model for the wood	34
3.3.2	Material model for the steel	38
3.3.3	Material model for the glue	39
4	Simplified model	41
4.1	Type of contacts between the materials	42
4.1.1	Traction-separation model for cohesive contacts	44
4.2	Material models for the glue	47
4.3	Different types of analyses	48
4.3.1	Calibration of simulation parameters	49
5	Full model	53
5.1	Steel plate only	54
5.2	Tuning of glue material parameters	56
5.3	Mesh	58
6	Modified steel plate	61
6.1	Simulation results	62
6.1.1	Conclusion	64
7	Conclusion	65
7.1	Further work	66
7.2	Challenges	66
	Bibliography	67
A	Appendix 1	I
A.1	Stress distributions	I

List of Figures

1.1	Ashby chart for comparing Yield strength against density. The black line has a slope of 1,5 representing the material index for a beam in bending.	2
2.1	The principal axes of wood [1].	5
2.2	Refinement process from log to EWP [2].	6
2.3	Isometric view of the full model.	7
2.4	Explosion view of the full model.	7
2.5	Laminated Veneer Lumber, LVL. Observe the ply lay-up that is the same as in Figure 2.6, although the bottom half-ply is missing in this picture.	8
2.6	Illustration of the ply lay-up in this specific Kerto-Q LVL, where the fibre directions are illustrated using arrows.	8
2.7	A picture of The TimberTower located in Germany [3].	10
2.8	The coordinate system in relation to the fibre orientation of the face ply.	11
2.9	Illustration of the elastic and plastic strain in a stress-strain curve for a inelastic perfectly plastic material [4]. (L) stands for plastic loading and (U) stands for elastic unloading.	14
2.10	The three different fracture modes from left to right: Mode I Opening, Mode II sliding, Mode III tearing.	16
2.11	Tension test showing brittle (<i>a</i>), and ductile (<i>b</i>) behavior [5]. The <i>y</i> is the yield stress, <i>u</i> is ultimate strength and <i>f</i> stands for fracture.	17
3.1	The fracture in the first row of holes.	21
3.2	The tensile test set-up at RISE.	22
3.3	Test data from full joint tests performed at RISE. The two lower subfigures are the same data with different scopes on the x-axis.	23
3.4	Stress-strain data for the steel, STRENX 700 MC E manufactured by SSAB.	24
3.5	The test set up with a wide specimen in the TRAM UTC 50 kN.	25
3.6	Drawing of the narrow tensile test specimen.	26
3.7	Drawing of the wide tensile test specimen.	26
3.8	The stress-strain behaviour obtained from the tests. Both subfigures has the same axes, however Batch 1 is measured without extensometer and batch 2 with.	28
3.9	Same data as Figure 3.8 above, with all data visible. Curves are cut at the maximum stress values.	28
3.10	The stress-strain behaviour across fibre. Curves are cut at the maximum stress values.	29
3.11	Stress-strain plot of the glue tests.	30
3.12	Cross-section sample cut overview.	31

3.13	Sample 4, main side cut scans. Each cut is 30 mm apart. Sample 4 has been tested for fatigue at more than 30 000 cycles, where the load is unknown to us.	32
3.14	Sample 4, prim side cut scans.	32
3.15	Sample 5, main side cut scans. Each cut is 30 mm apart. Sample 5 has been tested in pure tension and broke at 269 kN.	32
3.16	Sample 5, prim side cut scans.	33
3.17	Sample 10, main side cut scans. Each cut is 30 mm apart. Sample 10 has been tested for fatigue in tension/compression at 165 kN and broke after 3250 cycles.	33
3.18	Sample 10, prim side cut scans.	33
3.19	Comparison between the LVL-panel with and without considering the layers. x, y, and z-direction.	36
3.20	Comparison between the LVL-panel with and without considering the layers. Shear directions.	37
3.21	Stress-strain curve for STRENX 700 MC E and corresponding simulations.	38
3.22	The stress-strain curve for two different glue material models obtained using dynamic explicit analysis.	40
4.1	The simplified model, which is a tenth of the full joint.	41
4.2	Explosion view of the simplified model.	42
4.3	Different types of contacts between the glue and the steel in the simplified model.	43
4.4	Typical traction-separation response	44
4.5	Stress-strain curve with progressive damage degradation [6].	45
4.6	The force-local displacement response obtained from the simulations with the different kind of contact interpretations	46
4.7	Comparison of different glue material models, compared to the physical test data.	47
4.8	Simulation results from static implicit and dynamic explicit with different values of the mass scaling factor, f^2 , compared to the physical test data.	48
4.9	The ratio between the kinetic energy and the internal energy. In order to ensure that there is no significant change to the solution the ratio should preferably be less than 10%.	49
4.10	Different simulation parameters for dynamic explicit compared to test data.	50
4.11	Comparison of computation times and the ratio between kinetic and internal energy for different simulation parameters for dynamic explicit.	50
5.1	Illustration of the full-scale model.	53
5.2	Results from simulations with drastically changed glue properties. The red line is the original data sheet properties.	54
5.3	Simulation results for the steel plate only, without glue and wood. Displacement was measured both locally (45 mm from the horizontal symmetry line) and globally (at the ends where the boundary conditions are applied).	55
5.4	An illustration of how the local and the global deformations are measured on the steel plate	55
5.5	The different glue plasticity levels that were tested. The real curve is probably smooth.	56

5.6	Simulation results at the different glue plasticity levels. Also the brittleness of the steel was altered.	57
5.7	Mesheres of the full-scale model.	58
5.8	Mesheres of the full-scale model.	59
5.9	Simulation results for refined meshes compared to test results. Some simulations were not finished due to limitations in computational power.	59
5.10	After fracture. Clearly shows where the mesh has been refined and how it affects the glue failure. In the refined zone, some glue remains after one layer breaks.	60
6.1	The different modifications of the hole density in the steel plate. The dot/dash-line represents the horizontal symmetry line of the model. Drawing shows only a section of the width of the plates.	62
6.2	The different modifications of the hole density in the steel plate, compared to test data and simulation of the original.	62
6.3	Modified plate A. Fracture in glue initiates at split line and propagates to the middle of the plate.	63
6.4	Modified plate B. Fracture in glue initiates at split line and propagates further than the middle of the plate.	63
6.5	Simulated effects on maximum load dependent on Area ratio and Hole ratio.	64
A.1	Step 1	I
A.2	Step 2	II
A.3	Step 3	II
A.4	Step 4	III
A.5	Step 5	III
A.6	Step 6	IV
A.7	Step 7	IV
A.8	Step 8	V
A.9	Step 9	V
A.10	Step 10	VI
A.11	Step 11	VI
A.12	Step 12	VII
A.13	Step 13	VII

List of Tables

3.1	Mechanical properties from data sheets of the materials considered.	24
3.2	Overview of the tests on the Kerto-Q plies.	29
3.3	Summary of the tests.	29
3.4	Dimensions of the glue test specimens. All units are mm.	30
3.5	Mechanical properties used for a single wooden veneer and for homogeneous wood panels.	35
4.1	Mechanical properties used to define the cohesive contact behaviour between the wood and the glue	46
5.1	Simulation results for different glue plasticity levels.	57

Glossary

dodecagonal Twelve-sided polygon

Holz-Stahl-Kleverbinding (German) Wood-steel adhesive connection

STRENX 700 MC E SSAB Hot rolled steel with nominal yield strength at 700 MPa

Acronyms

CAD Computer Aided Design

CAE Computer Aided Engineering

CFD Computational Fluid Dynamics

CLT Cross Laminated Lumber

EWP Engineered Wood Products

FE Finite Element

FEA Finite Element Analysis

HSK Holz-Stahl-Kleverbinding

LVL Laminated Veneer Lumber

RISE Research Institutes of Sweden

1

Introduction

1.1 Background

In 2018, the CO₂ emissions reached an all-time high, increasing about 2,7% compared to 1,6% the previous year [7]. In order to prevent further increase of the CO₂ emissions, there is a great need for faster and stronger actions in order to address the accelerating climate change. One way of doing this, is to invest in more renewable energy sources, such as wind power. The perks with using renewable energy is that they produce neither greenhouse gases, which causes climate change, nor polluting emissions [8].

However, no renewable energy source is entirely green. During manufacturing of traditional wind power turbines and towers, hundreds of tons of steel are used, which consumes an enormous amount of energy [9]. To tackle this problem, a company called Modvion have started to develop wind power towers constructed in wood.

Modvion develops tall wooden towers to keep up the development of increasing cost-efficiency in wind power. Traditionally, wind turbine towers are made of steel, but it becomes incrementally inefficient with rising heights, since more material needs to be added at the foundation and the base diameter increases, making it costly and difficult to transport. Wood, on the other hand, has a higher strength to weight ratio than steel, which makes the design lighter and cheaper. Figure 1.1 clearly shows how softwood has a better strength to weight ratio than low alloy steel in the case of a beam in bending. Also, the price per kilogram is approximately the same for wood and steel, but since the wood has a lower density resulting in a lower mass needed to obtain the same strength as for steel, it is cheaper in the end.

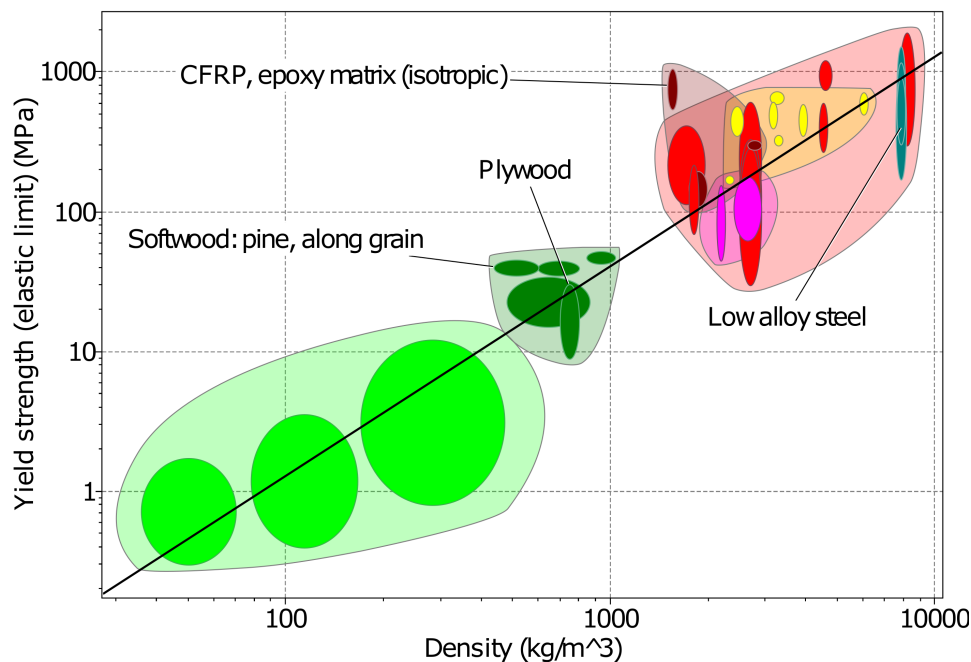


Figure 1.1: Ashby chart for comparing Yield strength against density. The black line has a slope of 1,5 representing the material index for a beam in bending.

Since the tower developed by Modvion is constructed in modules, it is possible to assemble it on the construction site, saving an enormous amount of money in transportation costs. Furthermore, the production of wooden towers consumes less energy compared to steel, resulting in decreased CO₂ emissions during production.

Conventional tower construction using steel, have reached the end of the road. Using the development in Engineered Wood Products (EWP), Modvion have been able to design towers with steep cost advantages that also reduces CO₂ in the atmosphere while being produced. Using EWP, higher towers than traditionally can be built using less material, which will result in more generated power, since increasing heights are being accessible due to the properties of the wood. Not only can the wind turbines with greater height take advantage of better wind resources due to its height, it is also possible to have longer blades on the wind turbine, which increases the capacity as well [10]. The wind power industry have long been struggling with imperfect alternatives to keep towers transportable, since higher towers needs costly thickening of metal walls and base diameter, making them more difficult to transport and the modular assemblies that exists are rather inefficient. Furthermore, steel and concrete industries alone stand for 6 % and 8 % of the world CO₂ emissions, respectively, and hence have a significant negative impact on the environment [11, 12].

The challenges with wood are still many. Joining of the modules is one of the main remaining challenges, where there is a lack of research and knowledge when it comes to the actual mechanical behaviour inside the joint, and also when it comes to Finite Element Analysis (FEA) of the joints. Bolted joints with steel plates and glued joints are some traditional ways of joining wood in large structures. This thesis will focus on joining the wooden modules using glue and steel plates.

1.2 Aim

The aim of this master thesis is to facilitate the construction of the wooden tower by developing an advanced finite element model for in-depth analysis of the inner joint mechanics. The ultimate goal will be to reproduce laboratory test results and understand the mechanical behaviour inside the joint during pure tension. This knowledge could later be used to propose design improvements of the joint.

1.3 Limitations

The project will only consider the types of materials and geometries provided by Modvion, which they have developed and tested. The software ANSA will be used to build models of the inner joint that is to be analysed, and Abaqus Unified FEA will be used to perform the finite element analysis. The load case that will be investigated is pure tension.

The thesis will be performed at Alten Sweden AB in Gothenburg, which is a consultancy company that develop and deliver expertise for world-leading companies through dedicated technology- and IT-consultants. The project will be performed during the spring of 2019.

1.4 Specification of issue under investigation

A design for a 150 m tall wind turbine tower constructed from EWP has been proposed by Modvion. The design is modular and comprised of several panels fitted together to form a tower. This thesis aims at in-depth analysis of the joints holding the panels together. The panels are made of Laminated Veneer Lumber (LVL) which is joined together by glue and steel plates. LVL can be interpreted as unidirectional plywood. Several aspects and load cases affect these joints, although to limit the scope, this thesis will only focus on one of the most critical load case; pure tension.

Joint solutions have recently been developed and tested by Modvion. Strength tests, including fatigue, have been carried out at Research Institutes of Sweden (RISE) institute facilities in Borås, and the remaining task is to create a model that enables recreation of these tests by simulations. The questions that are to be answered during the project are:

- Is our model representative?
- Are the material parameters provided by the company that develops the LVL representative?
- Where is the weak spot in the joint? What component of the joint fails first?
- Is the design of the joint optimal? Why? How can it be improved?
- Why are the results from Modvion's tests so good? Why is this a good joint?

1.5 Societal, ethical and ecological aspects

By constructing wind power towers in wood instead of steel, the CO₂ emissions during production will be reduced as well as the CO₂ already in the atmosphere will decrease due to increased planting of trees. Hence, this will have a positive effect on the environment and thus the society as a whole. Therefore this project should be considered as positive in a societal, ethical, and ecological point of view.

1.6 Previous academic work on the topic

During Modvion's relatively short history there has been a few Master's thesis done on the topic. Álvarez and Fernández [13] started in 2016 and made a thesis with the title *Conceptual design and FE analysis of a Cross Laminated Lumber (CLT) wind turbine tower*. The year after, Steen [14] made a thesis with the title *Structural Design of a Wooden Wind Tower Structure*. Both these have been focusing on the overall design of the tower while this thesis focus in detail on the glue joints.

More in general, there is plenty of academic work published on wood structures and glue joints. Some of which are cited in this report. One highly relevant publication to this one is a Master Thesis written by Blaženka Jeleč at TU Graz [15]. The thesis is written in German and is mostly focusing on experiments.

2

Theory

In this chapter, the theory of some major concepts in the project are explained. This includes; the materials used in the joint, the used software, a summary of previous related work, and the theory which lies as a foundation to the FEA performed in Abaqus Unified FEA.

2.1 Basic introduction to wood

The tower itself is, as mentioned, constructed in wood. Wood is an orthotropic material, which means that it has unique and independent properties in three mutually perpendicular directions, which are longitudinal, radial and tangential [1]. The longitudinal direction is parallel to the fibre direction of the wood, the radial direction is parallel to the growth rings, and the tangential direction is perpendicular to the grain and tangent to the growth rings. The different directions and their relation to the fibre direction and the growth rings can be seen in Figure 2.1.

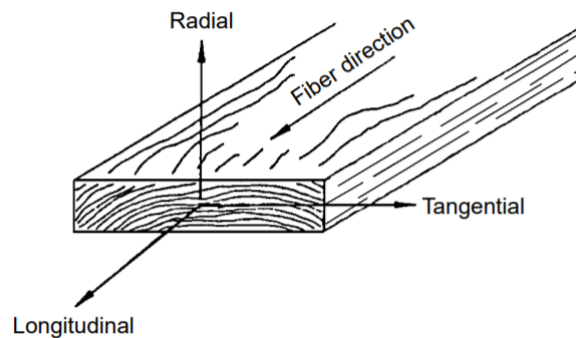


Figure 2.1: The principal axes of wood [1].

Wood species can be divided into softwood and hardwood. It is easy to think that the difference between these kind of trees is that softwood is a softer material (less dense) and that hardwood is a harder material (more dense), but this isn't always the case. One example is balsa wood, which is considered as hardwood despite being one of the lightest, least dense woods there is [16]. The distinction between softwood and hardwood is actually made botanically in terms of their reproduction, and not their appearance and end use as one may think [17, 18]. Both softwood and hardwood reproduce using seeds, but the structure of the seeds varies. Softwoods are gymnosperms, which means that

their seeds fall to the ground as they are without any coverage. Hardwoods on the other hand are angiosperms, which means that they produce seeds with some type of covering, such as an apple [17, 16]. Another difference is that angiosperms often lose their leaves during cold weather, while gymnosperm trees keep their leaves all year round. There are also mechanical differences between these two kinds of wood. Softwood are most often lighter and have high tensile strength but low shear strength, while hardwoods are heavier and have high tensile strength as well as shear strength [18]. Another difference between these two is that the softwood grows faster than hardwood and is therefore less expensive, which makes it an attractive construction material.

In construction, it is common to use Engineered Wood Products, known as EWP, which is man-made wood manufactured by binding veneers of wood together using an adhesive. By orienting the layers of veneers in different directions the final product obtains different material properties. EWP are used in order to overcome weaknesses of solid wood and obtaining a material with better properties. EWP also makes it possible to take advantage of low-quality raw material resulting in a material with higher added value [19]. The general concept of EWP is to cut the wood into smaller pieces and then re-assemble the pieces in order to make tailor-made structural members. The production process can be seen in Figure 2.2. The resulting products are more homogeneous with less variability. There are many different types of EWP, such as Plywood, CLT and Laminated Veneer Lumber (LVL). LVL is the chosen material used in the wind power tower developed by Modvion.

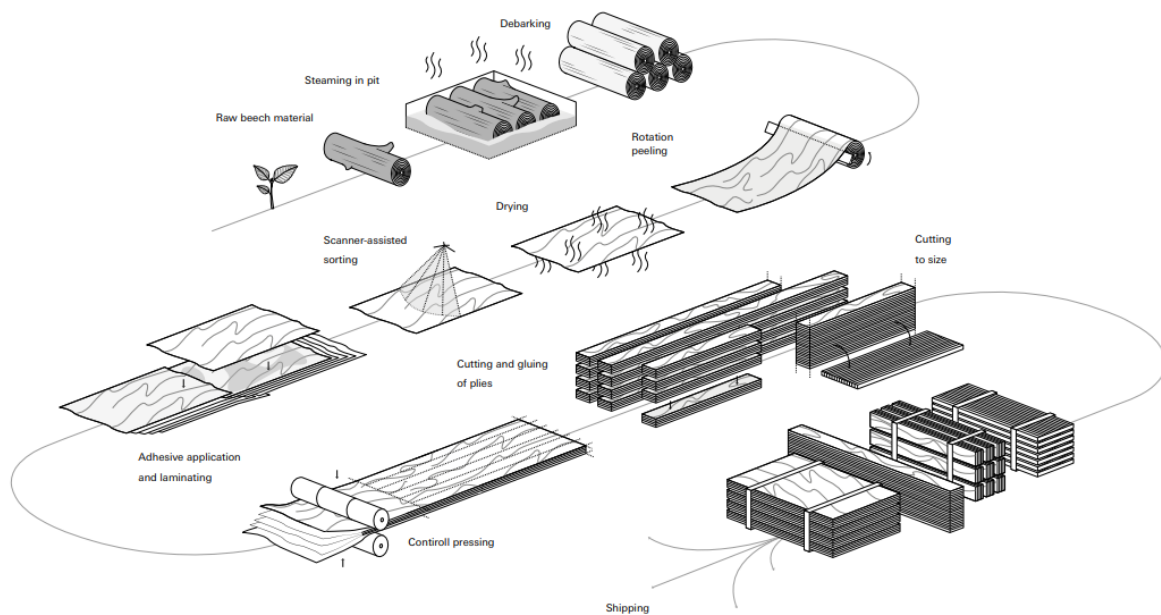


Figure 2.2: Refinement process from log to EWP [2].

2.2 The joint developed by Modvion

In Figures 2.3 and 2.4, the full test joint studied in this thesis can be seen. This is the joint that Modvion has performed tests on at RISE facilities with respect to tensile strength and fatigue limit. The joint consists of wood, glue and a perforated steel plate, which are described more in detail in the following subsections. Furthermore, steel compression plates have been added between the two wood components in order to prevent the fibres of the wood from intersecting during compression. In order to be able to fasten the joint when testing it, one connector at each end of the joint have been added, which are then mounted to the test machine using bolts, see Figure 2.4.

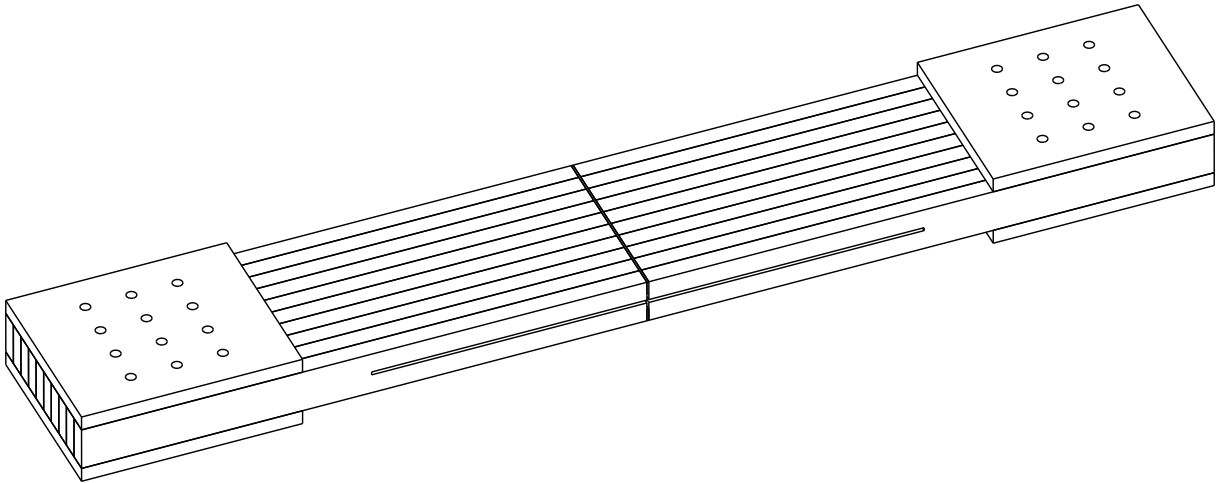


Figure 2.3: Isometric view of the full model.

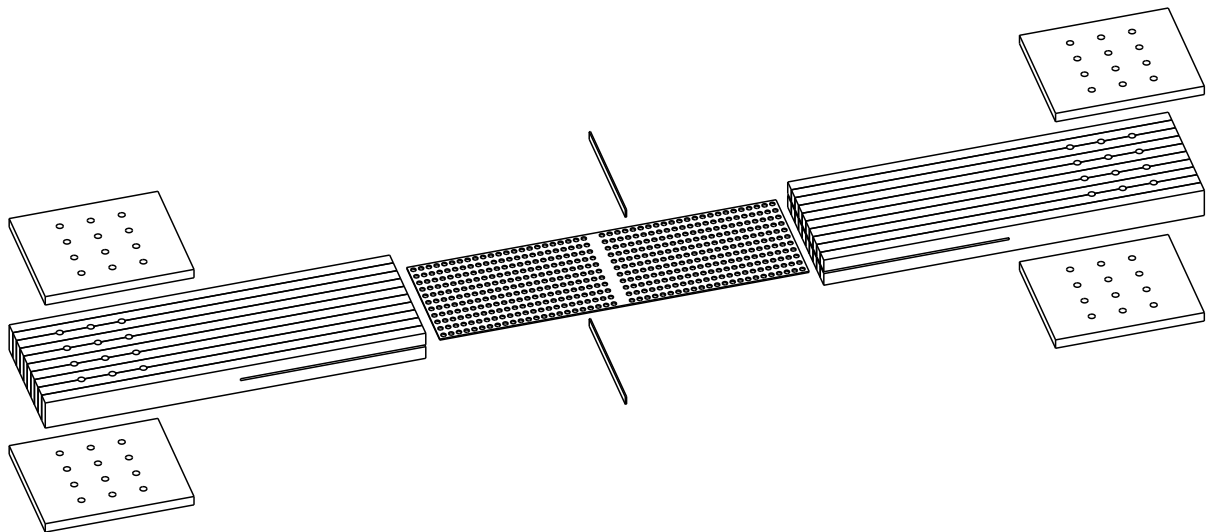


Figure 2.4: Explosion view of the full model.

2.2.1 Laminated Veneer Lumber, LVL

As mentioned, the tower developed by Modvion is made of a wooden material called LVL. It consists of cross-bonded veneers glued together, see Figure 2.5. Roughly one fifth of the veneers in the panels are glued crosswise, which gives LVL its excellent properties [20]. The type of LVL that Modvion uses is the Kerto Q-panel with thickness 24 mm [21, 22]. The Kerto Q-panel is load-bearing, bracing and dimensionally stable, and can be used for the most demanding structures, which makes it a perfect material for building high towers.



Figure 2.5: Laminated Veneer Lumber, LVL. Observe the ply lay-up that is the same as in Figure 2.6, although the bottom half-ply is missing in this picture.

The wood components of the joint consists of 10 LVL panels glued together, where each LVL panel is 24 mm and consists of nine softwood veneers cross-bonded with weather- and boil-resistant phenol formaldehyde adhesive. The configuration of the veneers is illustrated in Figure 2.6 seen from above. The outermost veneers have a thickness of 1,5 mm and the veneers located in between these are 3 mm thick.

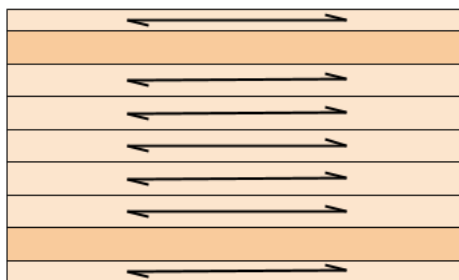


Figure 2.6: Illustration of the ply lay-up in this specific Kerto-Q LVL, where the fibre directions are illustrated using arrows.

Due to the crosswise veneers, the transverse strength and stiffness of the panel is enhanced, making it suitable as both horizontal and vertical bearer in various construction applications [22]. LVL is now considered to be the best EWP in terms of technology, reliability and performance [23]. LVL has some unique strength characteristics, for example its bending strength is twice as high than that of solid spruce, and its modulus of elasticity is 24 % greater. Due to its laminated structure and production technology, it is a material with homogeneous symmetrical structure that does not change its performance over its entire service life [23].

2.3 The joining of the wooden modules

In order to connect the wood modules in the wind power tower, Modvion uses a connection inspired by a wood joining method called the Holz-Stahl-Kleverbinding (HSK) system. The HSK system was developed by a German engineer named Leander Bathon [24] in the beginning of the 21st century. The connector is used to connect steel elements to wood or to connect two wood components together. The connector consists of a perforated steel plate and a corresponding adhesive [25]. The wood, in this case the LVL, is cut parallel to the fibres where the steel plate is inserted, see the line on the side of the joint in Figures 2.3 and 2.4. The cavity is then filled with the adhesive through a small hole in the side of the joint, rigidly connecting the two wood components. The holes in the metal plate acts as adhesive anchors, which enables the connection to withstand enormous forces. The metal plate is designed in a way that ensures that, in the event of failure, the steel plate begins to yield before the wood cracks [24, 25].

In order to prevent the steel plate from moving when inserting the glue, small steel holders have been added to keep the plate in position. The steel used in the joint is called STREX 700 MC E, which is a hot-rolled structural steel made for cold forming, with a minimum yield strength of 700 MPa for stronger and lighter structures.

2.3.1 Adhesive used in the joint

The most commonly used glue in the HSK system, which also is the glue that is used in the joint developed by Modvion, is Loctite CR 421 Purbond, which is a two-component polyurethane based glue made by Henkel [26]. The glue is specifically made for bonding threaded rods and steel rebar into structural timber components. Some of the mechanical properties of the glue can be found in Table 3.1, and the full data sheet can be found on Henkel's website [26].

2.4 Similar projects

Modvion is not the only company developing wind turbine towers that uses EWP as the main construction material. TimberTower is a good example of another tower, which is actually the worlds first wooden wind turbine tower and is located in Germany [27], see Figure 2.7. The tower is 100m high, made as a linked system of glued CLT panels and generates as much as 1,5 MW. The tower is manufactured off-site and then transported using standard containers and assembled on-site. The assembled tower is a closed and hollow body with hexagonal, octagonal or dodecagonal cross sections. To protect the tower from seasonal factors, the tower is covered in paint [3]. The wooden modules in the TimberTower are connected using the HSK-system. The tower developed by Modvion is inspired by the TimberTower, but with some improving modifications which enables the tower to reach larger heights resulting in higher generated power.



Figure 2.7: A picture of The TimberTower located in Germany [3].

2.5 Softwares

In this project, a number of commercial softwares were used to model and simulate the given problem. The three main softwares were ANSA as pre-processor, Abaqus Unified FEA as solver, and META as post-processor, that are further described below. These softwares were chosen based on recommendations from, and availability at Alten.

2.5.1 Pre-processing

The software used for pre-processing in this thesis was ANSA Pre-processor. ANSA [28] is a Computer Aided Engineering (CAE) pre-processing software, developed by BETA CAE Systems, used for build up of models. This software is widely used in automotive industry amongst others, and is suitable for both Computational Fluid Dynamics (CFD) and structural models. Modeling tasks such as geometry clean-up, FE-meshing, and boundary conditions can be done in ANSA. In this thesis all these modeling tasks were performed in ANSA.

2.5.2 FEA solver

The solver used in this thesis was Abaqus Unified FEA, since it handles complex materials, contacts, fracture and failure, which are key elements in the joint that was studied. Abaqus Unified FEA [29] is a CAE simulation software in the Dassault Systèmes Simulia platform. Abaqus Unified FEA has powerful and complete solutions for both routine and sophisticated engineering problems covering a vast spectrum of industrial applications [29]. Abaqus Unified FEA is popular in many disciplines due to the wide material modeling capability and the ability to customize the program[30]. In this thesis Abaqus Unified FEA was used only as a solver, i.e. no modeling tasks were performed using this software.

2.5.3 Post-processing

The software used for post-processing in this thesis was META Post-processor along with Mathworks Matlab R2018b. META is a multi-purpose post-processing software, developed by BETA CAE Systems, which can be used for even the most demanding post-processing requirements for structural and CFD analyses [31]. It supports many popular solvers used for structural and CFD analyses, such as Abaqus. META can be used for both 3D field post-processing as well as 2D plot post-processing, enabling everything from animations, plots and videos to reports and other objects [31]. META, along with Matlab were used to generate the 2D plots presented throughout the report.

2.6 Coordinate systems

The local coordinate system referred to in this report is a 3D Cartesian system with x, y, z or 1,2,3 as axes. The LVL is always placed with the main fibre direction, which is also the fibre direction of the face plies, in the x -, or 1-direction. y , 2 is transverse in plane and z , 3 is in the stacking direction. See Figure 2.8.

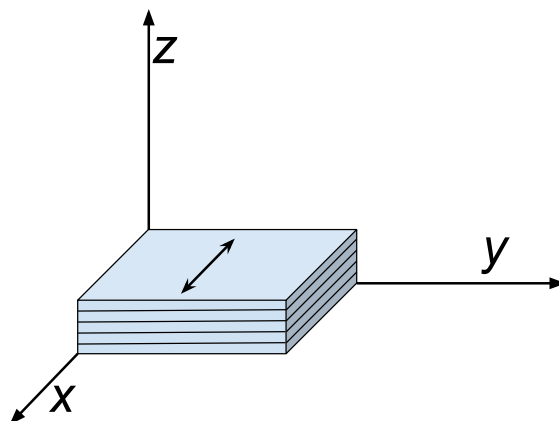


Figure 2.8: The coordinate system in relation to the fibre orientation of the face ply.

2.7 Constitutive modeling of the materials

When performing mechanical analyses of engineering materials and their structural components, it is important to be able to understand and describe the physical characteristics properly. In order to do so constitutive models are used, which link the states of stress and strain that occur during loading. Since the joint that was analyzed in this thesis consisted of three different materials with different properties this was extra important in order to correctly model the materials.

The wood is, as mentioned, an orthotropic material which is a subset of anisotropic materials, unlike the steel and the glue which are isotropic materials. The material properties in anisotropic materials depend on the direction in which they are measured and they also have three symmetry planes. Isotropic materials, on the other hand have the same properties in every direction.

2.7.1 Elasticity for orthotropic and isotropic materials

In the elastic region of the stress-strain behaviour for different materials, a material that have been subjected to external forces has the ability to return to its original shape and size when the forces have been removed. In linear elasticity the relation between the stress tensor, $\boldsymbol{\sigma}$, and the strain tensor, $\boldsymbol{\varepsilon}$, for a material subjected to uniaxial tension can be expressed using Hooke's law as,

$$\boldsymbol{\sigma} = \mathbf{C} \cdot \boldsymbol{\varepsilon} \quad (2.1)$$

where \mathbf{C} is the elastic stiffness tensor. Depending on the mechanical properties of the studied material these tensors differ. For the wood, Equation 2.1 can further be expressed in terms of components with respect to the orthonormal coordinate system according to,

$$\sigma_{ij} = C_{ijkl} \varepsilon_{kl} \quad (2.2)$$

where i, j, k and l denote three mutually orthogonal material directions ($i, j, k, l = [1,6]$). Due to symmetry of the stress and strain tensor, the following symmetries occur for linear elastic materials,

$$C_{ijkl} = C_{jikl}, \quad C_{ijkl} = C_{ijlk}, \quad C_{ijkl} = C_{klij} \quad (2.3)$$

Using these symmetries Equation 2.1 can be rewritten in matrix form as,

$$\begin{bmatrix} \sigma_{11} \\ \sigma_{22} \\ \sigma_{33} \\ \sigma_{23} \\ \sigma_{31} \\ \sigma_{12} \end{bmatrix} = \begin{bmatrix} C_{1111} & C_{1122} & C_{1133} & C_{1123} & C_{1131} & C_{1112} \\ C_{2211} & C_{2222} & C_{2233} & C_{2223} & C_{2231} & C_{2212} \\ C_{3311} & C_{3322} & C_{3333} & C_{3323} & C_{3331} & C_{3312} \\ C_{2311} & C_{2322} & C_{2333} & C_{2323} & C_{2331} & C_{2312} \\ C_{3111} & C_{3122} & C_{3133} & C_{3123} & C_{3131} & C_{3112} \\ C_{1211} & C_{1222} & C_{1233} & C_{1223} & C_{1231} & C_{1212} \end{bmatrix} \begin{bmatrix} \varepsilon_{11} \\ \varepsilon_{22} \\ \varepsilon_{33} \\ 2\varepsilon_{23} = \gamma_{23} \\ 2\varepsilon_{31} = \gamma_{31} \\ 2\varepsilon_{12} = \gamma_{12} \end{bmatrix} \quad (2.4)$$

Since an elastic orthotropic material has three orthogonal symmetry planes, the stiffness matrix in Voigt notation can be written as,

$$\underline{\underline{\mathbf{C}}} = \begin{bmatrix} C_{11} & C_{12} & C_{13} & 0 & 0 & 0 \\ C_{12} & C_{22} & C_{23} & 0 & 0 & 0 \\ C_{13} & C_{23} & C_{33} & 0 & 0 & 0 \\ 0 & 0 & 0 & C_{44} & 0 & 0 \\ 0 & 0 & 0 & 0 & C_{55} & 0 \\ 0 & 0 & 0 & 0 & 0 & C_{66} \end{bmatrix} \quad (2.5)$$

By taking the inverse of the elastic stiffness matrix, the compliance matrix, $\underline{\underline{\mathbf{S}}}$, is obtained which can be used in order to describe the strain-stress relation for orthotropic linear elastic materials in Voigt notation as,

$$\underline{\underline{\boldsymbol{\varepsilon}}} = \underline{\underline{\mathbf{S}}} \underline{\underline{\boldsymbol{\sigma}}} \quad (2.6)$$

with

$$\underline{\underline{\mathbf{S}}} = \begin{bmatrix} \frac{1}{E_1} & -\frac{\nu_{21}}{E_2} & -\frac{\nu_{31}}{E_3} & 0 & 0 & 0 \\ -\frac{\nu_{12}}{E_1} & \frac{1}{E_2} & -\frac{\nu_{32}}{E_3} & 0 & 0 & 0 \\ -\frac{\nu_{13}}{E_1} & -\frac{\nu_{23}}{E_2} & \frac{1}{E_3} & 0 & 0 & 0 \\ 0 & 0 & 0 & \frac{1}{G_{23}} & 0 & 0 \\ 0 & 0 & 0 & 0 & \frac{1}{G_{31}} & 0 \\ 0 & 0 & 0 & 0 & 0 & \frac{1}{G_{12}} \end{bmatrix} \quad (2.7)$$

Hence, the material parameters needed in order to describe the elastic relation between the stress and the strain for the wood are the parameters included in the compliance matrix presented in Equation 2.7 [32]. These parameters were used as input in ANSA when modeling the wooden material.

Furthermore, for the steel and the glue which are isotropic materials, the strain-stress relationship is given by,

$$\begin{bmatrix} \varepsilon_{11} \\ \varepsilon_{22} \\ \varepsilon_{33} \\ \gamma_{23} \\ \gamma_{31} \\ \gamma_{12} \end{bmatrix} = \begin{bmatrix} \frac{1}{E} & -\frac{\nu}{E} & -\frac{\nu}{E} & 0 & 0 & 0 \\ -\frac{\nu}{E} & \frac{1}{E} & -\frac{\nu}{E} & 0 & 0 & 0 \\ -\frac{\nu}{E} & -\frac{\nu}{E} & \frac{1}{E} & 0 & 0 & 0 \\ 0 & 0 & 0 & \frac{1}{G} & 0 & 0 \\ 0 & 0 & 0 & 0 & \frac{1}{G} & 0 \\ 0 & 0 & 0 & 0 & 0 & \frac{1}{G} \end{bmatrix} \begin{bmatrix} \sigma_{11} \\ \sigma_{22} \\ \sigma_{33} \\ \sigma_{23} \\ \sigma_{31} \\ \sigma_{12} \end{bmatrix} \quad (2.8)$$

Hence, only three parameters needed to be defined in order to describe the elastic strain-stress behaviour of the steel and the glue, the Young's modulus, E , the Poisson's ratio, ν , and the shear modulus, G [32]. Once again, these parameters were used as input in ANSA when modeling the material models for the steel and the glue.

2.7.2 Elasto-plasticity for the glue and the steel

The relations presented in Equation 2.6-2.8, are only valid for describing the elastic material behaviour, more specifically when the stress, σ , is smaller than the current yield stress, σ_y . For stresses larger than the yield stress, i.e. $\sigma > \sigma_y$, the material will be subjected to plastic strains, which means that the material undergoes non-reversible changes of shape as a result of the applied forces. When the plastic domain has been reached Hooke's law is no longer valid to describe the relation between the stress and the strain, since it no longer varies linearly. In order to reduce the complexity of analyzing inelastic materials, the elastic and plastic behaviours are studied separately. By assuming small deformations, the strain tensor can be expressed as [33],

$$\varepsilon = \varepsilon^e + \varepsilon^p \quad (2.9)$$

where ε^e and ε^p denotes the elastic and plastic strains, respectively. Even though the stresses no longer varies linearly during loading, the unloading is still linear [33]. When unloading to $\sigma = 0$, there will be strain remaining in the material, which is called the plastic strain. The stress-strain curve for a inelastic material can be seen in Figure 2.9.

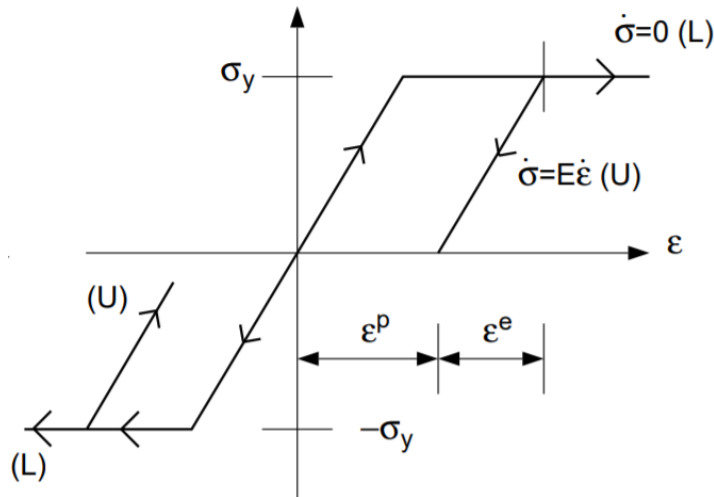


Figure 2.9: Illustration of the elastic and plastic strain in a stress-strain curve for a inelastic perfectly plastic material [4]. (L) stands for plastic loading and (U) stands for elastic unloading.

2.7.2.1 Isotropic hardening plastic behaviour

For steel subjected to pure tension, the typical stress-strain behavior can be described using the yield stress, plastic hardening and ductile fracture [4]. Hardening can be described as the further increase of stress beyond the yielding. Since the joint studied in this thesis is subjected to a monotonic load, isotropic hardening was used. When modelling metallic materials the plastic deformation is assumed to be volume preserving, which means that the plastic strain is deviatoric. The free energy is then consisting of two different contributions; one completely reversible (elastic) portion due to volume change, ψ_v , and one volume preserving inelastic contribution, ψ_{dev} [4]. The free energy can then be expressed as,

$$\psi = \psi_{\text{dev}}[i_{\text{dev}}^e] + \psi_{\text{v}}[\varepsilon_{\text{v}}] + \psi_{\text{mic}}[k] \quad (2.10)$$

with

$$\psi_{\text{dev}} = \frac{1}{2}2G(i_{\text{dev}}^e), \quad \psi_{\text{v}} = \frac{1}{2}K\varepsilon_{\text{v}}^2, \quad \frac{1}{2}Hk^2 \quad (2.11)$$

where G is the elastic shear modulus, K is the bulk modulus, H is the hardening modulus representing linear hardening, i_{dev}^e is the elastic deviatoric strain invariant, k is an isotropic hardening variable and ε_{v} is the volumetric strain. The volumetric strain and the elastic deviatoric strain invariant are further defined as

$$i_{\text{dev}}^e = \boldsymbol{\varepsilon}_{\text{dev}}^e : \boldsymbol{\varepsilon}_{\text{dev}}^e \quad \text{with} \quad \boldsymbol{\varepsilon}_{\text{dev}}^e = \boldsymbol{\varepsilon}_{\text{dev}} - \boldsymbol{\varepsilon}_{\text{dev}}^p \quad \text{and} \quad \varepsilon_{\text{v}} = \mathbf{1} : \boldsymbol{\varepsilon} \quad (2.12)$$

From Equation 2.11 and 2.12 the state equations can be derived as

$$\boldsymbol{\sigma}_{\text{dev}} = \frac{\partial \psi_{\text{dev}}}{\partial \boldsymbol{\varepsilon}_{\text{dev}}^e} = 2G\boldsymbol{\varepsilon}_{\text{dev}}^e \quad (2.13)$$

$$\sigma_{\text{m}} = \frac{\partial \psi_{\text{v}}}{\partial \varepsilon_{\text{v}}} = K\varepsilon_{\text{v}} \quad (2.14)$$

$$\kappa = -\frac{\partial \psi_{\text{mic}}}{\partial k} = -Hk \quad (2.15)$$

where κ is the micro hardening stress representing the hardening state of the microstructure of the material and the continuum stress is given by $\boldsymbol{\sigma} = \boldsymbol{\sigma}_{\text{dev}} + \sigma_{\text{m}}\mathbf{1}$.

When defining the plasticity in ANSA in this thesis, the von Mises yield criterion were used. The yield function pertinent to the von Mises yield function with isotropic hardening can be written as

$$\phi = \sigma_{\text{e}} - (\sigma_{\text{y}} + \kappa) \quad \text{with} \quad \sigma_{\text{e}} = \sqrt{\frac{3}{2}}\boldsymbol{\sigma}_{\text{dev}} \quad (2.16)$$

where σ_{e} is the effective von Mises stress. From this, the evolution of the internal variables $\{\dot{\boldsymbol{\varepsilon}}^p, \dot{k}\}$ can be expressed as the flow rule as

$$\dot{\boldsymbol{\varepsilon}}^p = \lambda \frac{\partial \phi}{\partial \boldsymbol{\sigma}_{\text{dev}}} = \lambda \mathbf{f} \quad (2.17)$$

$$\dot{k} = \lambda \frac{\partial \phi}{\partial \kappa} = -\lambda \quad (2.18)$$

where λ is a plastic multiplier defined by the loading conditions; $\phi \leq 0, \lambda \geq 0, \lambda\phi = 0$, and \mathbf{f} is the gradient of the yield surface defined as

$$\mathbf{f} = \frac{\partial \phi}{\partial \boldsymbol{\sigma}_{\text{dev}}} = \frac{\partial \sigma_{\text{e}}}{\partial \boldsymbol{\sigma}_{\text{dev}}} = \frac{3}{2} \frac{\boldsymbol{\sigma}_{\text{dev}}}{\sigma_{\text{e}}} \quad (2.19)$$

By combining the rate formulated state equations in Equations 2.13-2.15, with the flow rules in Equations 2.17 and 2.18, a generic format for the present case of isotropic linear hardening plasticity can be written as

$$\dot{\boldsymbol{\sigma}} = \mathbf{E} : \dot{\boldsymbol{\epsilon}} - \lambda \mathbf{E} : \mathbf{f} \quad (2.20)$$

$$\dot{\kappa} = H\lambda \quad (2.21)$$

where $\mathbf{E} = 2G\mathbf{I} + K\mathbf{1} \otimes \mathbf{1}$ is the elastic stiffness modulus tensor and \mathbf{f} is the gradient of the yield surface. For a more detailed description of the solution process used in Abaqus Unified FEA, see the Abaqus Users's Manual [34].

In Abaqus Unified FEA the final solution is obtained using the Newton's method [35]. The hardening parameters needed in order to obtain the solution are calculated in Abaqus Unified FEA based on the plastic stress-strain curved defined by the user.

2.8 Fracture modeling of the glue and the steel

During the tensile tests of the joint performed by Modvion, fracture occurred in the glue and the steel after being subjected to a large enough force. Fracture in a component means that cracking exists to the extent that the component is separated into two or more pieces. In order to avoid structural failure in a component, the stress must not exceed the strength of the material, which is the stress that causes a deformation or fracture failure when exceeded.

There are many variables that has to be taken into account when studying the fracture mechanics of a component. For example, stresses often act in more than one direction that can trigger the crack propagation leading to failure. Also, the real components may already contain flaws or cracks prior to loading, which need to be specifically considered. This could be the case for the joint studied in this thesis if the glue does not fill the entire cavity between the steel and the wood. Therefore, it is required to further analyse the assembled joint with respect to already existing flaws that may affect the fracture mechanics in the reality so this can be accounted for in the creation of the FE-model.

The different ways of applying a force or a displacement to a component in order to enable crack propagation are often divided into three fracture modes: Mode I, Mode II and Mode III, see Figure 2.10.

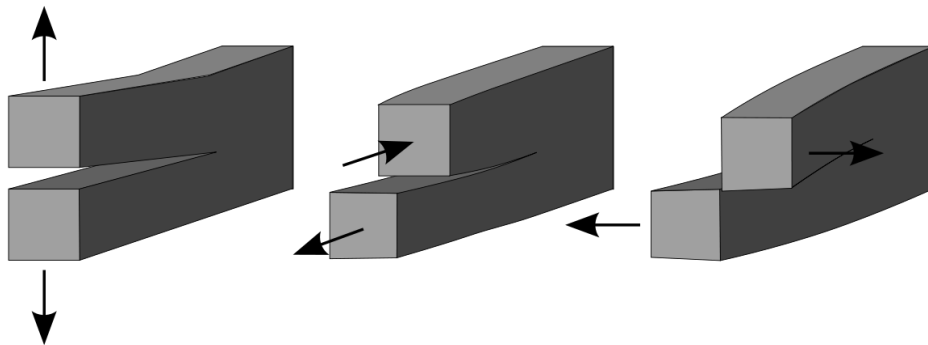


Figure 2.10: The three different fracture modes from left to right: Mode I Opening, Mode II sliding, Mode III tearing.

Mode I, also called the opening mode, corresponds to when a tensile stress is applied normal to the plane of the crack. This is the fracture mode that occurs in the steel plate in the joint during the tensile tests that are studied in this thesis. Mode II, the sliding mode, corresponds to when a shear stress is acting parallel to the crack, so called in-plane shearing. Finally, Mode III, the tearing mode, corresponds to when a shear stress is acting perpendicular to the crack, so called out-of-plane shearing. The shearing modes may both occur in the glue when the joint is subjected to pure tension.

There are different types of material failures depending on if the deformation of the studied component is time dependent or time independent, and if the component is subjected to either static loading or cyclic loading. Since there are various types of deformation and fracture, it is important to correctly identify which behaviour that apply to the component that are studied in order to choose the suitable analysis method to predict the behaviour. The joint that is studied in this thesis is determined to have time independent deformation and is subjected to static loading, since the applied force changes slowly [36]. For static loading, the fracture can have either brittle or ductile behaviour. The stress-strain behaviour for both these cases can be seen in Figure 2.11.

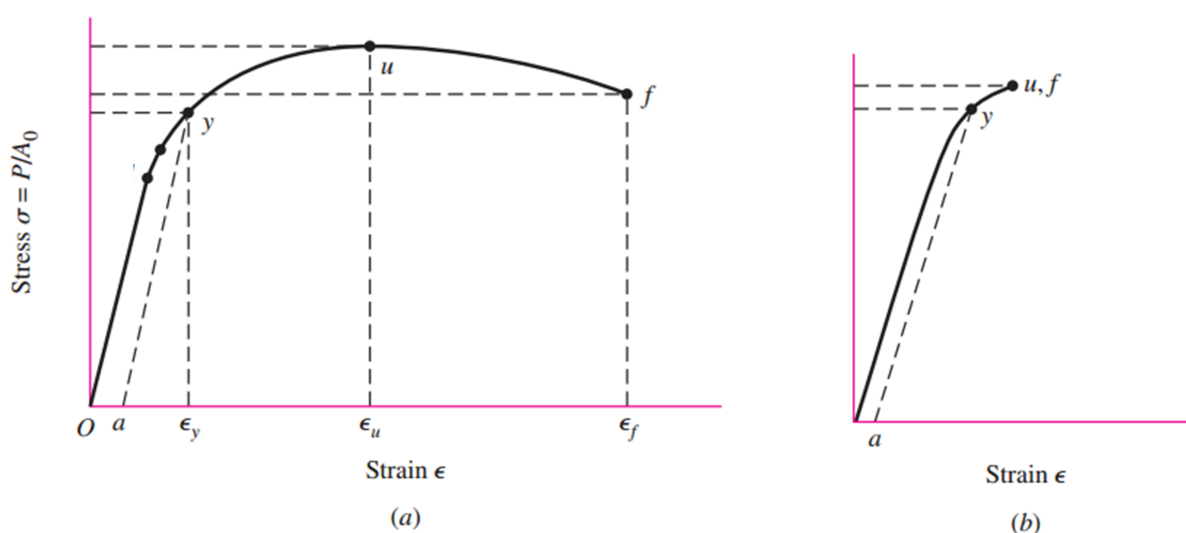


Figure 2.11: Tension test showing brittle (a), and ductile (b) behavior [5]. The y is the yield stress, u is ultimate strength and f stands for fracture.

As can be seen in the figure presented above, both a ductile and brittle material have plastic deformation, but the amount is considerably larger for the ductile behaviour. For brittle materials, fracture occurs directly when the ultimate strength has been reached, which is the case for the glue, but for ductile materials, i.e. the steel, there exists a damage zone ($\epsilon_u \rightarrow \epsilon_f$) before fracture occurs. In the damage zone for ductile materials, necking is present and the decrease in force beyond the ultimate strength is due to the rapid decrease in the cross-sectional area [36]. This was taken into consideration when defining the material model for the glue and the steel.

When defining the fracture behaviour of the materials, the variables needed were the plastic strain at damage initiation and the damage evolution expressed as the effective total displacement to failure, measured from the time of damage initiation, i.e. ϵ_u . The

displacement at failure is dependent of the failure strain, ε_f , and the characteristic element length of the model. More information about the specific input values used for simulating the fracture for the different materials are presented in Chapter 3.

2.8.1 Element deletion

In order to simulate the fracture behaviour of the glue and the steel in Abaqus Unified FEA, damage initiation and damage evolution were used together with element deletion. Element deletion refers to when actual elements are deleted from the model upon reaching maximum degradation, D_{\max} , at all of the section points at any integration locations, i.e. Gauss points, of an element [6].

By applying this method to simulate the fracture, it is important to pay attention to how this is implemented. Since the method is based on removing elements, it also means that actual mass is removed from the model. This may cause equilibrium issues leading to inaccurate result, and if used with an implicit solver it can also cause convergence problems. This risk of equilibrium issues can be reduced by using a sufficiently fine mesh in the regions that may be exposed to failure. In order to avoid convergence problems, an explicit solver should rather be used with this approach. When using an explicit solver, it is important to use sufficiently small time increments in order to make the solver stable, close to equilibrium [37]. If the time increment is too large, it will result in a unstable solution, which often makes solution variables such as displacement oscillate with increasing amplitudes. Also the total energy balance will change significantly.

Since the joint studied in this thesis consists of multiple materials, the initial time increment will be determined by the element with the highest wave speed [37]. An approximation of the stability limit can be written as

$$\Delta t \approx \frac{L_{\min}}{c_d} \quad (2.22)$$

where L_{\min} is the smallest element dimension in the mesh and c_d is the dilatational wave speed [37]. Since a fine mesh combined with small time increments are necessary, the simulations take long time to run. There are different ways to reduce the computational cost when running dynamic explicit analysis. Two approaches were used in this thesis:

- Reducing the computational cost by speeding up the simulation. Increasing the velocity and decreasing the time period.
- Reducing the computational cost by using mass scaling.

The first approach is based on reducing the number of increments, n , required by speeding up the simulation in comparison to the time of the actual process. This is done by reducing the time period of the event, T . However, if the speed-up is too large it may cause errors due to increased inertia forces, which will change the predicted response. The other approach is based on artificially increasing the material density by a factor f^2 which will reduce the number of required time increments to n/f , which is the same as decreasing the time period to T/f [37]. This approach has the same effect on the inertia forces as when reducing the time period.

There are two different types of mass scaling available in Abaqus Unified FEA, fixed and variable [38]. With fixed mass scaling, the scaling is performed once at the beginning of the step for which is specified, and for variable mass scaling, the mass is scaled at the beginning of a step and then periodically throughout that step. In the analyses in this project, fixed mass scaling was used.

With both approaches used for reducing the computational cost, it is important to ensure that the inertia forces do not dominate and change the solution. This can be done by monitoring the kinetic energy such that the ratio of kinetic energy to internal energy is not too large, preferably less than 10% [37] in order to retain accuracy of the solution.

For both the steel and the glue, the ductile damage initiation criterion was used, which is a phenomenological model used for predicting damage caused by nucleation, growth and coalescence of voids [39]. The model assumes that the plastic strain at damage, ε_D^p , is a function of the stress triaxiality, η , and the equivalent plastic strain rate, $\dot{\varepsilon}^p$, as

$$\varepsilon_D^p(\eta, \dot{\varepsilon}^p) \quad (2.23)$$

The stress triaxiality is defined as $\eta = -p/q$, where p is the pressure stress and q is the Mises equivalent stress. The damage criterion is then reached when the following condition is satisfied

$$\omega_D = \int \frac{d\varepsilon^p}{\varepsilon_D^p(\eta, \dot{\varepsilon}^p)} = 1 \quad (2.24)$$

where ω_D is a state variable, which increases with the plastic deformation.

2.9 Simulation set-up

All models created in this thesis are meshed using C3D8R elements, which are hexahedral 3D elements with 8 nodes. The R stands for reduced integration which are used since it usually provides more accurate results and significantly reduces the computational time, especially in three dimensions.

The boundary conditions used in the simulations were that one end of the test specimen was fixed in all directions and in the other end, either a displacement or a velocity was applied in one direction. For the static implicit analyses a displacement was applied and for the dynamic explicit analyses a constant velocity was applied.

3

Analysis and validation of material data

In order to get a deeper understanding of the starting position of the project the given data, both from physical tests and data sheets, needed to be analyzed, interpreted and validated.

3.1 Physical tensile test data for the joint

The physical test data that was given was data obtained from three pure tensile tests performed by Modvion. These tests were performed at RISE in Borås. Two identical extensometers were used, one on each side of the gap, attached 45 mm from the edges of the split line. In Figure 3.2 the full test set-up can be seen. All of the three tensile tests resulted in the fracture occurring at the same place, which was the horizontal row of holes closest to the split line, see Figure 3.1.



Figure 3.1: The fracture in the first row of holes.

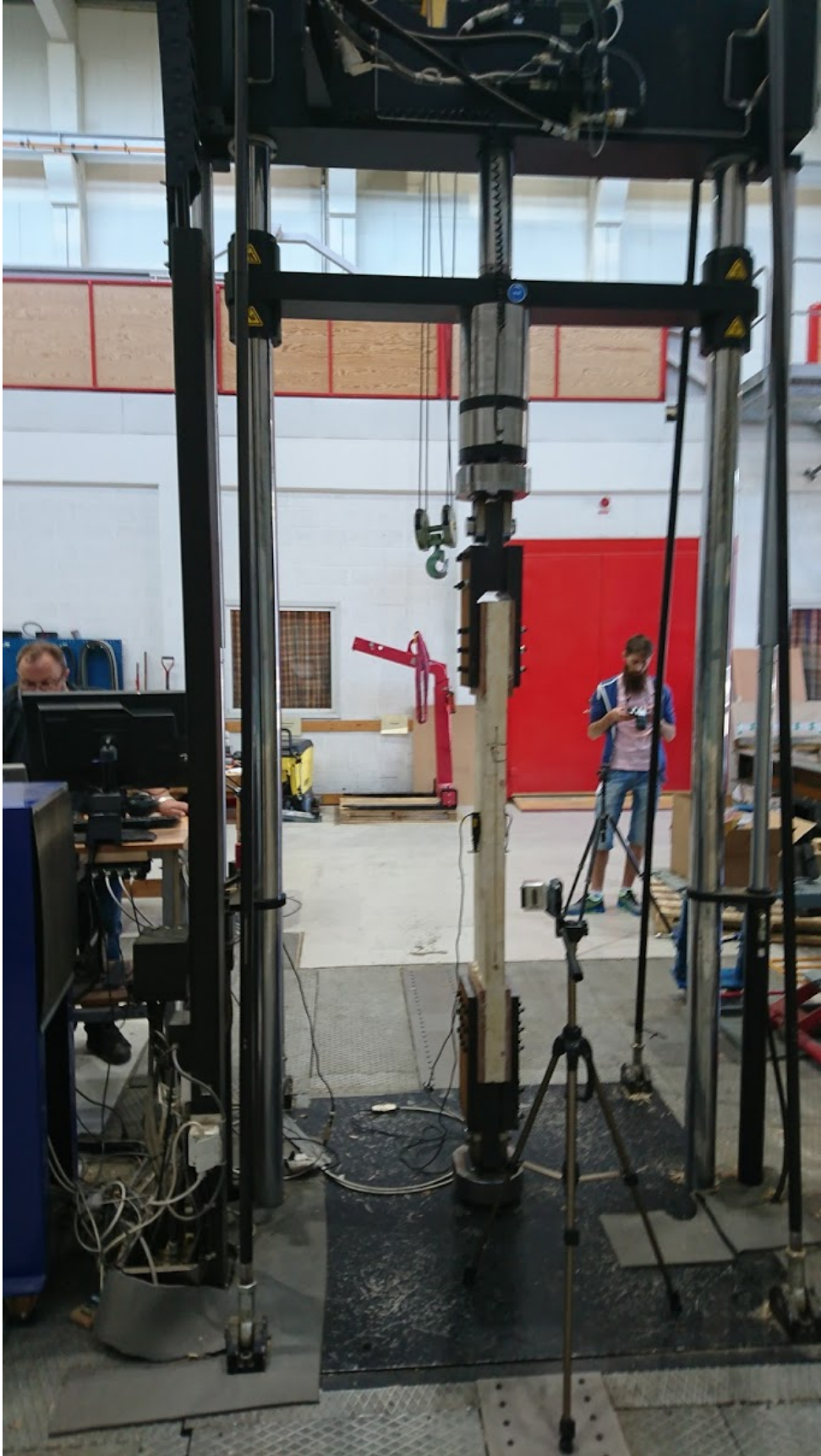


Figure 3.2: The tensile test set-up at RISE.

Along with the local displacement over the split line measured by the extensometers, time, load and global machine displacement were measured as well. The given data are plotted in Figure 3.3 below. The tests were force-controlled with a special cycle shown in the first sub figure. The relaxation in the force gives the ambiguity in the other plots.

The force vs. local displacement curves in the lower figures is what was desired to be replicated in the simulations of the full-scale model of the joint. The reason for not converting this data to a stress-strain curve is because the joint consists of three different materials, all with different material properties and cross-sectional areas, making the conversion from force-displacement data to stress-strain data difficult.

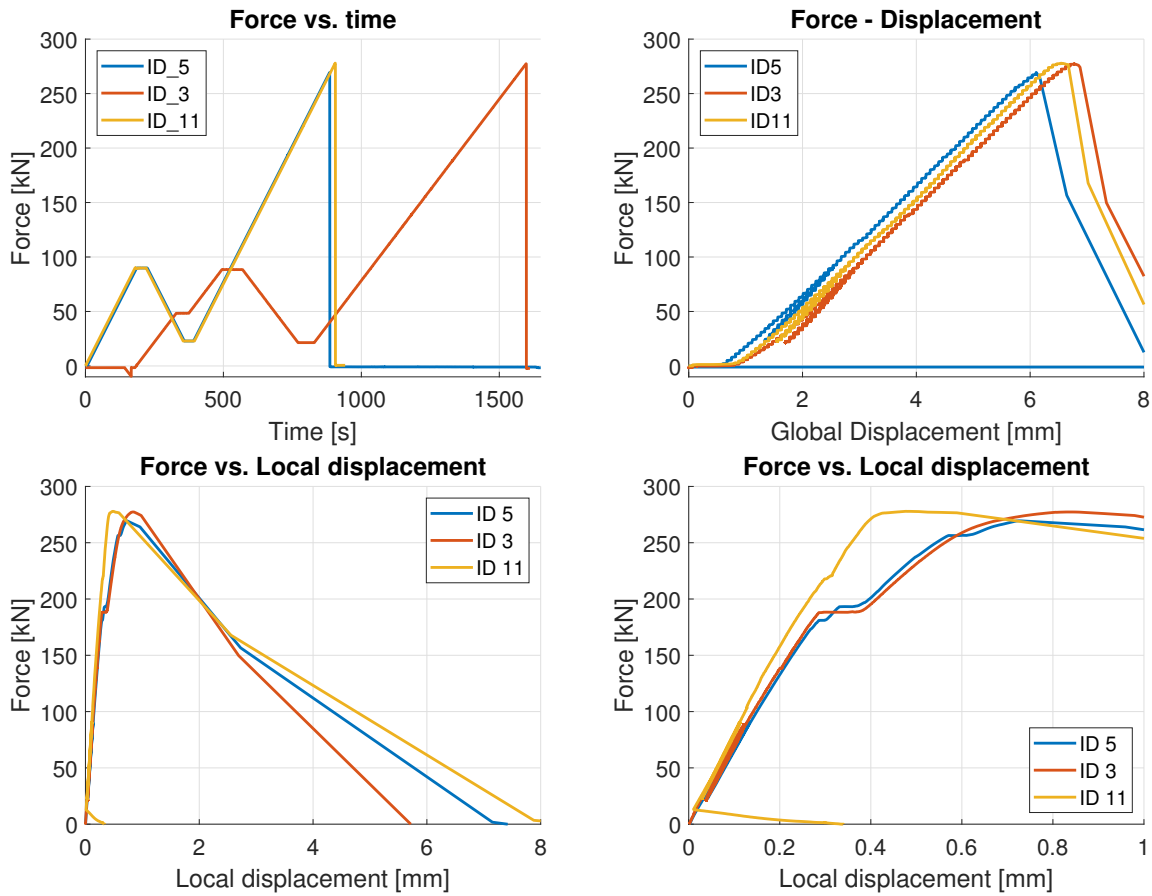


Figure 3.3: Test data from full joint tests performed at RISE. The two lower subfigures are the same data with different scopes on the x-axis.

3.2 Data obtained from research and tests

In order to create a correct model of the joint, material properties of the individual parts of the joint had to be obtained. Data sheets for the LVL panels [22], the glue [26] and the steel [40] were available on the internet. The data sheets only provided basic values such as Young's modulus, Yield strength and Tensile strength. The material parameters, for the different materials, obtained from the data sheets can be seen in Table 3.1.

Table 3.1: Mechanical properties from data sheets of the materials considered.

Parameter	Unit	Loctite CR 421	Kerto-Q 21–24 mm	STRENX 700 MC E
E_1	MPa	1560	10 000	205 000
E_2	MPa		1200	
E_3	MPa		130	
G_{12}	MPa	1310	600	
G_{13}	MPa		60	
G_{23}	MPa		22	
ν_{12}	MPa	0,3	0,2	0,3
ν_{13}	MPa		0,45	
ν_{23}	MPa		0,35	
ρ	kg/m ³	1350	510	7900
$f_{t,0}$	MPa	25–30	19	750–950

In addition to the material parameters presented above, it was desirable to get more information about the mechanical behaviour of the different materials, in order to get an accurate model of the entire joint. Therefore physical tests were performed on the wood and the glue, and additional data for the steel was provided from SSAB upon request. The stress-strain data given by SSAB is illustrated in Figure 3.4, and further description of the physical tests can be found in the following sections.

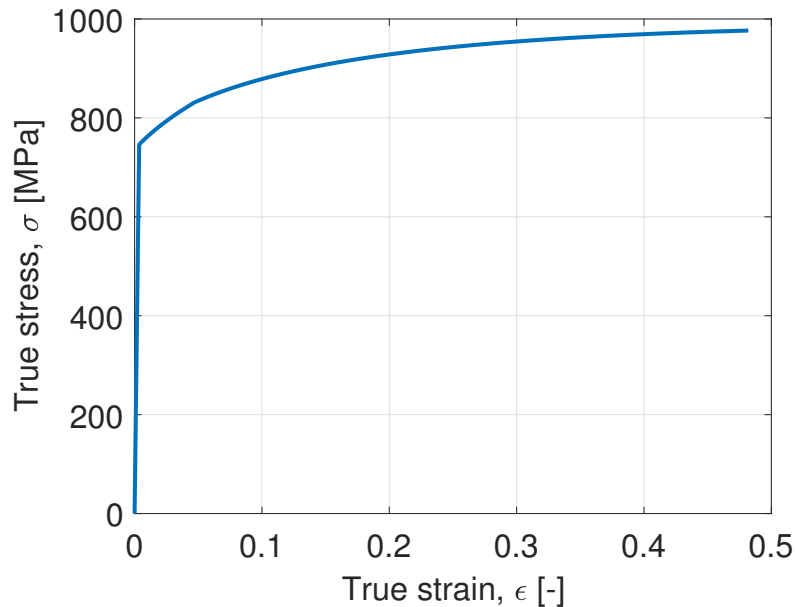


Figure 3.4: Stress-strain data for the steel, STRENX 700 MC E manufactured by SSAB.

From the additional data for the steel, the yield stress and the ultimate strength could be identified as 746 MPa and 976 MPa, respectively. These values were used when describing the plastic behaviour of the steel when validating the material model in ANSA and Abaqus Unified FEA.

3.2.1 Wood tensile tests of single veneers

The material parameters of the wood provided by the data sheet were given for an entire LVL panel, where it was considered as a homogeneous and orthotropic material. In order to validate the homogeneous and orthotropic material model for the wood, the material parameters of the wood on ply level needed to be defined. This was done by performing tensile tests on single veneers in the LVL panel, both parallel and perpendicular to the fibre direction. The geometries of the test specimens used for the tensile tests can be seen in Figures 3.6 and 3.7. Two different geometries were used to detect any geometry dependency. The tests were performed on a TRAM UTC 50 kN testing machine at Chalmers, which can be seen in Figure 3.5. Most of the tests were performed at a strain rate of 10 mm/min, which was picked after consultation with the examiner. The first batch was performed without an extensometer due to uncertainty regarding the use of it. After learning from previous test series, the second and last batch was performed with a 100 mm extensometer of model 3542-100M-005-ST made by Epsilon Technology Corp. An overview of the tests as well as the results can be found later in this section.



Figure 3.5: The test set up with a wide specimen in the TRAM UTC 50kN.

The available stock material for the tensile tests was an unfinished test joint, without the slots sawed, and with some incorrect fibre orientations. Due to the incorrect fibre orientations, it was possible to extract test specimens with the same fibre orientation consisting of more than one layer, which facilitated when testing the strength perpendicular to the fibres.

3. Analysis and validation of material data

From the two blocks, single and multiple plies could be extracted by using a band saw, a jointer, a planer, and finally a belt sander to remove residues from neighbouring plies and glue. On the first batch the dog-bone geometry was shaped out with a band saw and a belt sander, and on the second batch a CO₂ laser cutter was used. It was not possible to observe any significant difference in the results between the sanded and the laser cut samples, so in order to save time as well as get better accuracy and precision in the geometry, the laser cutter was continued to be used.

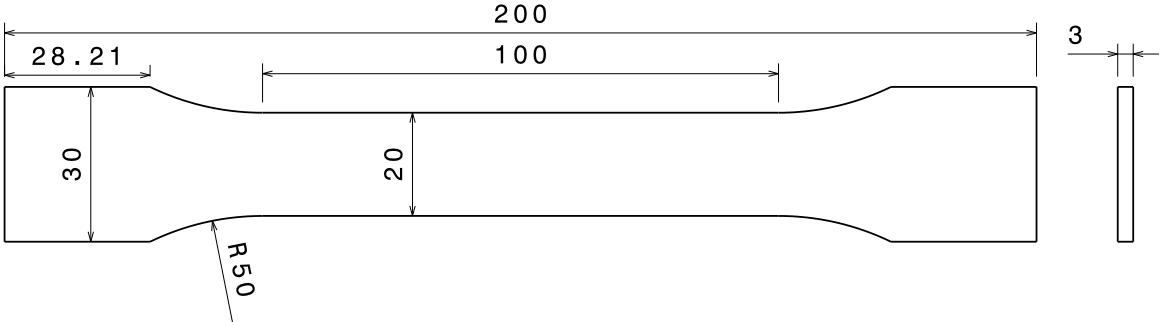


Figure 3.6: Drawing of the narrow tensile test specimen.

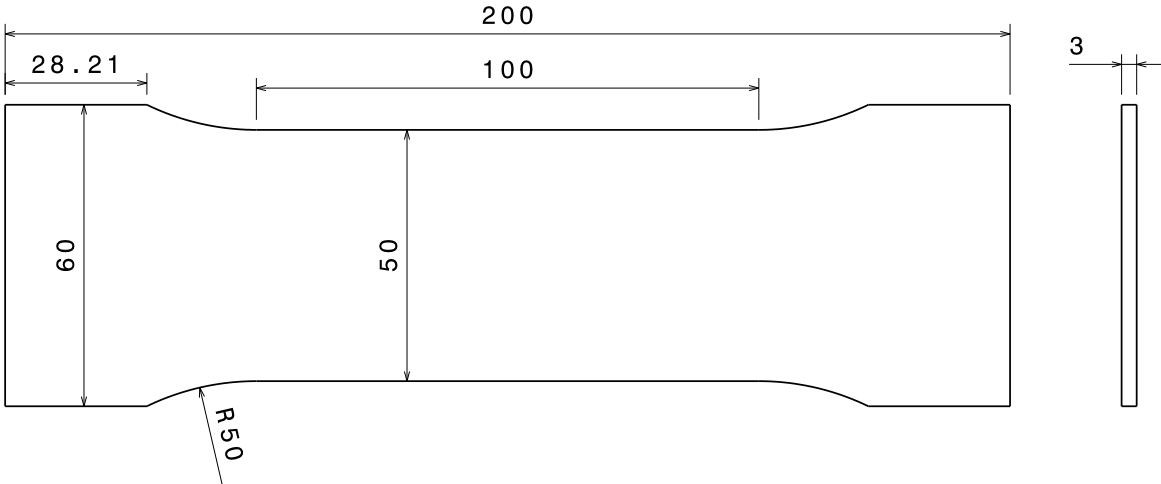


Figure 3.7: Drawing of the wide tensile test specimen.

The test data obtained from the tests consisted of the elapsed time, the machine displacement, extensometer data and the applied load. These data were then used in order to calculate the stress-strain behaviour of each specimen. The engineering stress, σ_e , and the engineering strain, ε_e , were computed accordingly,

$$\sigma_e = \frac{F}{A_0} \quad (3.1)$$

$$\varepsilon_e = \frac{\Delta L}{L_0} \quad (3.2)$$

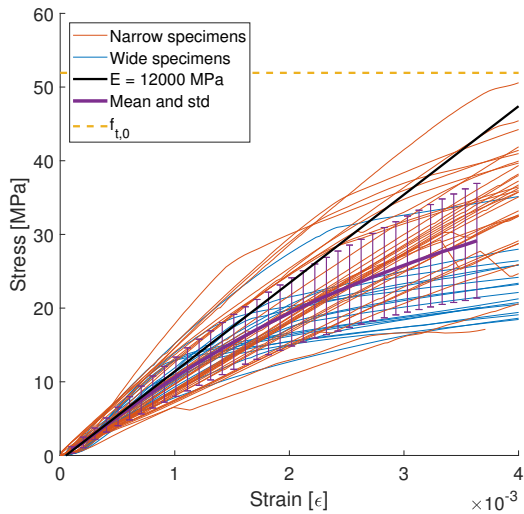
where F is the measured load as a result of the applied displacement, A_0 is the initial cross-sectional area of the specimen, ΔL is the displacement and L_0 is the initial length between the measurement points. The stress-strain data was then studied statistically resulting in a mean stress value and the standard deviation for each strain value. The mean, \bar{x} , and the standard deviation, s , was computed as,

$$\bar{x} = \frac{1}{N} \sum_{i=1}^N x_i \quad (3.3)$$

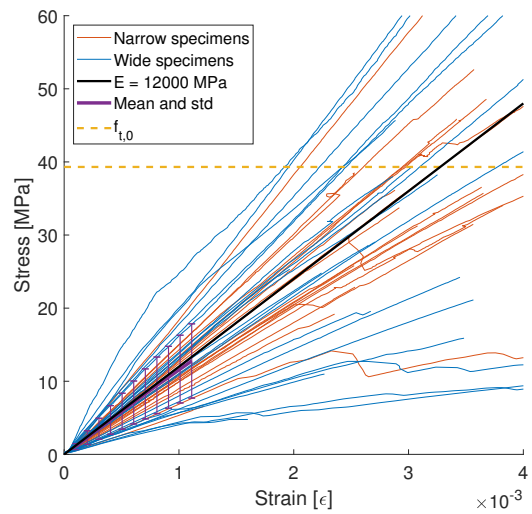
$$s = \sqrt{\frac{\sum_{i=1}^N (x_i - \bar{x})^2}{N - 1}} \quad (3.4)$$

where x_i is the different stress values and N is the number of values. This result was used when determining the Young's modulus in the 1- and 2- direction, which were later used to validate the homogeneous material using simulations.

Figures 3.8, 3.9 and 3.10 illustrates test data from the performed tests on single plies extracted from Kerto-Q 24 mm sheets, together with the mean and standard deviation for each case. Table 3.2 and Table 3.3 shows an overview of the tests where *dir1* and *dir2* refers to parallel and perpendicular fibre directions, respectively.

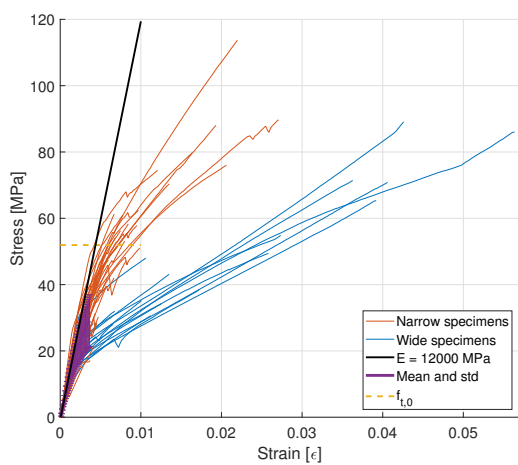


(a) Batch 1, along fibres.

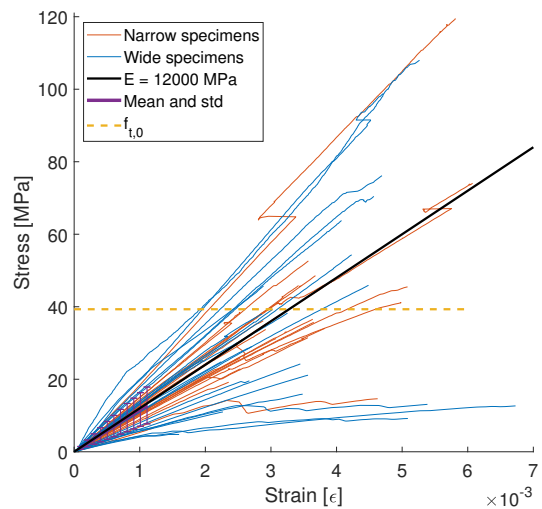


(b) Batch 2, along fibres.

Figure 3.8: The stress-strain behaviour obtained from the tests. Both subfigures has the same axes, however Batch 1 is measured without extensometer and batch 2 with.

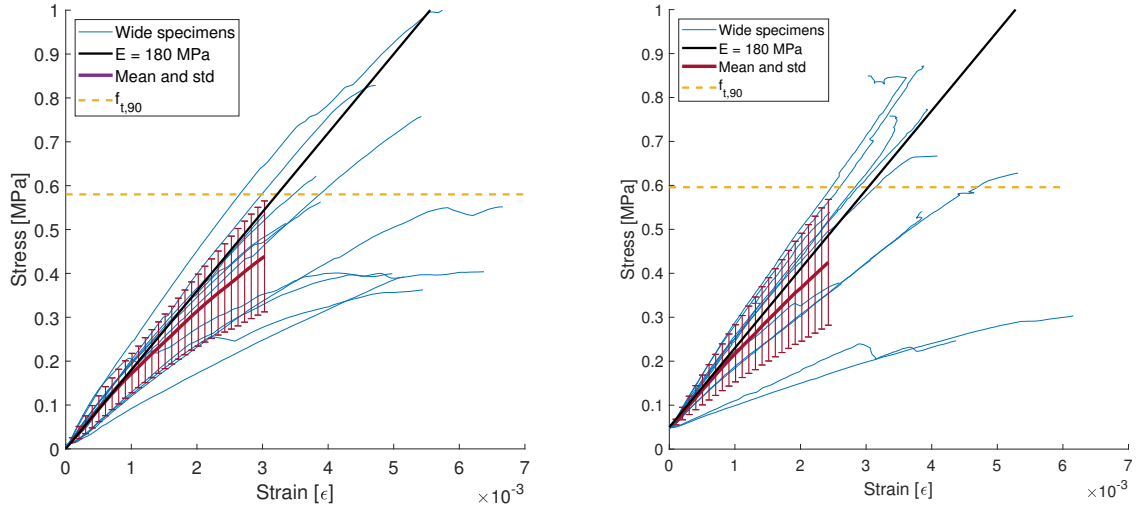


(a) Batch 1, along fibres.



(b) Batch 2, along fibres.

Figure 3.9: Same data as Figure 3.8 above, with all data visible. Curves are cut at the maximum stress values.



(a) Batch 1, across fibres, compensated global displacement data. (b) Batch 2, across fibres, extensometer data.

Figure 3.10: The stress-strain behaviour across fibre. Curves are cut at the maximum stress values.

Table 3.2: Overview of the tests on the Kerto-Q plies.

Date	Number and types of specimens	Batch
2019-02-26	7 wide dir1, 2 wide dir2, 8 narrow dir1	1
2019-02-27	12 wide dir1, 6 wide dir2 double	1
2019-03-02	18 wide dir1	1
2019-03-07	8 wide dir 1, 6 wide dir 2, 8 narrow dir1	1
2019-03-18	9 narrow dir1	2
2019-03-19	17 narrow dir1, 8 narrow odd, 30 wide dir 1, 12 wide dir2	2

Table 3.3: Summary of the tests.

Batch	1	2
Wide dir1	45	30
Narrow dir1	16	26
Wide dir2	14	12
Other	0	8

As can be seen when comparing Figures 3.8a and Figures 3.8b, there is a difference between them. This is due to how the strain is calculated. In batch 1 the machine displacement is used to calculate the strain in the sample, while in batch 2 the strain has been measured with an extensometer placed locally over the neck of the sample. Since the extensometer gives a more accurate value of the strain, the batch without the extensometer was disregarded when creating and validating the material model for the wooden plies. Furthermore, outliers and failed tests were removed before continuing with the development of the material model.

3.2.2 Glue tensile tests

During Modvion's manufacturing of the full joint test specimens there was some glue that leaked out on the floor when the joint was assembled. A block from this leak were made into two tensile tests. The block was cut into two dog-bone shape test samples with dimensions listed in Table 3.4. The geometry was very much limited by the available material. Tests were then performed in the same manner as for the wood but with the extensometer configured to 50 mm.

Table 3.4: Dimensions of the glue test specimens. All units are mm.

ID	Gripping distance	Width	Thickness	Neck length
1	100	28	14,5	55
2	98	26,8	14	55

Figure 3.11 shows the test results for the two test specimens described in Table 3.4. The data sheet for the glue specifies a Young's modulus of 1560 MPa, and a tensile strength of 25–30 MPa at a elongation of 2%. The test results deviate significantly from this, with a Young's modulus of about 5000 MPa and failure stress about 15 MPa. The large difference can hypothetically be explained by the curing conditions and the geometry of the glue.

It should be noted that both tests broke in the jaws, where the compressive pre-loading from the jaws affects the stress states significantly. Since only two tests were performed, which also were done under doubtful conditions, no conclusions could be drawn and the data provided in the data sheet was therefore used in the simulations.

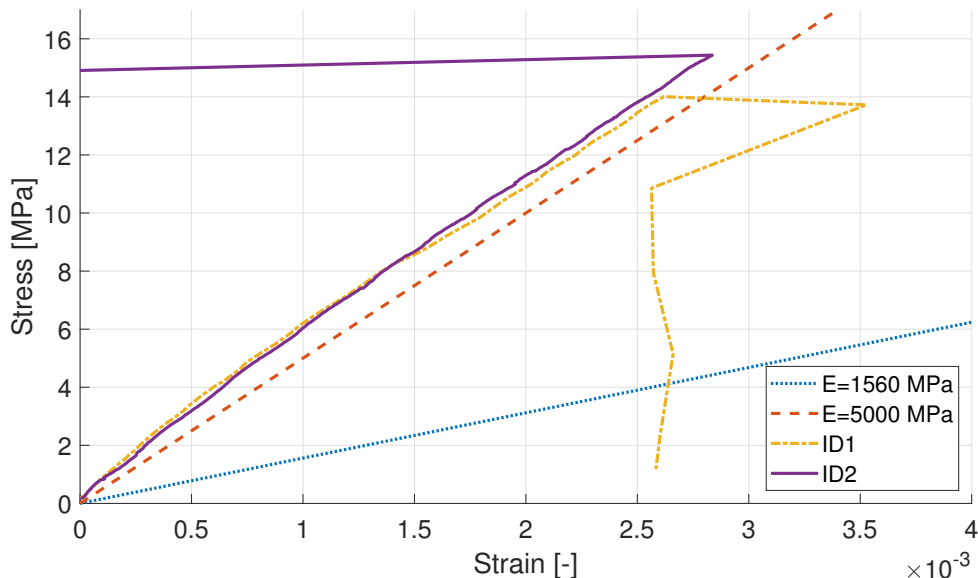


Figure 3.11: Stress-strain plot of the glue tests.

The significant variation of the tests, and the values from the data sheet may also be explained as that the data sheet might be extra conservative and/or that the glue properties can vary with environmental or other factors that are out of the scope for this thesis.

3.2.3 Cross section cuts of the test samples

To get an even deeper understanding of the mechanical behaviour inside the joint and what behaviour that is to be recreated using simulations, the inside of the full test joint was examined. This was done by sectioning the joint by physically cutting the samples into 30 mm thick pieces and scanning the cut surfaces. The scans of sample 4, 5, and 10 can be seen in Figures 3.13 and 3.14, 3.15 and 3.16, and 3.17 and 3.18, respectively. Sample 5 has been tested in pure tension and sample 4 and 10 has been tested for fatigue in tension/compression. Figure 3.12 explains how the slices are cut and labeled.

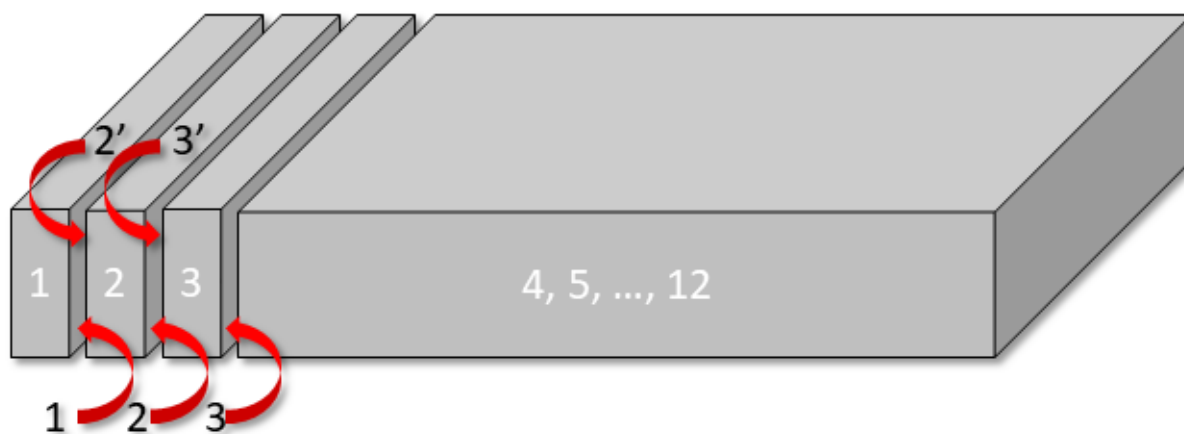


Figure 3.12: Cross-section sample cut overview.

From these cross-sections it can be observed that the static tension, i.e. sample 5, has more cracks in the glue, and the cracks also protrudes further into the sample. This indicates that the glue breaks in a brittle fracture at higher maximum loads and is probably not very sensitive to fatigue in this application. It can also be seen that the cracks occur almost exclusively in the interaction between the glue and the steel, and rarely in the interaction with the wood. This result was used when considering which type of contacts that should be used in the interaction between the three materials when creating the FE-model. Another very clear observation is the change in the width of the slot as well as the misalignment of the steel plate in the slot, which may also have an effect on the mechanical behaviour of the joint.



Figure 3.13: Sample 4, main side cut scans. Each cut is 30 mm apart. Sample 4 has been tested for fatigue at more than 30 000 cycles, where the load is unknown to us.



Figure 3.14: Sample 4, prim side cut scans.



Figure 3.15: Sample 5, main side cut scans. Each cut is 30 mm apart. Sample 5 has been tested in pure tension and broke at 269 kN.



Figure 3.16: Sample 5, prim side cut scans.

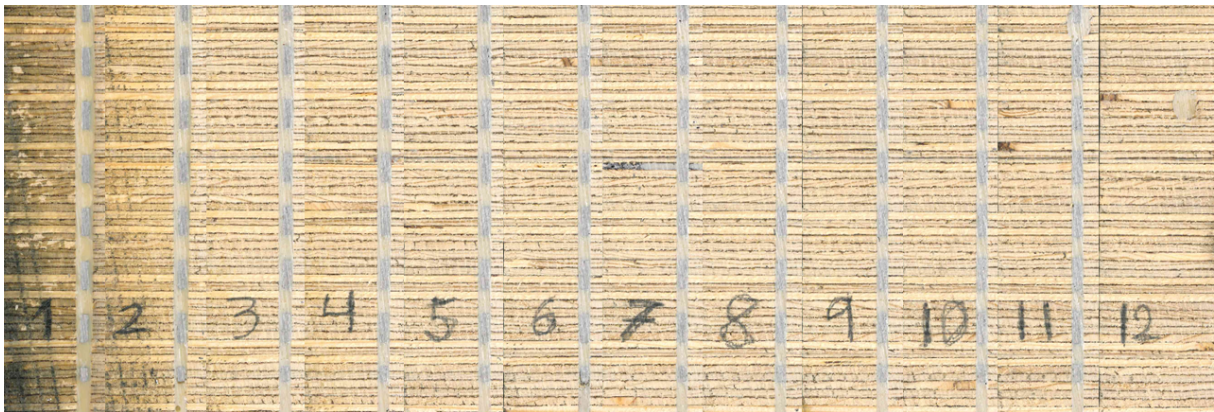


Figure 3.17: Sample 10, main side cut scans. Each cut is 30 mm apart. Sample 10 has been tested for fatigue in tension/compression at 165 kN and broke after 3250 cycles.



Figure 3.18: Sample 10, prim side cut scans.

3.3 Recreation of the material behaviours

Before developing the FE-model of the joint, the material models for the three materials that the joint consists of needed to be validated. This was done by using ANSA as pre-processor and Abaqus Unified FEA as solver, with the intention to obtain simulation results that correctly fit the material data from the physical tests and data sheets presented in the previous sections. By ensuring that the material models well represented the reality before continuing with the development of the entire model of the joint, the number of insecure parameters in the model could be reduced.

For the wood and the steel a sufficient amount of information was given in the data sheets in order to be able to validate these materials correctly. Therefore, precise parameters could be obtained for these materials in this step. For the glue, the provided information about its mechanical properties was quite scarce. Therefore the glue was treated as a variable all the way to the final simulations. However, a minor material validation was made for the glue, in order to have a base to work from when running simulations on the entire joint.

3.3.1 Material model for the wood

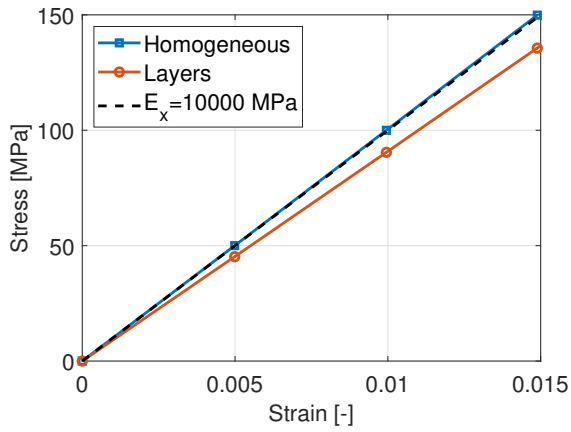
In order to investigate if the material parameters for the LVL provided by the manufacturer is representative, physical tensile tests were performed on the wood. The provided material properties in the data sheet were given for an entire LVL panel where it was considered as a homogeneous orthotropic material, instead of a laminate. To investigate if it is an adequate assumption to consider the LVL panel as homogeneous orthotropic instead of a laminate, the material properties for a single veneer were needed. When the material properties for a single veneer were known, it was possible to see if nine of these layers arranged in the correct way, would give orthotropic properties close to the values given in the data sheet.

The Young's modulus parallel and perpendicular to the fibre direction, i.e. E_1 and E_2 , were obtained from the physical tensile tests of the single veneers. The shear modulus and the Poisson's ratio in the different directions, and the elastic stiffness in the third direction were set equal to the values given in the data sheet for Kerto-S, which is an LVL panel consisting of veneers arranged with parallel fibre direction. The material parameters used in the simulation of the veneers along with the material properties given in the data sheets are presented in Table 3.5.

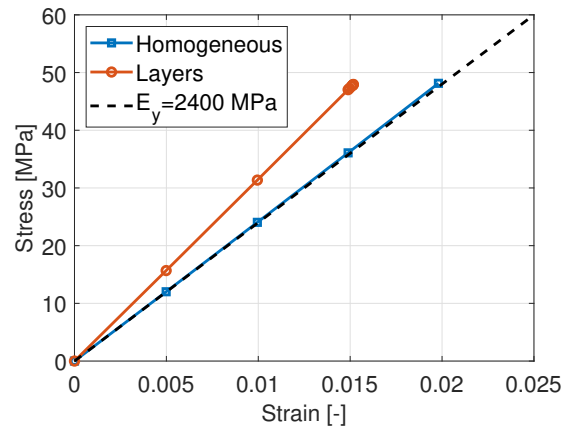
Table 3.5: Mechanical properties used for a single wooden veneer and for homogeneous wood panels.

Parameter	Unit	Wood single veneer	Kerto-Q data sheet	Kerto-S data sheet
E_1	MPa	12 000	10 000	13 800
E_2	MPa	180	2400	430
E_3	MPa	130	130	130
G_{12}	MPa	600	600	600
G_{13}	MPa	380	60	380
G_{23}	MPa	1	22	1
ν_{12}	-	0,2	0,2	0,2
ν_{13}	-	0,45	0,45	0,45
ν_{23}	-	0,35	0,35	0,35
ρ	kg/m ³	510	510	510

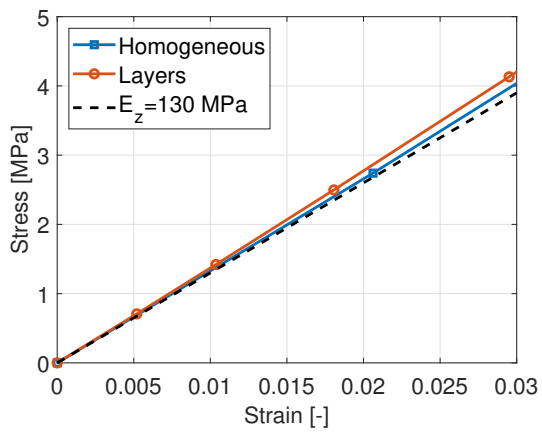
An LVL panel with nine layers oriented as presented in Figure 2.6, and a homogeneous LVL panel was created in ANSA. These were then tested in tension, compression and shear in different directions using Abaqus Unified FEA, using the material parameters presented in Table 3.5. The results from these simulations were then compared, in order to see if the material properties given in the data sheet for the LVL panel were accurate.



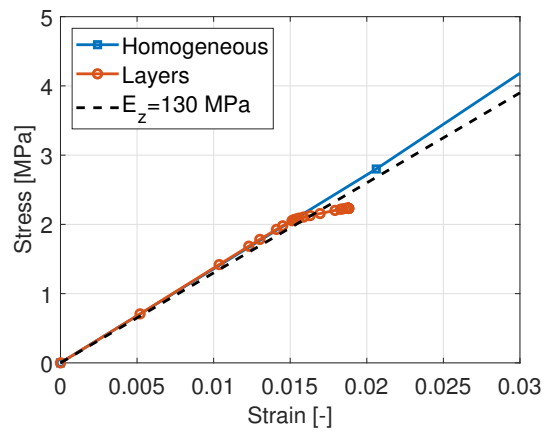
(a) Tension, x-direction.



(b) Tension, y-direction.

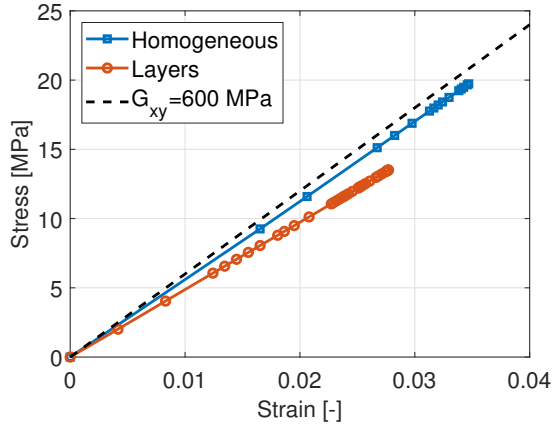


(c) Tension, z-direction.

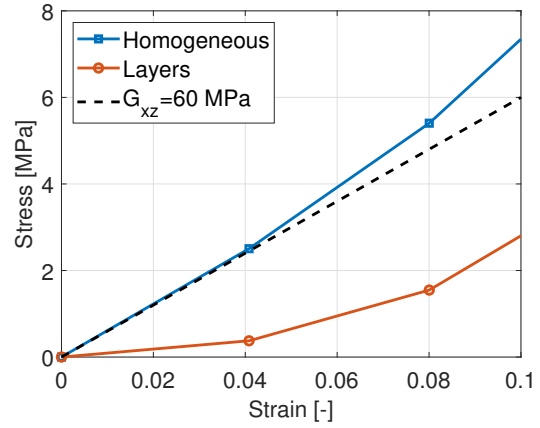


(d) Compression, z-direction.

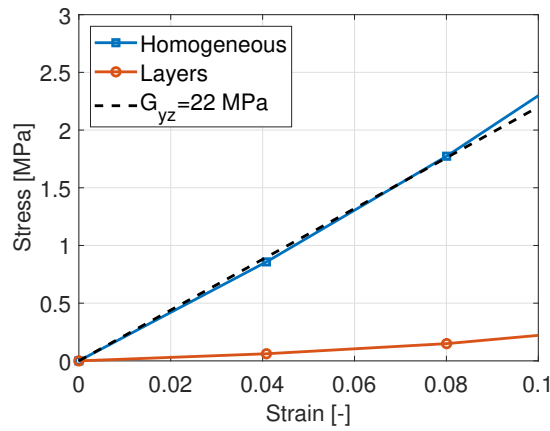
Figure 3.19: Comparison between the LVL-panel with and without considering the layers. x, y, and z-direction.



(a) Shear, xy-direction.



(b) Shear, xz-direction.



(c) Shear, yz-direction.

Figure 3.20: Comparison between the LVL-panel with and without considering the layers. Shear directions.

As can be seen in Figure 3.19 and 3.20a, the results are indeed similar, except for the shear stresses in the xz- and yz-direction. The shear stresses in the xz- and yz-direction does not correspond very well for the homogeneous and layered simulations but since these shear directions are of least significance in this glue joint, this is not likely to propagate into an error source in the full joint simulations.

Also, the material parameters used to model the mechanical properties for each layer are based on tests performed exclusively on plies from the same batch, which may lead to insecurity in the result. Furthermore, the adhesive used to join the plies in order to form the LVL panels, has not been taken into consideration when modeling the panel as a laminate, which may also be an explanation to the difference between the simulation results. Based on this reasoning, and in order to save computational time, the homogeneous orthotropic model was determined to be a good enough representation of the LVL panels. Therefore, the LVL panels were furthermore assumed to be homogeneous and orthotropic.

3.3.2 Material model for the steel

For the steel, accurate test data of the stress-strain curve was provided from SSAB. The plastic part of this data was used as input in ANSA together with the density 7900 kg/m^3 , and the Young's modulus $205\,000 \text{ MPa}$. Figure 3.21 illustrates the true stress-strain curve for the steel, together with the simulation results from both static and dynamic simulations. The reason for running both a static and a dynamic simulation was to compare the outcome of the two different types of solvers. For the case with the dynamic simulation, the specimen broke after reaching a certain stress by using element deletion in Abaqus Unified FEA, which is difficult when performing a static analysis. The reason for using element deletion was since the task is to recreate the physical test data for the full joint, which indeed breaks when a large enough force is applied.

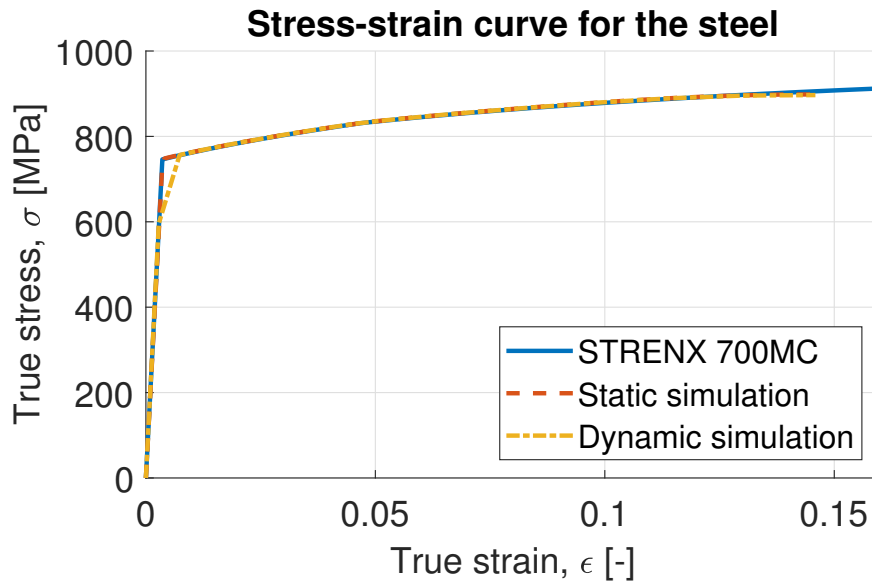


Figure 3.21: Stress-strain curve for STRENX 700 MC E and corresponding simulations.

From the simulations, the engineering strains and stresses were provided. Since the provided data from SSAB was the true stress-strain curve, the simulation data needed to be converted. The true stress, σ_t , and the engineering stress, σ_e , were calculated according to,

$$\sigma_t = \frac{F}{A} \quad (3.5)$$

$$\sigma_e = \frac{F}{A_0} \quad (3.6)$$

where F is the reaction force caused by the applied displacement, A is the actual instantaneous area, and A_0 is the initial area. Consistency of volume gives that $V = A \cdot L = A_0 \cdot L_0$ and the engineering strain is defined as $\varepsilon_e = (L - L_0)/L_0 = L/L_0 - 1$. Hence the true stress can be written as,

$$\sigma_t = \frac{F \cdot L}{A_0 \cdot L_0} = \frac{F}{A_0} (1 + \varepsilon_e) = \sigma_e (1 + \varepsilon_e) \quad (3.7)$$

The true strain is defined as the change in length with respect to the instantaneous length as,

$$\varepsilon_t = \int_{L_0}^L \frac{dL}{L} = \ln\left(\frac{L}{L_0}\right) \quad (3.8)$$

Since the instantaneous length can be expressed as $L = L_0(1 + \varepsilon_e)$, the true strain can be expressed as,

$$\varepsilon_t = \ln(1 + \varepsilon_e) \quad (3.9)$$

The reason why the graph for STRENX 700 MC E continues further than the graphs obtained by the simulations depends on the geometry of the model created in ANSA as well as how the data was analyzed and plotted using META. The true fracture strain is as high as 0.48, although it does not keep a stable neck and the macro strain hence stays below 0.15. The graphs coincide well for lower strains before the neck formation, which is expected.

3.3.3 Material model for the glue

As previously mentioned, the glue was treated as a variable all the way to the final simulations, but in order to have a base to work from, a minor material validation was made. The only material parameters that were given for the glue were the Young's modulus equal to 1560 MPa, the tensile strength equal to 25–30 MPa and the elongation at fracture equal to 2%. Based on these values a material model could be created such that it satisfied these values. Since the data sheet for the glue did not specify if the fracture strain were given in plastic strain or total strain, both these alternatives were considered when validating the material model for the glue. When running the simulations, a dynamic explicit analysis was used in order to be able to model the failure of the glue using element deletion.

The results from the simulations can be seen in Figure 3.22. As can be seen the Young's modulus is close to 1560 MPa for them both and the fracture occurs at either 2% total or plastic strain at a stress somewhere near 25–30 MPa. These two material models were later used as the base for the glue when evaluating the simplified and the full model.

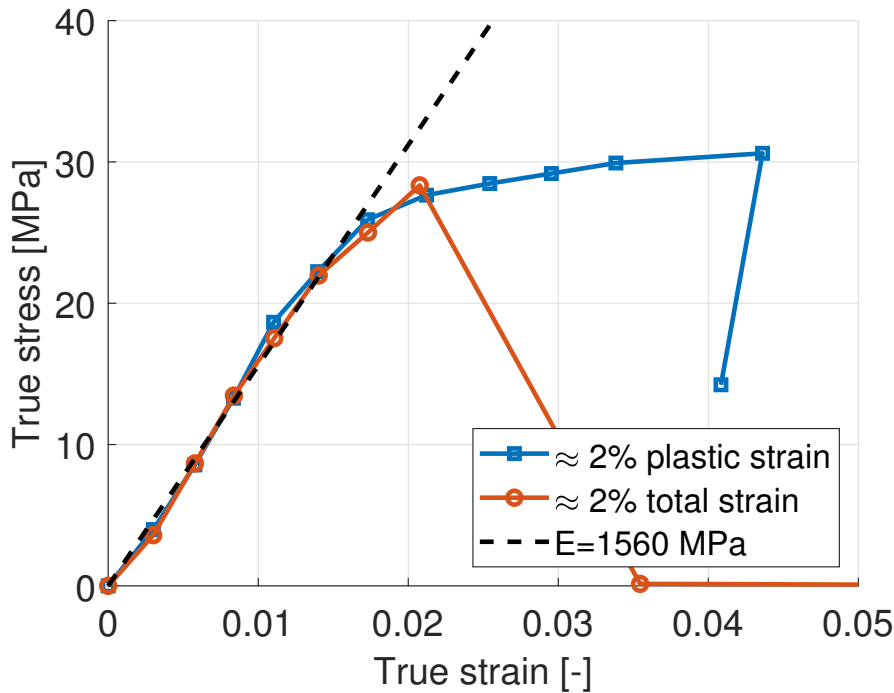


Figure 3.22: The stress-strain curve for two different glue material models obtained using dynamic explicit analysis.

In the model with 2% total strain the plastic strain were set to 0,5%, in order to replicate some kind of brittle failure. For both cases the plastic stresses were in the range of 25–30 MPa. Another way of simulating a brittle failure using Abaqus Unified FEA is to apply brittle cracking instead of ductile plasticity when defining the material in ANSA. The reason for not using this approach was because additional unknown variables needed to be defined in order to describe the mechanical behaviour of the glue, in comparison to the ductile plasticity model. In order to obtain accurate values of these variables, additional physical tests needed to be performed, which was not possible due to the time limit of this project. Therefore, the ductile plasticity model were used for both the glue and the steel.

4

Simplified model

When the material models for the wood and the steel had been validated, the next step was to develop a simplified model of the joint. This was done in order to perform some quick simulations to get an idea of how different input parameters affect the response of the entire model. It was also used to see if there is any resemblance between the obtained simulation results and the physical tensile test results provided by Modvion. The simplified model was also used in order to test how the different types of material parameters in the glue affect the result of the entire joint, and what material model of the glue that gives the most accurate result compared to the physical test data. The influence of the different types of contacts was also investigated using the simplified model.

The simplified model was created based on the Computer Aided Design (CAD)-model of the full joint provided by Modvion, see Figures 2.3 and 2.4. Some illustrations of the simplified model can be seen in Figures 4.1 and 4.2. The simplifications that were made compared to the full CAD-model were that the plates used for fastening the joint during the tensile tests were removed, only one of the ten LVL panels were considered and the steel plate only consisted of one line of holes. The attachment zones could be removed because of the possibility to use boundary conditions directly on a surface in the simulations, hence no bolted connections to the testing machine were needed. This further reduced the complexity of the model, resulting in reduced computational cost. Also, since the model is analyzed with respect to tension, the compression plates were removed since they have no impact during tension.

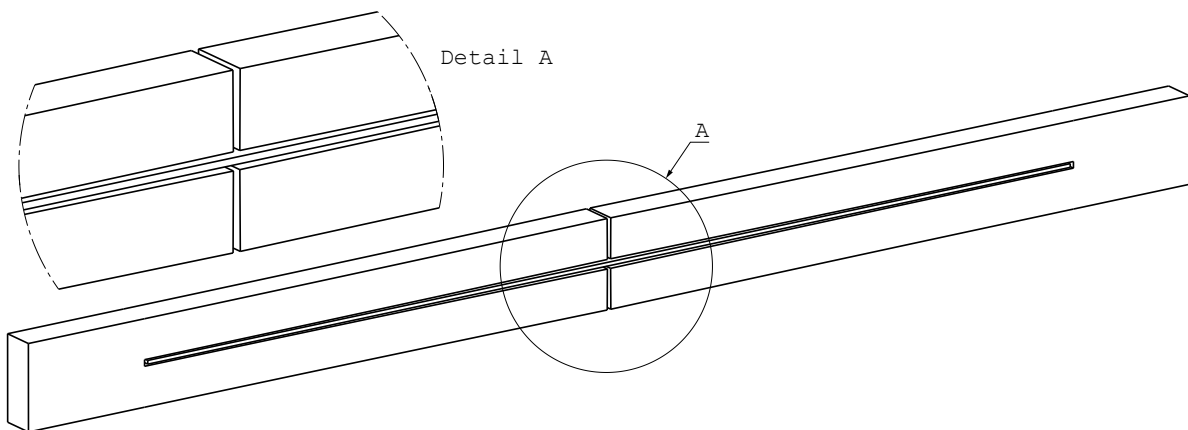


Figure 4.1: The simplified model, which is a tenth of the full joint.

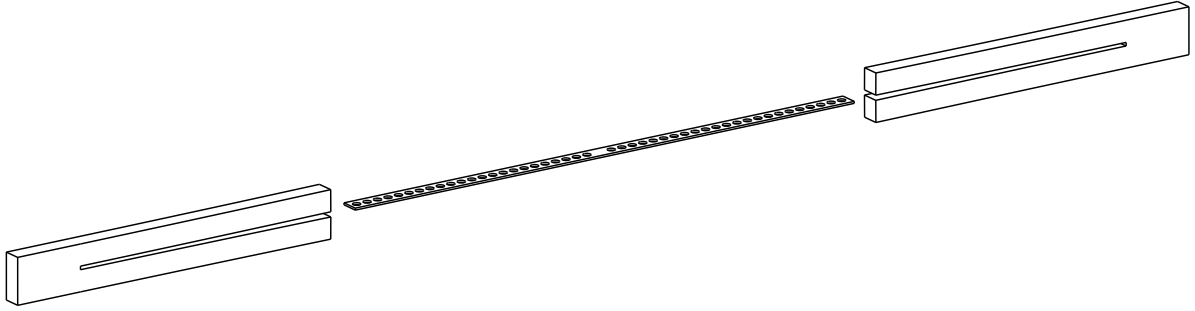


Figure 4.2: Explosion view of the simplified model.

The simplified model was used in order to test different material models for the glue, combined with different interpretations of the contacts between the different materials. The reason for modifying these parameters, was because these were the remaining insecurities in the model after the material validation. In addition to this, a comparison between static implicit analysis and dynamic explicit analysis was made. This was done to ensure that the correct analysis parameters were used in the dynamic simulation in order to retain the necessary degree of accuracy of the solution.

In order to be able to compare the results obtained from the simulations on the simplified model, to the physical test data, the reaction force due to the applied displacement was multiplied by ten. This was done as an approximation since the full model consists of ten LVL panels glued together and the simplified only consists of one panel, resulting in lower reaction forces.

4.1 Type of contacts between the materials

In order to get as good fit to the physical test results as possible, different types of contacts between the glue and the steel were tested individually. The reason for not studying the contact between the wood and the glue was because it was concluded from the analysis of the extracted cross sections of the joint that the glue and the wood are still in contact even after the fracture of the joint. Therefore the nodes between the wood and the glue were pasted, as a way to resemble a full contact, with no sliding between the materials, which means that the materials shared nodes on the interaction surfaces.

First, a static implicit analysis was run with no defined contact between the steel and the glue, instead the nodes in the interactions between the different materials were pasted. The second type of interaction that was tested was a model with a no-friction-contact between the glue and the steel, while the interaction between the glue and the wood remained pasted.

The reason for testing these two types of contacts was because they acted as opposite extremes to each other. By testing these contacts it was possible to identify the range in which the fracture stress occurs. Thus it gives an idea if it is possible to obtain the correct fracture behaviour by modifying the contact between the glue and the steel, or if the problem lies elsewhere. The results from these simulations can be seen in Figure 4.3.

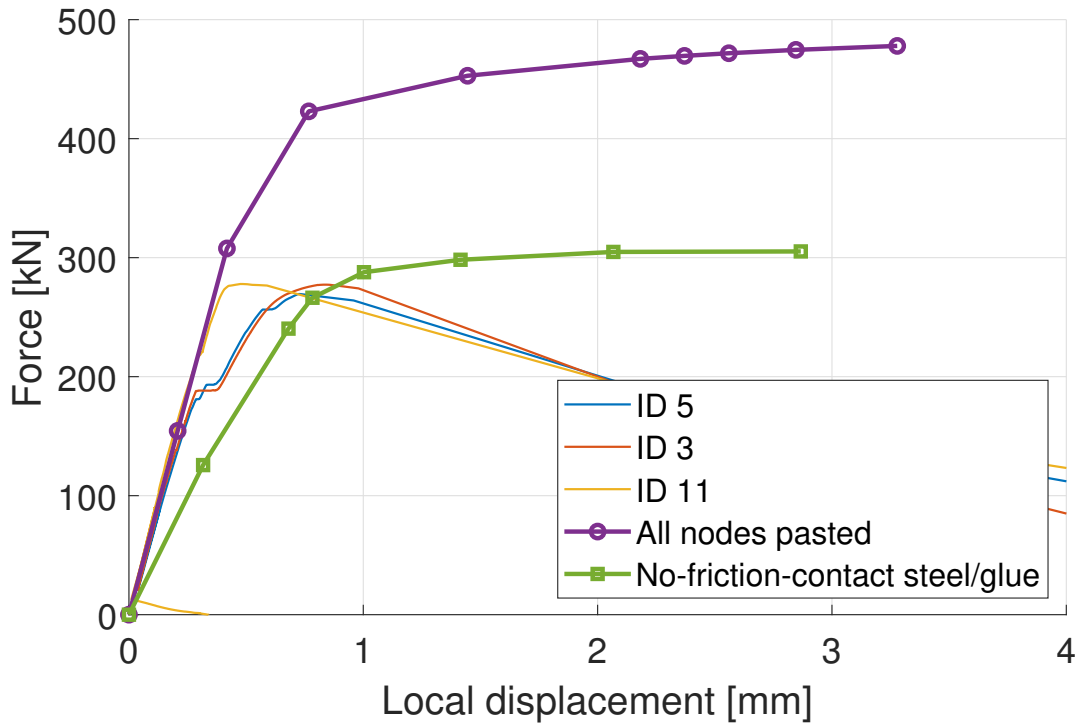


Figure 4.3: Different types of contacts between the glue and the steel in the simplified model.

By looking at Figure 4.3, it can be observed that the slope of the elastic part of the curve decreases when applying the no-friction-contact between the glue and the steel. It can also be seen that the applied force needed in order to reach the plastic zone decreases and comes closer to the physical test data, compared to the model with all nodes pasted. Thus, it can be concluded that pasted nodes between the steel and the glue gives a better representation of the reality in the elastic zone of the curves, while the no-friction-contact gives a better representation in the plastic region.

One way of replicating both these behaviours in one model, is to define a cohesive behaviour in the interaction between the glue and the steel. Cohesive contact behaviour is commonly used when modeling bonded interfaces in which the bond may damage and fail as a result of the loading. In this case the cohesive bonding is limited to original contact constraints which means that Abaqus Unified FEA limits the cohesive bonds to those that exists in the beginning of the simulation [41]. For the cohesive behaviour, the linear elastic traction-separation behaviour in Abaqus Unified FEA was used, which is explained in the following section.

4.1.1 Traction-separation model for cohesive contacts

The traction-separation model assumes initially elastic behaviour, which is then followed by the initiation and evolution of damage [41]. So, by adapting this behaviour between the steel and the glue, the elastic region from the model with the pasted nodes could be captured, as well as the plastic region from the model with the no-friction-contact, by introducing damage at a certain strain. When the damage criterion was fulfilled the contact between the steel and the glue disappeared, hence the no-friction behaviour could be achieved.

The elastic part of the traction-separation model is written in terms of an elastic constitutive matrix that relates the nominal stresses to the nominal strains across the interface. The elastic behaviour can hence be written as,

$$\mathbf{t} = \begin{Bmatrix} t_n \\ t_s \\ t_t \end{Bmatrix} = \begin{bmatrix} K_{nn} & K_{ns} & K_{nt} \\ K_{ns} & K_{ss} & K_{st} \\ K_{nt} & K_{st} & K_{tt} \end{bmatrix} \begin{Bmatrix} \delta_n \\ \delta_s \\ \delta_t \end{Bmatrix} = \mathbf{E}\boldsymbol{\delta} \quad (4.1)$$

where \mathbf{t} is the nominal stress vector which consists of three components, t_n , t_s , and t_t , which represents the normal traction and two shear tractions, respectively. δ_n , δ_s and δ_t are the corresponding separations. For simplifications, uncoupled traction-separation behaviour was used, which means that only the components in the diagonal of the stiffness matrix, \mathbf{K} , needed to be defined.

As discussed above, the initial response of the cohesive contact is assumed to be linear. When the damage criterion are met, material damage will occur according to a damage evolution law defined by the user. A typical traction-separation response with a failure mechanism can be seen in Figure 4.4.

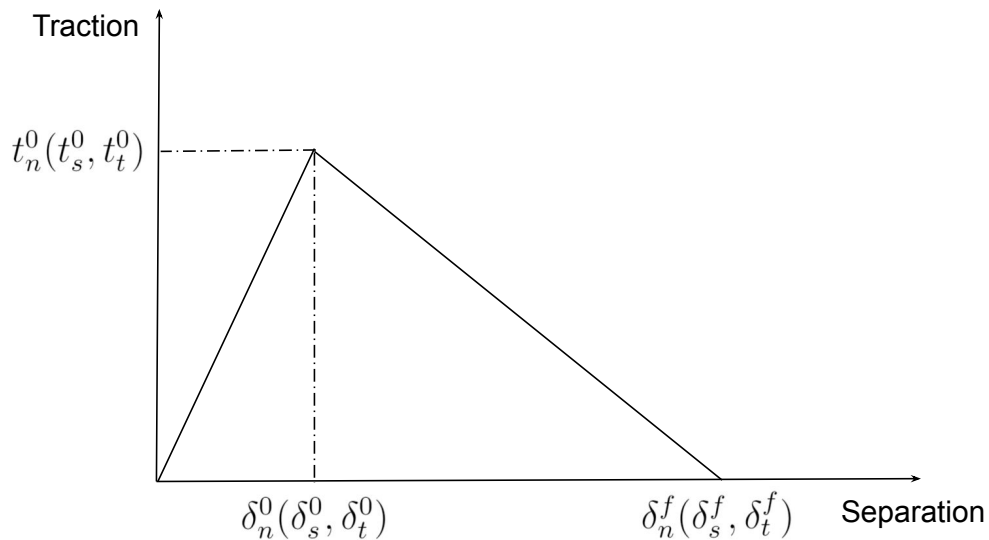


Figure 4.4: Typical traction-separation response

There are different ways to define the damage initiation, which refers to the beginning of degradation of the response of a material point. When the stresses and/or strains satisfy the specified damage initiation criteria, the process of degradation begins. In this project the maximum stress criterion was used when modeling the cohesive contact. The criterion can be represented as

$$\max \left\{ \frac{t_n}{t_n^0}, \frac{t_s}{t_s^0}, \frac{t_t}{t_t^0} \right\} = 1 \quad (4.2)$$

which means that damage is initiated when the maximum contact stress ratio reaches a value of one. In the equation above t_n^0 , t_s^0 and t_t^0 represent the peak values of the contact stress when the deformation is purely normal to the interface or purely in the first or second shear direction, respectively.

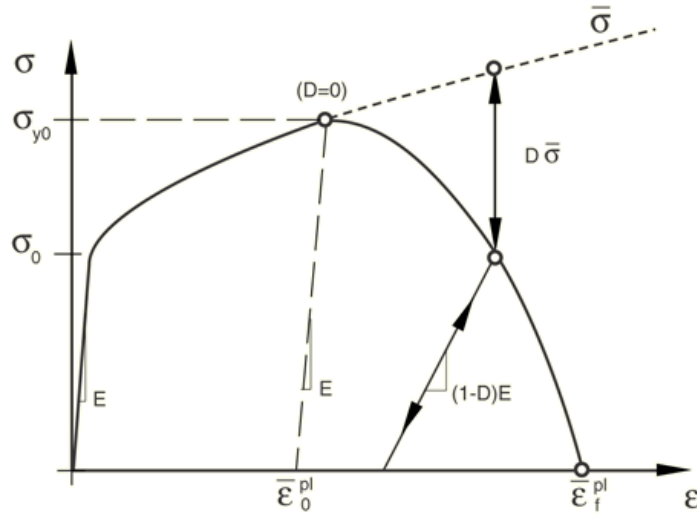


Figure 4.5: Stress-strain curve with progressive damage degradation [6].

The damage evolution can then be described using a scalar damage variable, D , which represents the overall damage at the contact point. The damage evolution law describes how fast the cohesive stiffness is degraded once the damage initiation criterion is reached. Initially the damage variable has the value 0, and when damage evolution is modeled, D , evolves from 0 to 1 when loaded further than the initiation of damage. An illustration of a stress-strain response with progressive damage degradation can be seen in Figure 4.5. The contact stress components of the traction-separation model are affected by the damage variable according to

$$\begin{aligned} t_n &= (1 - D)\bar{t}_n, & \bar{t}_n &\geq 0 \quad (\text{No damage during compression}) \\ t_s &= (1 - D)\bar{t}_s \\ t_t &= (1 - D)\bar{t}_t \end{aligned}$$

where \bar{t}_n , \bar{t}_s and \bar{t}_t are the stress components predicted by the elastic traction-separation behaviour for the current separations without damage.

The inputs used when simulating the cohesive contact behaviour between the glue and the steel are presented in Table 4.1. The contact stiffness in the normal direction are set equal to the Young's modulus, and the shear contact stiffness in the shear directions are set equal to the shear modulus for the glue. The maximum contact stresses t_n , t_s and t_t are chosen based on the hypothesis that the contact between the steel and the glue fails before the glue itself, which has a tensile and shear strength of 25–30 MPa and 79,9 MPa, respectively. Since the glue is considered to be brittle the displacement at failure were set to 0.

Table 4.1: Mechanical properties used to define the cohesive contact behaviour between the wood and the glue

Parameter	Unit	Value
K_{nn}	MPa	1560
K_{ss}	MPa	1310
K_{tt}	MPa	1310
t_n	MPa	25
t_s	MPa	70
t_t	MPa	70
Disp. at failure	mm	0

The result from the simulation with the cohesive contact compared to the results obtained from the simulations with all nodes pasted and the no-friction-contact between the glue and the steel, can be seen in Figure 4.6.

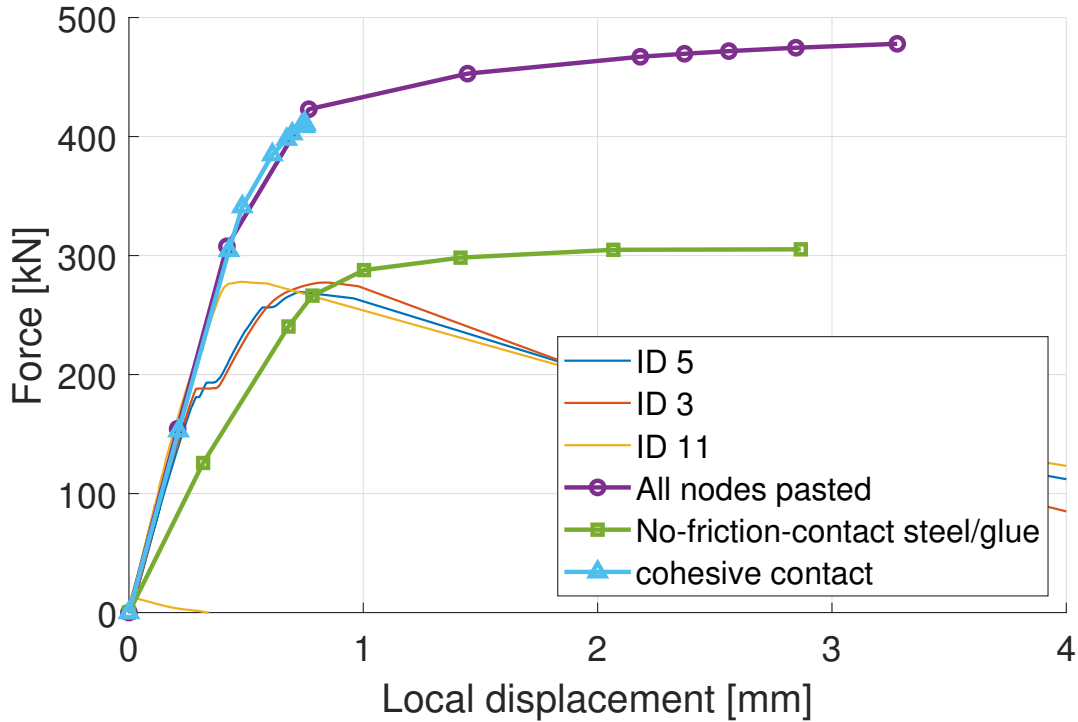


Figure 4.6: The force-local displacement response obtained from the simulations with the different kind of contact interpretations

Due to some convergence issues the simulation did not run the entire specified time period. Although, it is possible to see an indication of that the curve deviates earlier than the curve representing the result with all nodes pasted. It can also be seen that the correct stiffness is captured, as expected. Hence, it can be concluded that the force needed in order for the joint to enter the plastic region can indeed be lowered by implementing a cohesive contact between the glue and the steel.

However, there are too many insecurities when it comes to the different input parameters used when implementing the cohesive contact. For example, physical tests are required in order to find the correct values of the contact stiffness's in the normal and shear direction, as well as the maximum contact stiffness's allowed. Since the tools needed in order to perform these kinds of tests were not available, it was determined to continue using the all-nodes-pasted-approach in the upcoming simulations.

4.2 Material models for the glue

As stated in Section 3.3.3 there was some uncertainty when it came to which material model that should be used to model the glue. In order to investigate how the glue affects the response of the entire joint, a comparison was performed with four different glue models. The material models developed in the material validation of the glue were used as a base for these simulations. The joint was tested with both 2% total and plastic strain. In addition to this, different plastic stress ranges were investigated as well. The results from these simulations can be seen in Figure 4.7.

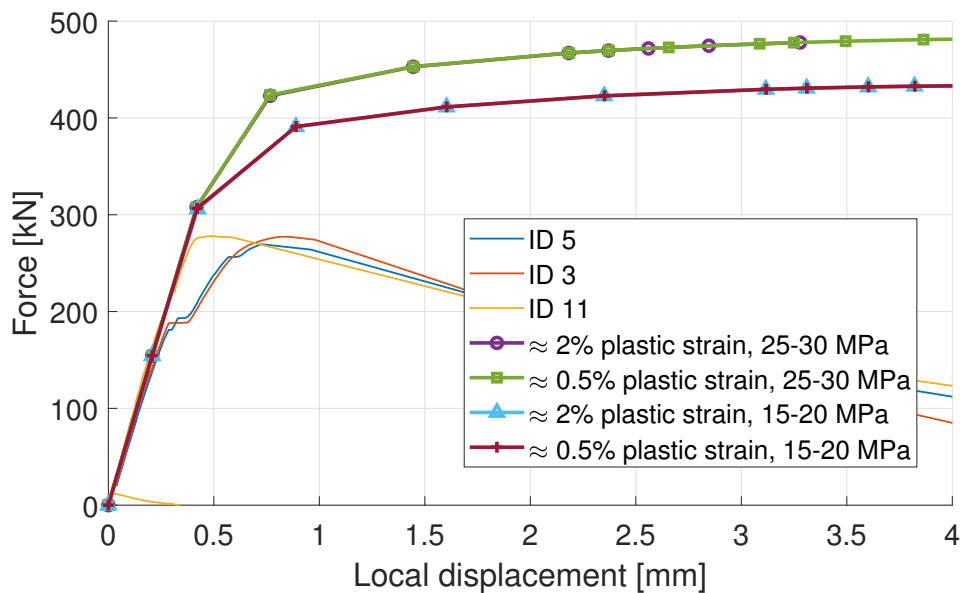


Figure 4.7: Comparison of different glue material models, compared to the physical test data.

As can be seen in Figure 4.7, only the plastic stress range seems to affect the result for the simplified model. Lower plastic stress range of the glue results in a decrease in the force needed in order for the response of the simplified model to reach the plastic region, which is expected. The plastic strain in the glue does not seem to affect the response for the simplified model, at least not when running a static implicit simulation with no damage initiation. The reason for not capturing the softening of the test data, is because there is no damage initiation and evolution implemented in the simulation. The same goes for the analyses performed in the following section.

4.3 Different types of analyses

The test data that is to be recreated consists of both a linear part, i.e the elastic region, and a nonlinear part, i.e the plastic region. In order to capture both these behaviours, together with the fracture of the joint using element deletion, a dynamic explicit analysis combined with mass scaling was used. Mass scaling was used in order to reduce the computational cost of the simulations. In order to ensure that the inertia forces created by the mass scaling would not dominate and change the solution, a comparison between a static implicit and a dynamic explicit analysis was made, with different values on the mass scaling factor, f^2 and with no damage initiation. In Figure 4.8, the result for these simulations can be seen together with the data from the physical tensile tests performed by Modvion.

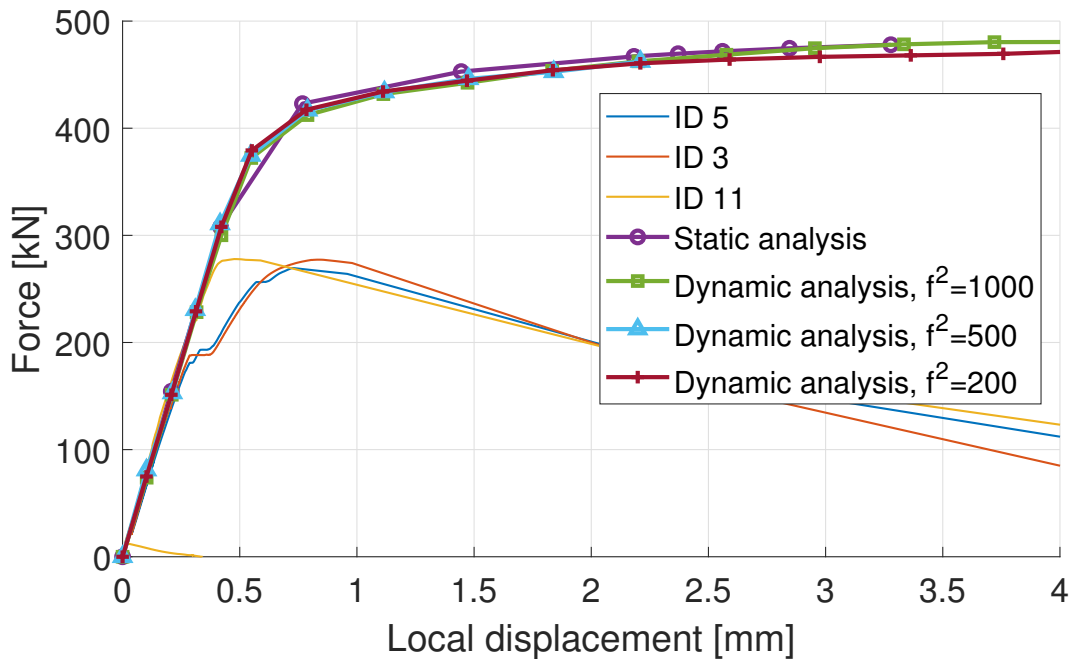


Figure 4.8: Simulation results from static implicit and dynamic explicit with different values of the mass scaling factor, f^2 , compared to the physical test data.

As can be seen, the difference between the simulation results obtained with the different values on the mass scaling factor is small. However, when investigating the ratio between the kinetic and internal energy presented in Figure 4.9, which should not be higher than 10% in order to retain accuracy, it is easy to draw the conclusion that higher mass scaling factor results in higher inertia forces, which is not desirable. Hence, the lower the mass scaling the better. For dynamic analyses, especially with mass scaling, the way that the velocity is applied can be important. Since the displacement increases linearly due to the applied velocity in the simulations, the accelerations are very large in the first load increment causing the forces from $F = ma$ to be very high. This could explain why there is a peak in the energy ratio at the first load increments.

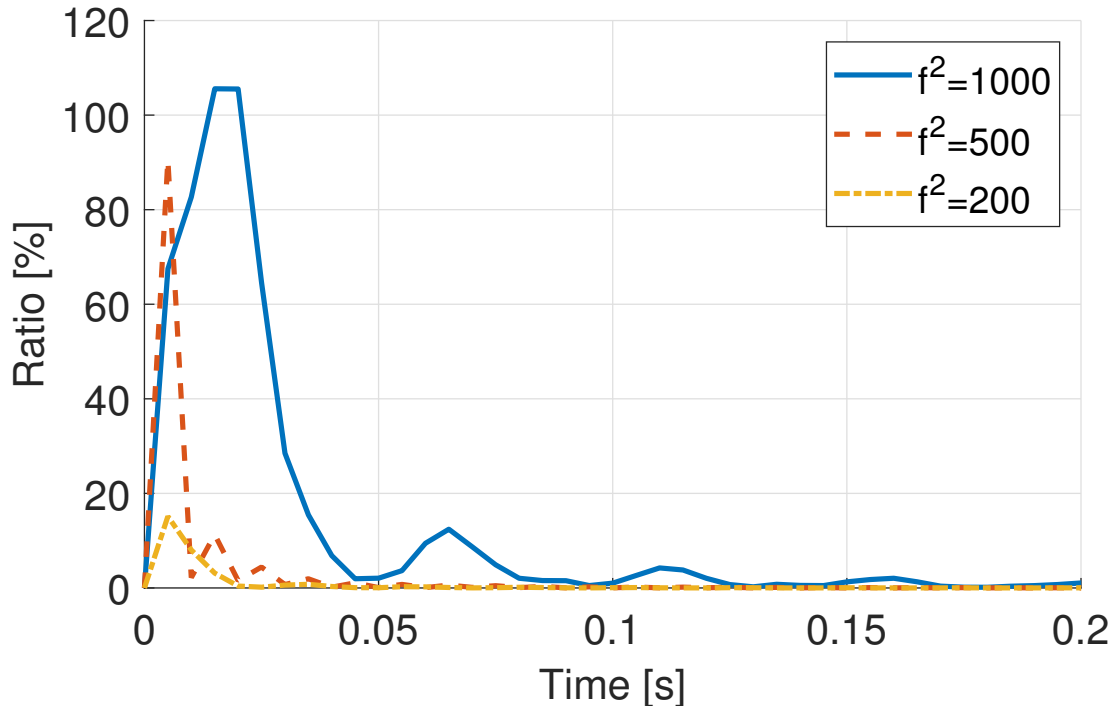


Figure 4.9: The ratio between the kinetic energy and the internal energy. In order to ensure that there is no significant change to the solution the ratio should preferably be less than 10%.

4.3.1 Calibration of simulation parameters

In order to reduce the computational cost while still maintaining reasonable reliability and accuracy, a small parameter study was performed on some simulation parameters for dynamic explicit analysis with element deletion implemented in Abaqus Unified FEA. The velocity of the displacement, v , the time period, T , and the fixed mass scaling factor, f^2 , was altered in four different combinations shown in Figure 4.10. The simulation results varies a bit, although no clear trend can be observed by only studying the Force-Local displacement plot.

Figure 4.11a shows the computation times for the different simulations. It is clear that the time period and the mass scaling both affects the computation time significantly, as expected. Shorter time period and higher mass scaling gives larger dynamic effects in the simulation, but also lowers the simulation time. The fact that the simulations with shorter time and larger mass scaling factor gives larger dynamic effects caused by inertia forces, can be seen in Figure 4.11b.

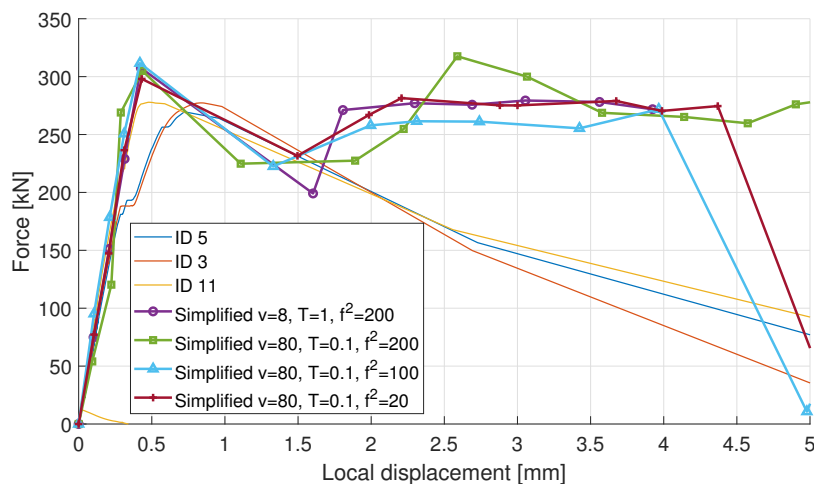


Figure 4.10: Different simulation parameters for dynamic explicit compared to test data.

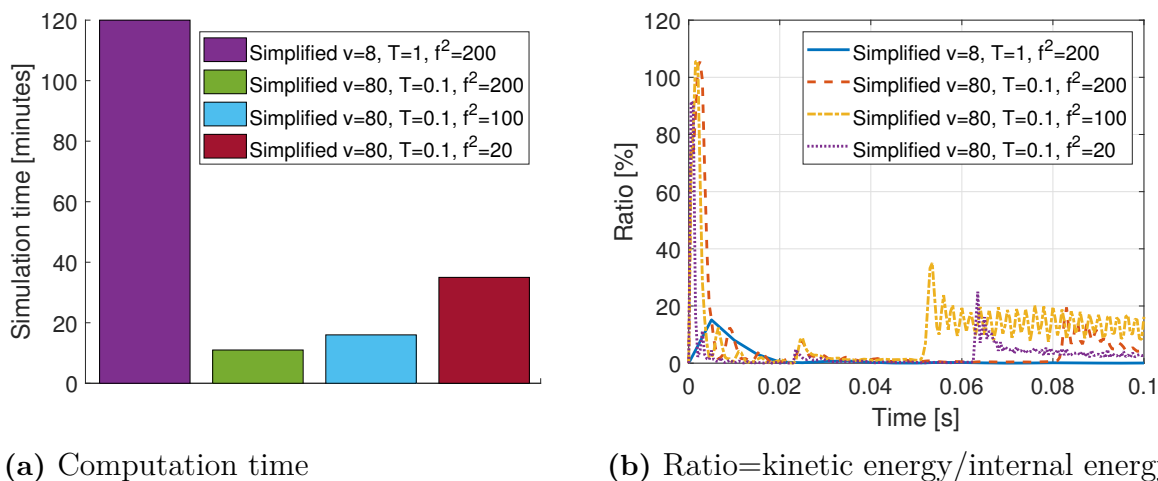


Figure 4.11: Comparison of computation times and the ratio between kinetic and internal energy for different simulation parameters for dynamic explicit.

Clearly, the response of the simulation with velocity, $v = 8$, time period, $T = 1$ and mass scaling factor $f^2 = 200$, are least affected by the dynamic effects, since the energy ratio remains well below the preferred 10% during almost the entire simulation. However, the computation time for this simulation was 120 minutes compared to the second longest, which was only 40 minutes. When looking at the ratio between the kinetic energy and the internal energy for the second longest simulation, the ratio is above 10% for a short

time in the beginning of the simulation and then in the end, after the failure of the joint. During the majority of the simulation time, the energy ratio is much less than the preferable 10%. Therefore, as the best compromise between accuracy and computational cost, $v = 80; T = 0,1; f^2 = 20$ were chosen as simulation parameters for the following simulations. In order to get more accurate results, longer simulations with preferably no mass scaling would be required, but since there was a limited time frame for the project, this was not possible.

5

Full model

When the desired results had been obtained with the simplified model, a full scale model of the joint was developed. The development of the full-scale FE-model was an iterative process and started as the geometry of the full joint but with some simplifications when it came to what material models that were used and if all layers were considered or if the wood was considered as a homogeneous and orthotropic material. Based on the analysis in Section 3.3.1 and in order to reduce the computational cost, the wood was continued to be treated as a homogeneous and orthotropic material for all simulations. The homogeneous orthotropic material parameters were based on data sheets for Kerto-Q, and are listed in Table 3.5. An illustration of the full-scale model can be seen in Figure 5.1.

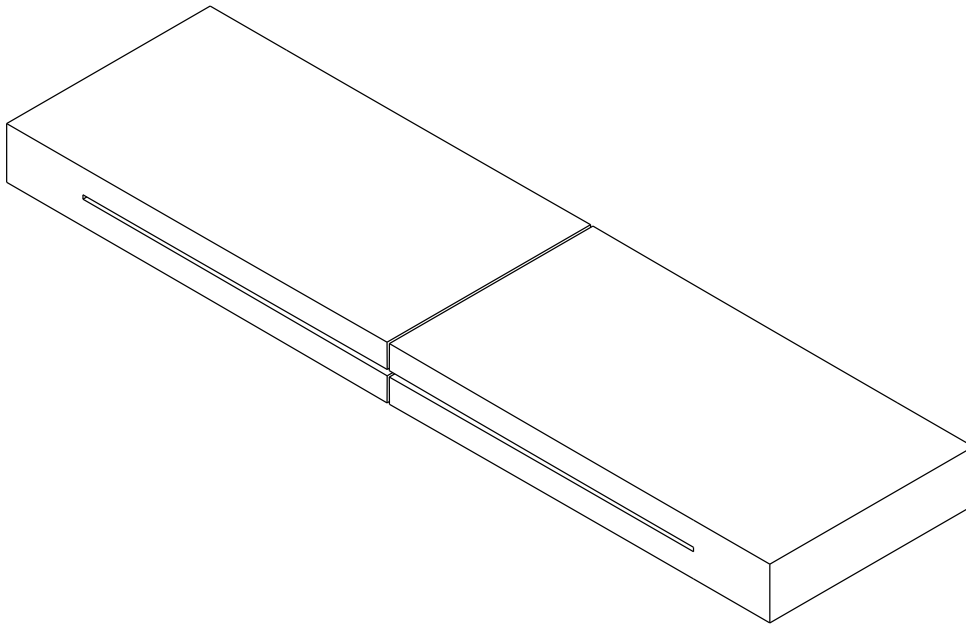


Figure 5.1: Illustration of the full-scale model.

A number of simulations were run for each step in the process of obtaining the final full-scale model of the joint. The results from each step were analysed and compared to the physical test results from the tensile tests. Based on the comparisons between the simulations and the physical test data, modifications of the FE-model were made in order better fit the data.

Before starting the development of the final FE-model a small parameter study of the influence of the Young's modulus and the Poisson's ratio of the glue was performed on a full model simulation, in order to investigate the overall effect of these properties. This was interesting since only one of these properties, the Young's modulus, was given for the glue, while the Poisson's ratio was unknown. Both the Young's modulus and the Poisson's ratio were changed in different simulations. The results can be seen in Figure 5.2 with the parameters in the legend.

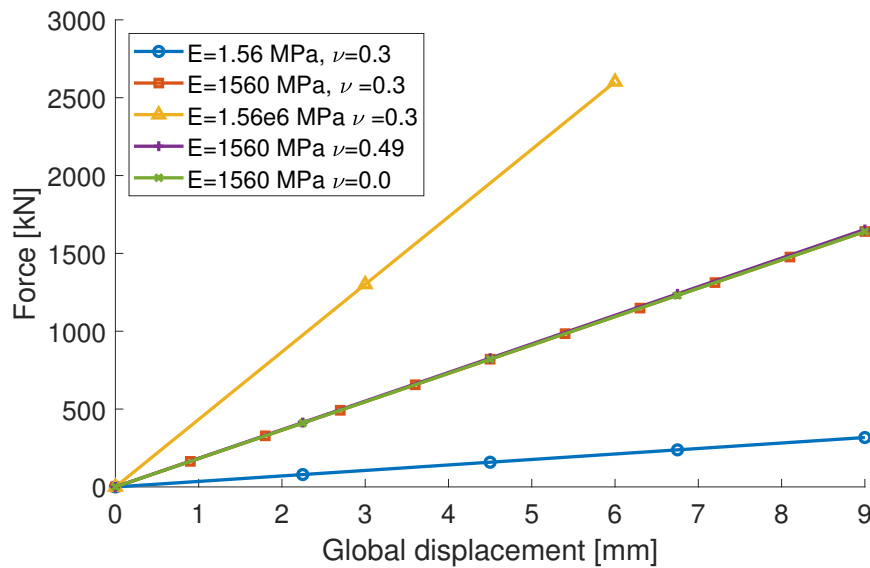


Figure 5.2: Results from simulations with drastically changed glue properties. The red line is the original data sheet properties.

It can be concluded that the Young's modulus has a large effect on the outcome, while the effect of the Poisson's ratio can be neglected. Based on this result, the decision was made that there was no need to invest more time in trying to find the correct value of the Poisson's ratio, since it does not have an effect on the final response of the full model.

5.1 Steel plate only

Based on the knowledge that the HSK-system is designed in such a way that the steel plate yields before the wood cracks, and that the glue starts to crack before the steel plate fails, the hypothesis was made that the steel plate carries most of the load. In order to investigate this, simulations were performed on only the steel plate. These simulations were then compared with the physical test data for the entire joint, in order to see if there was any resemblance. The simulations were performed with a longitudinal symmetry (xz-plane) and boundary conditions applied directly on the far edges of the steel plate. The results from these simulations can be seen in Figure 5.3.

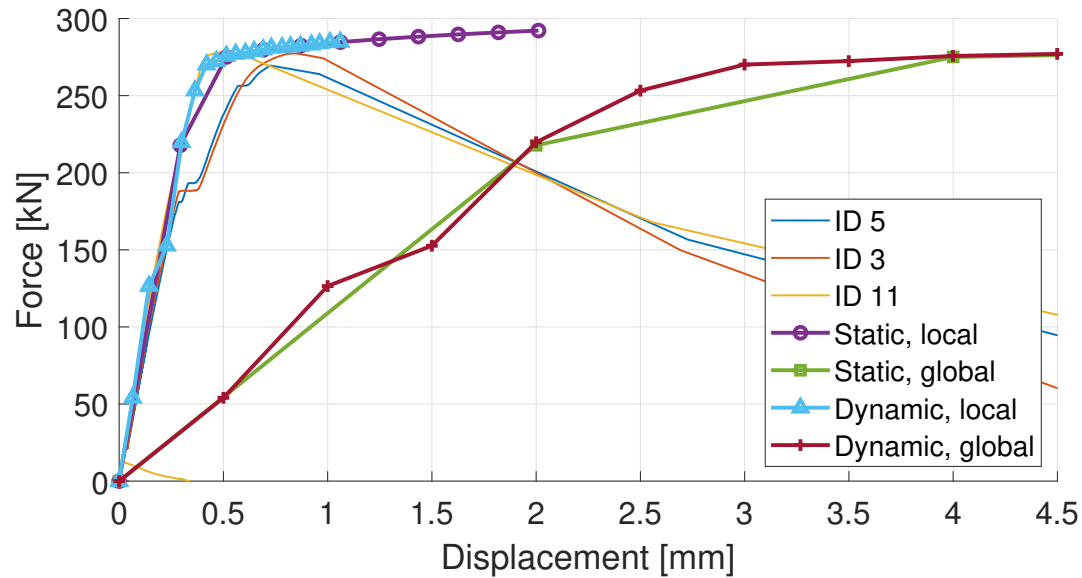


Figure 5.3: Simulation results for the steel plate only, without glue and wood. Displacement was measured both locally (45 mm from the horizontal symmetry line) and globally (at the ends where the boundary conditions are applied).

The reaction forces obtained from the simulation are plotted both against the global and the local displacement in Figure 5.3. The local deformations are measured in the same way as for the physical joint, which is approximately 45 mm from the horizontal symmetry line of the joint, while the global deformation is measured in the point where the displacement is applied, see Figure 5.4.

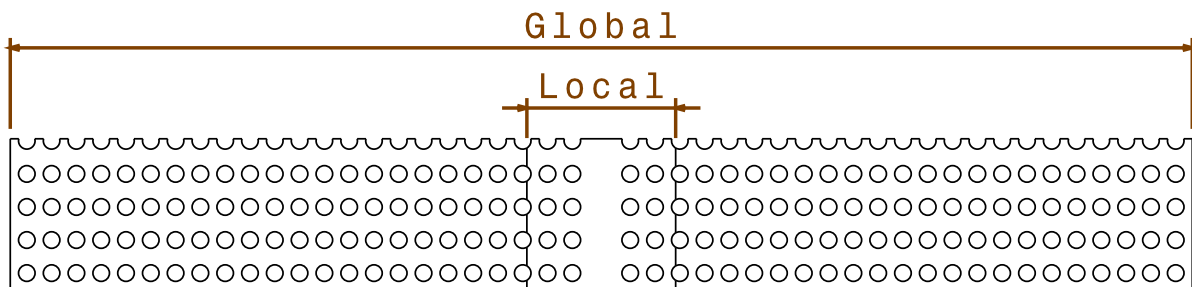


Figure 5.4: An illustration of how the local and the global deformations are measured on the steel plate

The curves for the local displacement follows the stiffness for the physical tests results very well, which implies that the wood and the glue does not affect the overall stiffness in the local region close to the horizontal symmetry line of the joint much at all. Furthermore, when measuring the displacement globally on the steel plate it shows a lower stiffness curve. This is because of the longer measuring range which includes a larger number of holes, which lowers the overall stiffness.

The yield limit on the steel plate corresponds almost perfectly to the yield limit in the test data, which is very much expected since it is known that the full joint breaks in the steel. Hence, the hypothesis that the steel plate carries most of the loading as soon as the glue cracks, is confirmed. This implies that, in order to accurately replicate the physical test data and capture the softening of the curve, failure in the form of damage initiation and evolution, needs to be implemented in the glue and the steel such that glue fails first followed by the steel. In order to implement this type of failure in the model, element deletion was used.

5.2 Tuning of glue material parameters

Since the data for the Loctite CR 421 Purbond was still quite insecure when the development of the full model was performed, and that the conducted tests on the glue showed results far from the data sheet, it was decided to try different glue material models on the full model as well. This was done in order to try to calibrate the simulation to replicate the test results.

The stiffness of the model have shown to be quite accurate when using the Young's modulus of the glue given in the data sheet, 1560 MPa. Although, the failure load has been too high when the glue failure stress was set to 30 MPa. Therefore the Young's modulus from the data sheet were kept while the plastic stress range was lowered in several steps. Figure 5.5 shows the different plastic stress ranges that were tested.

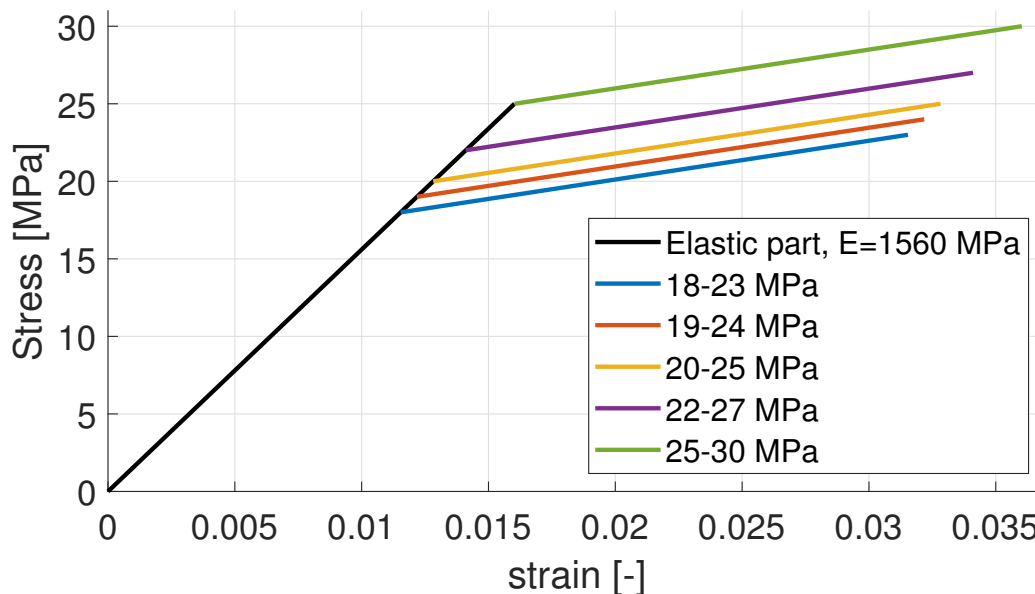


Figure 5.5: The different glue plasticity levels that were tested. The real curve is probably smooth.

The plastic stress ranges from Figure 5.5 were simulated both on the simplified and the full model. The results from the simulations are shown in Table 5.1 and Figure 5.6.

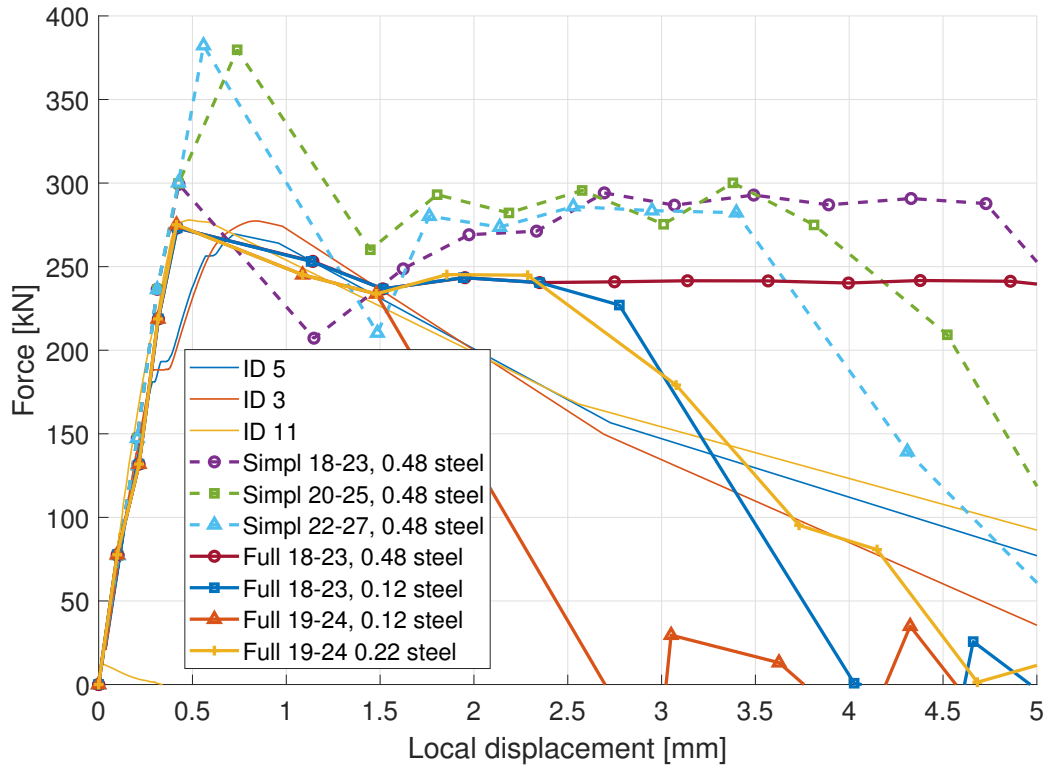


Figure 5.6: Simulation results at the different glue plasticity levels. Also the brittleness of the steel was altered.

Table 5.1: Simulation results for different glue plasticity levels.

ID	Plasticity level	Model	Steel failure strain	Steel fracture	Max load
1	18–23 MPa	Simplified	0,48	First row	300 kN
2	20–25 MPa	Simplified	0,48	First row	380 kN
3	22–27 MPa	Simplified	0,48	First row	382 kN
4	18–23 MPa	Full	0,48	No	275 kN
5	18–23 MPa	Full	0,12	First row	275 kN
6	19–24 MPa	Full	0,12	Third row	275 kN
7	19–24 MPa	Full	0,22	Third row	275 kN

It is clear that the simplified model cannot be directly compared to the full model in this case. The max loads are significantly higher on the simplified model with the same parameters. It is also likely that none of the simulations are very accurate since the variation in results does not clearly correspond to the parameter differences. This could be an error caused by the implementation of element deletion.

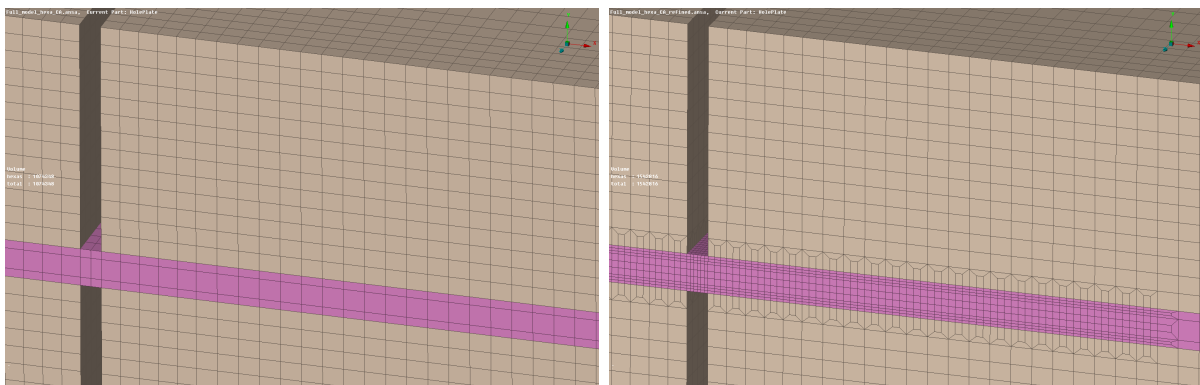
The simulation with ID 5 in Table 5.1 is clearly closest to reality regarding both maximum load and fracture behaviour. Hence these parameters were chosen for future simulations: Glue plasticity level 18–23 MPa, Steel fracture strain 0,12.

5.3 Mesh

As discussed in Section 2.8.1, the mesh size is of big significance when element deletion is implemented. If the elements that are removed are too large this affects the accuracy of the solution. From the physical tensile tests it was known that the components of the joint that fails are the steel and the glue, while the wood remains intact. Therefore, element deletion were only implemented on the glue and the steel. Hence, the mesh size of the wood did not need refining and were left relatively coarse throughout all the remaining simulations.

Three different meshes were used for the full model; coarse, refined 1, and refined 2. The coarser mesh, see Figures 5.7a and 5.8a, was used initially to quickly calibrate the different materials and simulation parameters. When this was done, the refined meshes were used to create a finer visualization of the stress distribution and to investigate the mesh size dependency.

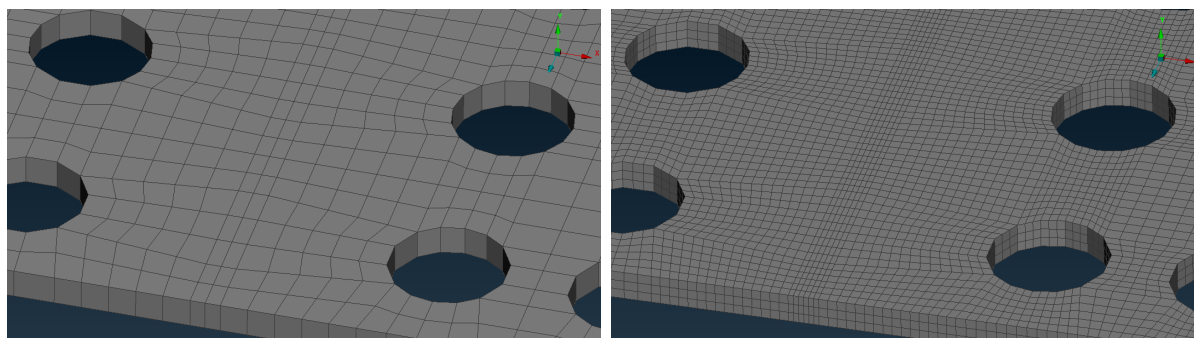
The refined 1 mesh was refined by splitting the elements in the steel plate and the glue into three parts in all directions, which means that one element became 27. This refinement was performed in the region surrounding the six holes closest to the horizontal symmetry line. This region was chosen based on the fact that it was known from analyses of the physical tests that the glue and the steel plate breaks somewhere in this region. The refinement of this region can be seen in Figures 5.7b and 5.8b. The mesh called refined 2 was refined in the same way, but instead of only refining a closed region of the glue and the steel, the full reach of the steel plate and the glue were refined.



(a) Coarse mesh.

(b) Refined 1 mesh.

Figure 5.7: Meshes of the full-scale model.

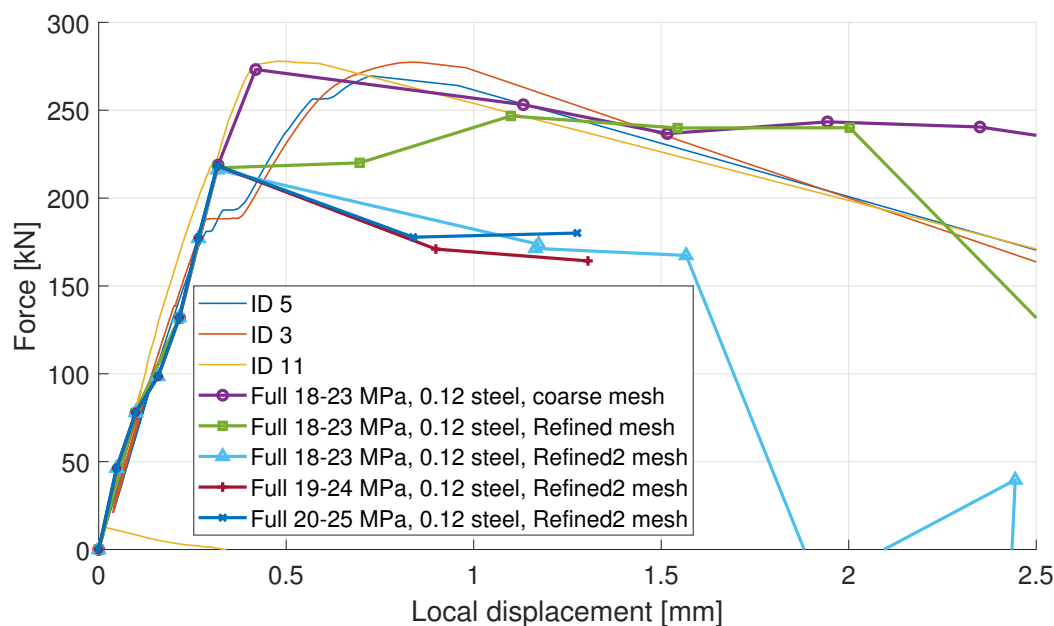


(a) Coarse mesh.

(b) Refined 1 mesh.

Figure 5.8: Meshes of the full-scale model.

From the simulation results with the different meshes presented in Figure 5.9, it can be observed that the mesh size in the glue and in the steel plate does not affect the elastic part of the response. However, it clearly affects the breaking point where the damage initiates, and the propagation of the crack, i.e. the damage evolution, which is reasonable since it is in this region the elements starts to get removed.

**Figure 5.9:** Simulation results for refined meshes compared to test results. Some simulations were not finished due to limitations in computational power.

Another thing that was observed when running the simulations where all the elements in the glue and the steel had been refined, was that fracture only occurred in the glue and not in the steel. This was because fracture occurred between the glue and the wood before any of the stresses got transferred from the glue to the steel. Hence, the steel did not get subjected to large enough stresses in order for damage to be initiated. The reason for this may be because the material model for the glue was too brittle, hence fracture occurred too quickly.

5. Full model

Another reason could simply be that the elements that were removed after failure still were too big. When removing an element from the model, the elements surrounding the removed element may be subjected to a small shock due to the quick removal of mass. This shock may lead to other elements reaching failure, causing them to be removed as well, and so on. In the model where only a chosen region had been refined this may not have been as big of an issue since the shock caused by the removal of the smaller elements, did not have as high impact on the larger elements. This could then result in a slower damage evolution throughout the glue, which means that the glue did not have time to entirely break before damage had been initiated in the steel plate. In other words, the steel plate breaks before the glue has completely broken itself.

In Figure 5.10, the fracture obtained when running the simulation where a chosen region of the mesh had been refined can be seen. As can be seen, the steel plate breaks before all of the glue have failed. Another thing that can be observed is that the steel plate in the simulation breaks in the same way as the steel plate in the physical tensile tests performed at RISE, i.e. in the line of holes closest to the symmetry line.

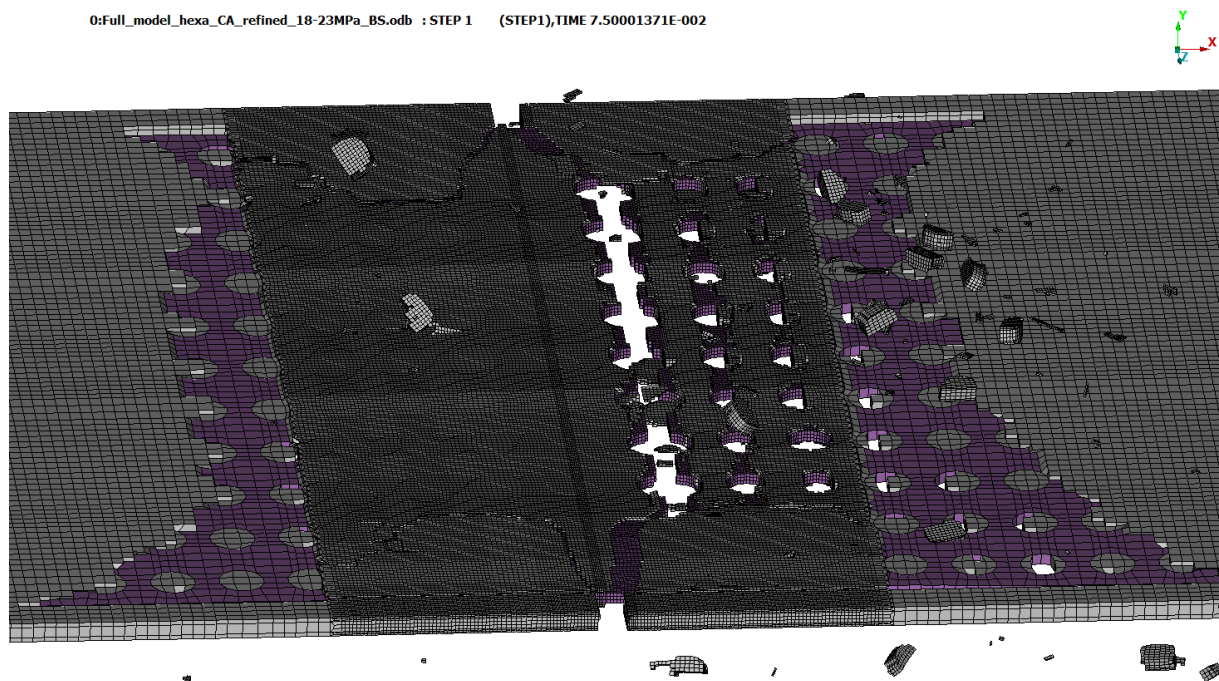


Figure 5.10: After fracture. Clearly shows where the mesh has been refined and how it affects the glue failure. In the refined zone, some glue remains after one layer breaks.

Thus, there still exists two insecurities in the full model: the material model of the glue, and the mesh size. In order to investigate this further, more physical tests would be required in order to be able to accurately capture the fracture of the glue as it behaves in reality. Also, when it comes to simulating the fracture using element deletion, a mesh convergence study would be preferable. Due to the time limitations all these tasks were considered to be future work.

6

Modified steel plate

Even though the FE-model still had some insecurities, it was decided that it could still be used to investigate potential improvements of the joint, by comparing the results between themselves. Since the real samples of the joint all breaks in the steel plate, the idea was to make the joint stronger by increasing the cross-sectional area of the steel plate around the fracture location. This is easiest done by reducing the number of holes in the steel plate. The ideal case would be to have the wood, the glue, and the steel break at the same time. Thus the tensile strength of the joint could possibly be increased without adding more material or extra features.

In order to investigate this further, two modified steel plates were modeled. The material and outer measurements were kept and only the hole pattern was changed. The simulations were performed with 18-23 MPa glue and all other previously calibrated parameters. In order to reduce the computational cost, vertical symmetry was used when creating the FE-models, using symmetry boundary conditions. Also, the coarser mesh was used for all the simulations, which may affect the accuracy of the results. Therefore, the results presented in this section should be studied with caution.

The number of holes was reduced in two different ways, Mod A and Mod B, where the latter has a lower number of holes. Schematic drawings of the modified steel plates are shown in Figure 6.1.

- **Original:** The original steel plate has equally spaced rows of equal holes.
- **Modification A:** Linearly less holes and linear distance increase between the rows.
- **Modification B:** Linearly even less holes and linear distance increase between the rows. Less rows.

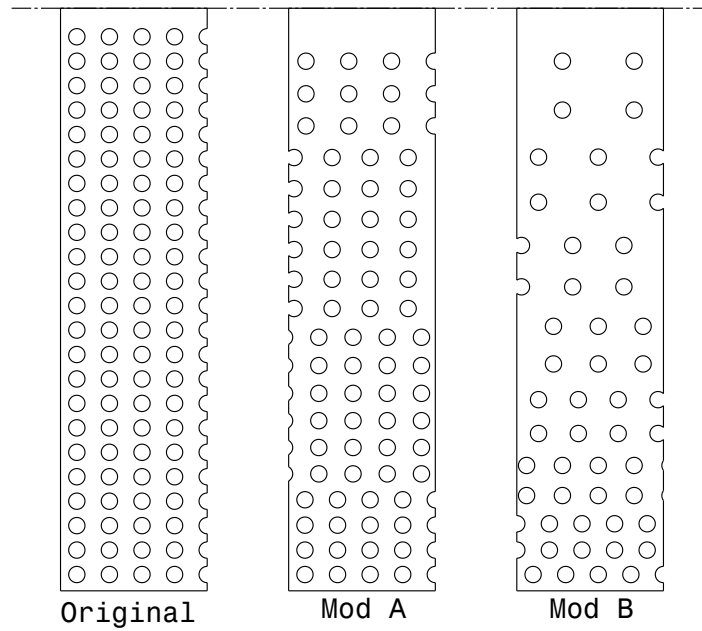


Figure 6.1: The different modifications of the hole density in the steel plate. The dot/dash-line represents the horizontal symmetry line of the model. Drawing shows only a section of the width of the plates.

6.1 Simulation results

In Figure 6.2, the results from the simulations with the different steel plates can be seen.

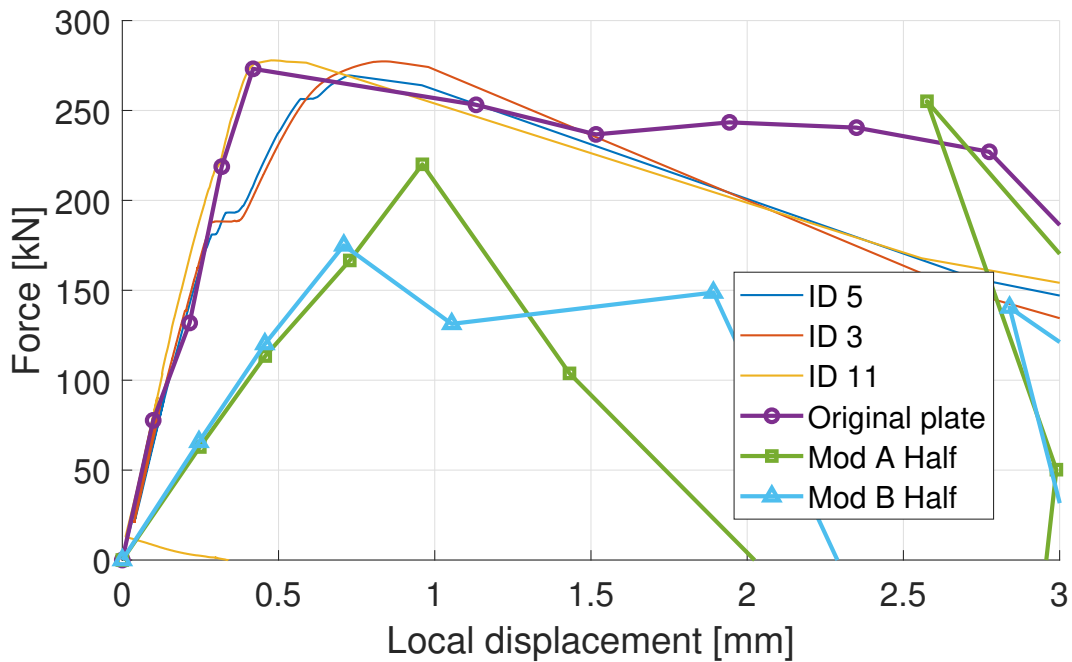


Figure 6.2: The different modifications of the hole density in the steel plate, compared to test data and simulation of the original.

The obtained results can be summarized as;

- **Original:** Breaks at the first row of holes closes to the horizontal symmetry line. Maximum load is 273 kN, and the steel reaches its ultimate tensile strength of 976 MPa.
- **Modification A:** Breaks only in the glue; the fracture in the glue initiates at the horizontal symmetry line and propagates to the middle of the plate, see Figure 6.3. Maximum load is 220 kN, and the stresses in the steel plate peaks at approximately 780 MPa.
- **Modification B:** Breaks only in glue; the fracture in the glue initiates at the horizontal symmetry line and propagates further than the middle of the plate, see Figure 6.4. Maximum load is 175 kN, and the stresses in the steel plate peaks at approximately 590 MPa.

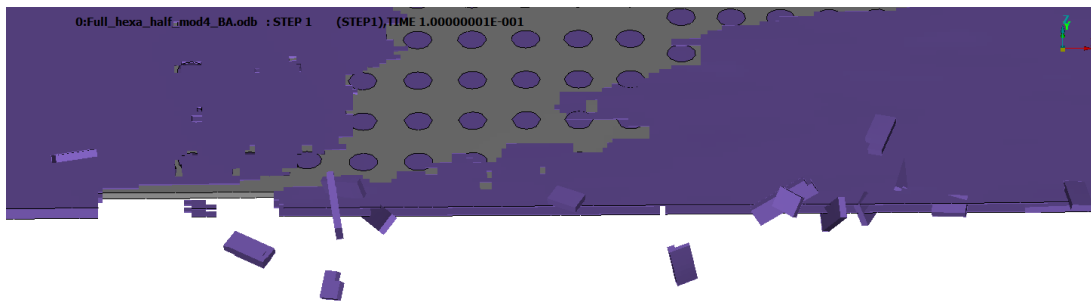


Figure 6.3: Modified plate A. Fracture in glue initiates at split line and propagates to the middle of the plate.



Figure 6.4: Modified plate B. Fracture in glue initiates at split line and propagates further than the middle of the plate.

The results clearly shows that with fewer holes, the entire glue between the wood and the steel plate breaks before the steel starts to yield. A reason for this may be that the glue has a decreased ability to grip on to the steel plate, since the number of glue anchors are reduced. Hence, instead of transferring stress to the steel thorough these anchors, the glue takes up a larger part of the stress by itself, which eventually leads to fracture. This would also explain the decrease in stress in the steel plate.

In Figure 6.5, the maximum loads are plotted against the area ratio, a , and the hole ratio, h , where it once again can be seen that fewer holes results in lower tensile strength of the joint. Although, this is far from enough data to determine the actual dependency curve for this effect, it is likely that the maximum is close to the original plate and that it goes down on the other side, i.e. when the number of holes are increased.

The ratios are calculated as:

$$a = \frac{A_{\text{tot}}}{A_{\text{remaining}}} \quad (6.1)$$

$$h = \frac{N_{\text{first row}}}{N_{\text{last row}}} \quad (6.2)$$

where

A_{tot} = Plate area before holes are stamped

$A_{\text{remaining}}$ = Plate area after holes are stamped

$N_{\text{first row}}$ = Number of holes in the row closest to the split line

$N_{\text{last row}}$ = Number of holes in the row farthest away from the split line

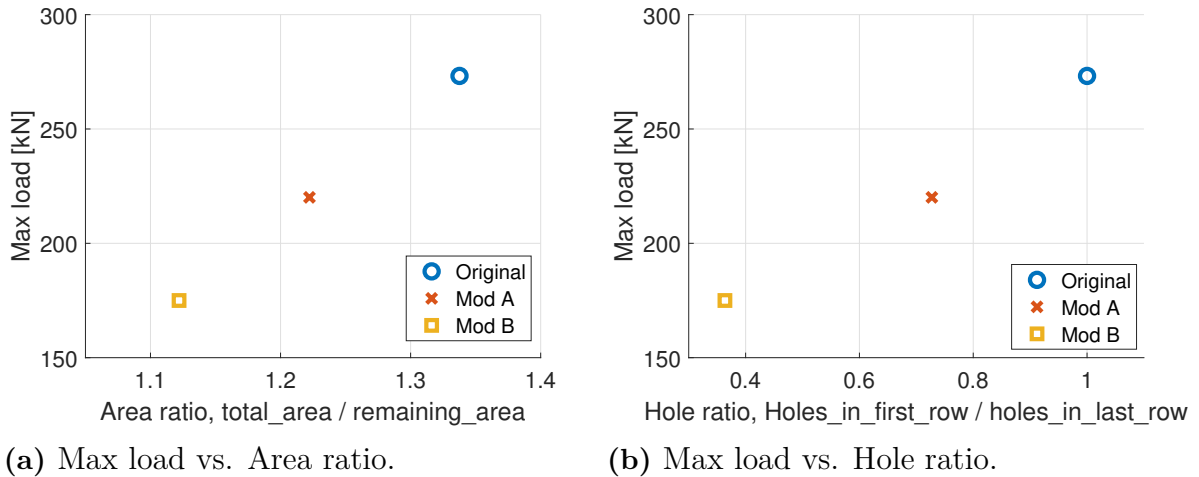


Figure 6.5: Simulated effects on maximum load dependent on Area ratio and Hole ratio.

6.1.1 Conclusion

The original plate is probably already quite close to the optimum hole pattern for this kind of joint. The designs proposed here with less holes are clearly not better. Though it should be kept in mind that none of these simulations should be fully trusted, since there still exists some insecurities. Some approximations have been made throughout this project, and it is unknown how far from reality these approximations are, without performing more analyses, both physical and simulations.

7

Conclusion

This thesis is merely the tip of the iceberg for the understanding of the mechanical behaviour inside this type of glue joint when it is subjected to pure tension. However, it can be used to give a beginning to the answer of the questions that were set up in the beginning of the project, which are listed in the introduction.

- **Is our model representative?**

By looking at Figure 5.9, it can be concluded that the FE-model is indeed representative in the elastic part of the response and close to the correct result also for the plastic region. From Figure 5.10, it can also be concluded that the correct fracture behaviour are somewhat captured since the steel plate breaks in the same manner for both the physical tests and the simulations. However, some insecurities still remain when it comes to the fracture mechanics, and further studies are required in order to resolve these issues. For example, element deletion needs to be studied further in order to correctly be able to simulate the fracture of the joint.

- **Are the material parameters provided by the company that develops the LVL representative?**

Based on the analyses of wood described in Section 3.3.1, combined with the simulations on the simplified and full model, it can be concluded that the values presented in the data sheet are accurate enough for this analysis. However, only test samples from a limited number of randomly selected panels have been used when performing the physical tests, which makes it difficult to draw any certain conclusions. Also, since most of the stresses are carried by the steel and the glue during tensile tests of the joint, the mechanical properties of the wood are not decisive for the result of the entire joint.

- **Where is the weak spot in the joint? What component of the joint fails first?**

As known from the physical tests, the joint breaks in the steel plate which can be seen in Figure 3.1, which is the same as for the simulations, see Figure 5.10. However the glue is not far ahead of the steel. When the steel is modified just a bit by reducing the number of holes, the glue fails before damage is initiated in the steel plate, as discussed in Section 5.3. In order to optimize the tensile strength of the joint, the glue and the steel plate needs to be optimized together, due to their dependency. Hence, both the glue and the steel plate are weak spots.

- **Is the design of the joint optimal? Why? How can it be improved?**

One type of modification has been performed by increasing the cross-sectional area of the steel plate where fracture occurs by reducing the number of holes, which did not show an improvement, as discussed in Section 6. Hence, it was concluded that the original steel plate is already quite close to the optimum for this kind of joint. However, this issue could maybe be resolved by changing the Loctite CR 421 Purbond to a stronger glue that may not need as many adhesive anchors in order to transfer the stress to the steel plate. Another thing that would be interesting to investigate is to see if the holes in the steel plate could be transformed in any way to favour an effective stress transfer between the glue and the steel.

- **Why are the results from Modvion's tests so good? Why is this a good joint?**

It is a very good joint that has probably already been optimized by its creators. The glue has good adhesion to the wood, and the poor adhesion to the steel has been solved by adding holes to the steel plate, enabling the glue to create adhesive anchors. Hence, the adhesive anchors created in the holes of the steel plate are critical for the joints performance, which also can be seen when looking at the results obtained with the modified steel plates in Section 6. From this it was concluded that when reducing the number of holes in the steel plate, i.e. when reducing the number of adhesive anchors in the joint, the glue fails entirely before damage is initiated in the steel plate.

7.1 Further work

With more time, knowledge and computational power, much more accurate simulations can be done in order to get deeper understanding of the mechanical behaviour of the joint. Listed below are some main areas which should be focused on in terms of future work.

- Make a mesh convergence study in order to reduce error caused by the element deletion. This requires lots of computational power.
- Make physical tests on the glue in order to develop and verify a better material model.
- Make physical tests on the interactions between glue/wood and glue/steel in both shear and tension. Also, analyze how different contacts may affect the fracture mechanics of the joint.
- Try out more hole patterns on the steel plate. Especially closer to the original design in order to find the optimum. Also see if there is any way to modify the steel plate in order to facilitate the stress transfer between the glue and the steel, since it is known that the steel can withstand higher loads than the glue.

7.2 Challenges

This project has been a challenging task in many ways. Due to limited prerequisites regarding the softwares, methods and tools used in this project, and with no natural learning source, a great part of the project time has been spent on learning how to use the softwares and understanding how the simulations behave. So, both time, knowledge, and computational power have been strong limiting factors in this project.

Bibliography

- [1] D. W. Green, J. E. Winandy, and D. E. Kretschmann, *Mechanical Properties of Wood, Chapter 4*. Forest Products Laboratory, United States Department of Agriculture, 1999. [Online]. Available: <https://www.fpl.fs.fed.us/documnts/fplgtr/fplgtr113/ch04.pdf>
- [2] Pollmeier. Baubuche - beech laminated veneer lumber - product profile. [Online]. Available: <https://www.pollmeier.com/en/downloads/brochures.html;jsessionid=B8A9EC59FB87C8FE093C6C84FEC8F987>
- [3] Wind-Turbine-Models, “Vensys 77/1500-Timber Tower,” 2018. [Online]. Available: <https://en.wind-turbine-models.com/turbines/560-vensys-77-1500-timber-tower>
- [4] K. Runesson and R. Larsson. Constitutive modeling of engineering materials - theory and computation. [Online]. Available: <https://pingpong.chalmers.se/courseId/9535/node.do?id=4641680&ts=1524689104594&u=-591277393>
- [5] Geomechanics Corner. The delicate matter of rock brittleness; part i: A rock mechanical perspective. [Online]. Available: <https://geomechanicscorner.com/2014/11/14/the-delicate-matter-of-rock-brittleness-part-i-a-rock-mechanical-perspective/>
- [6] Abaqus User’s Manual. Damage evolution and element removal for ductile metals. [Online]. Available: <https://abaqus-docs.mit.edu/2017/English/SIMACAEMATRefMap/simamat-c-damageevolductile.htm>
- [7] C. Harvey. (2018) CO₂ emissions reached an all-time high in 2018. [Online]. Available: <https://www.scientificamerican.com/article/co2-emissions-reached-an-all-time-high-in-2018/>
- [8] Acciona. (2018) Renewable energy. [Online]. Available: <https://www.acciona.com/renewable-energy/>
- [9] T. Puiu. (2012) First wooden wind turbine installed in germany is a lot more eco-friendly. [Online]. Available: <https://www.zmescience.com/research/timbertower-first-wood-turbine-04323/>
- [10] S. Hoff and J. DeVilbiss. (2017) Wind turbine heights and capacities have increased over the past decade. [Online]. Available: <https://www.eia.gov/todayinenergy/detail.php?id=33912>
- [11] L. Rodgers, “Climate change: The massive CO₂ emitter you may not know about,” 2018. [Online]. Available: <https://www.bbc.com/news/>

science-environment-46455844

- [12] Worldsteel Association, “Steel’s contribution to a low carbon future and climate resilient societies,” 2019. [Online]. Available: <https://www.worldsteel.org/publications/position-papers/steel-s-contribution-to-a-low-carbon-future.html>
- [13] A. Álvarez Canel and D. Fernández Cortizo, “Conceptual design and fe analysis of a clt wind turbine tower,” Master’s thesis, Chalmers University of Technology, 2016.
- [14] P. Steen, “Structural design of a wooden wind tower structure,” Master’s thesis, Chalmers University of Technology, 2017.
- [15] B. Jeleč, “Untersuchungen zugbeanspruchter faserparallel eingeklebter Bleche in Furnierschichtholz aus Buche,” Master’s thesis, Technischen Universität Graz, 2016. [Online]. Available: <https://diglib.tugraz.at/untersuchungen-zugbeanspruchter-faserparallel-eingeklebter-bleche-in-furnierschichtholz-aus-buche-2016>
- [16] HowStuffWorks. (2001) What is the difference between a hardwood and a softwood? [Online]. Available: <https://science.howstuffworks.com/life/genetic/question598.htm>
- [17] NZ Wood - For a better world. What is the difference between hardwood and softwood? [Online]. Available: <http://www.nzwood.co.nz/faqs/what-is-the-difference-between-hardwood-and-softwood/>
- [18] S. U. Mou. Difference between softwood and hardwood. [Online]. Available: <https://civiltoday.com/civil-engineering-materials/timber/150-difference-between-softwood-and-hardwood>
- [19] M. Johansson. Timber and engineered wood products. [Online]. Available: http://www.kstr.lth.se/fileadmin/kstr/pdf_files/Timber_Engineering_2017/Timber_and_engineered_wood_products.pdf
- [20] Metsä Wood, “What is Kerto LVL?” 2018. [Online]. Available: <https://www.metsawood.com/global/news-media/articles/Pages/what-is-Kerto.aspx>
- [21] —, “Kerto® LVL Q-panel DOP,” 2018, Declaration of performance NO. MW/LVL/312-001/CRP/DOP. [Online]. Available: <https://www.metsawood.com/global/Tools/DoP/Pages/DOPSearch.aspx?ReferenceCode=MW/LVL/312-001/CPR/DOP>
- [22] —, “Kerto® LVL Q-panel Datasheet,” 2018. [Online]. Available: <https://www.metsawood.com/global/Tools/MaterialArchive/MaterialArchive/MW-KertoLVL-Q-panel-datasheet-EN.pdf>
- [23] Ultralam LVL, “LVL Ultralam,” 2018. [Online]. Available: <http://ultralam.com/products/laminated-veneer-lumber-lvl/>
- [24] E. Karsh. (2014) Modern timber connections. [Online]. Available: <https://www.structuremag.org/?p=4061>
- [25] Timber Composite Technology. (2019) Hsk perforated steel sheets. [Online]. Available: <https://ticomtec.de/en/hsk-systems/holz-stahl-klebeverbundsystem/baustoffe-hsk/hsk-lochblech/>

-
- [26] Henkel & Cie AG, “LOCTITE CR 421 PURBOND,” 2017. [Online]. Available: <https://www.henkel-adhesives.com/us/en/industries/engineered-wood.html>
- [27] R. Caula, “Timbertower world’s first wooden wind turbine,” 2012. [Online]. Available: <https://www.designboom.com/technology/timber-tower-wooden-wind-turbine/>
- [28] BETA CAE Systems. (2019) ANSA. [Online]. Available: <https://www.beta-cae.com/ansa.htm>
- [29] Dassault Systèmes. (2019) Abaqus Unified FEA. [Online]. Available: <https://www.3ds.com/products-services/simulia/products/abaqus/>
- [30] Wikipedia. (2019) Abaqus Unified FEA. [Online]. Available: <https://en.wikipedia.org/wiki/Abaqus>
- [31] BETA CAE Systems. (2019) META. [Online]. Available: <https://www.beta-cae.com/meta.htm>
- [32] Abaqus Analysis User’s Manual. Linear elastic behaviour. [Online]. Available: <https://www.sharcnet.ca/Software/Abaqus610/Documentation/docs/v6.10/books/usb/default.htm?startat=pt05ch19s02abm02.html>
- [33] E. Borgqvist, “Elasto-plasticity in fem interpreted as a dae system,” Master’s thesis, Lund University, 2010. [Online]. Available: <http://www.solid.lth.se/fileadmin/hallfasthetslara/utbildning/examensarbete/TFHF5154.pdf>
- [34] Abaqus Theory Manual. Isotropic elasto-plasticity. [Online]. Available: <https://classes.engineering.wustl.edu/2009/spring/mase5513/abaqus/docs/v6.6/books/stm/default.htm?startat=ch04s03ath104.html>
- [35] K. E. Atkinson. Numerical analysis. [Online]. Available: <https://www.britannica.com/science/numerical-analysis#ref364052>
- [36] N. E. Dowling, *Mechanical Behaviour of Material - Engineering Methods for Deformation, Fracture and Fatigue*. Pearson Education, 2011. [Online]. Available: <https://www.goodreads.com/book/show/14857638-mechanical-behavior-of-materials-norman-e-dowling>
- [37] Abaqus User’s Manual. Explicit dynamic analysis. [Online]. Available: <https://www.sharcnet.ca/Software/Abaqus610/Documentation/docs/v6.10/books/usb/default.htm?startat=pt03ch06s03at08.html>
- [38] ——. Mass scaling. [Online]. Available: <https://www.sharcnet.ca/Software/Abaqus610/Documentation/docs/v6.10/books/usb/default.htm?startat=pt04ch11s07aus72.html>
- [39] ——. Damage initiation for ductile metals. [Online]. Available: <https://abaqus-docs.mit.edu/2017/English/SIMACAEMATRefMap/simamat-c-damageinitductile.htm>
- [40] SSAB, “Strenx 700,” 2017. [Online]. Available: <https://www.ssab.com/products/brands/strenx/products/strenx-700-mc>
- [41] Abaqus User’s Manual. Surface-based cohesive behavior. [Online]. Available: <https://www.sharcnet.ca/Software/Abaqus/6.14.2/v6.14/books/usb/default>

[htm?startat=pt09ch37s01alm63.html](#)

A

Appendix 1

A.1 Stress distributions

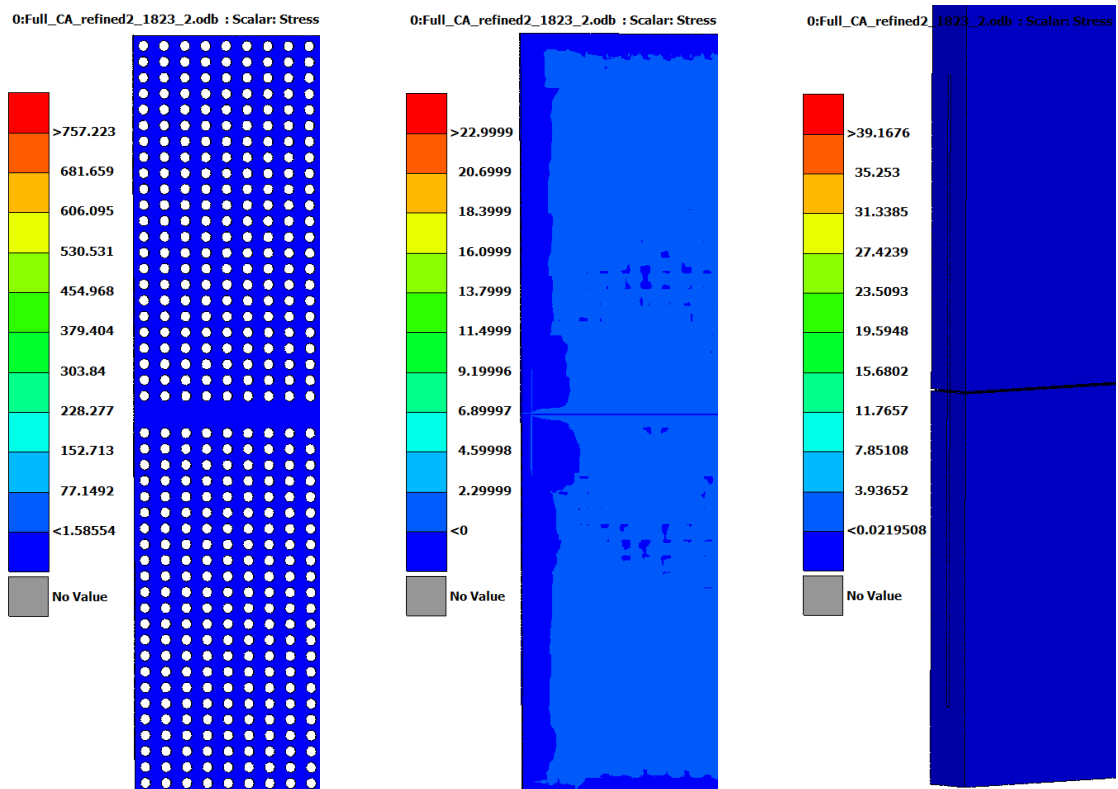


Figure A.1: Step 1

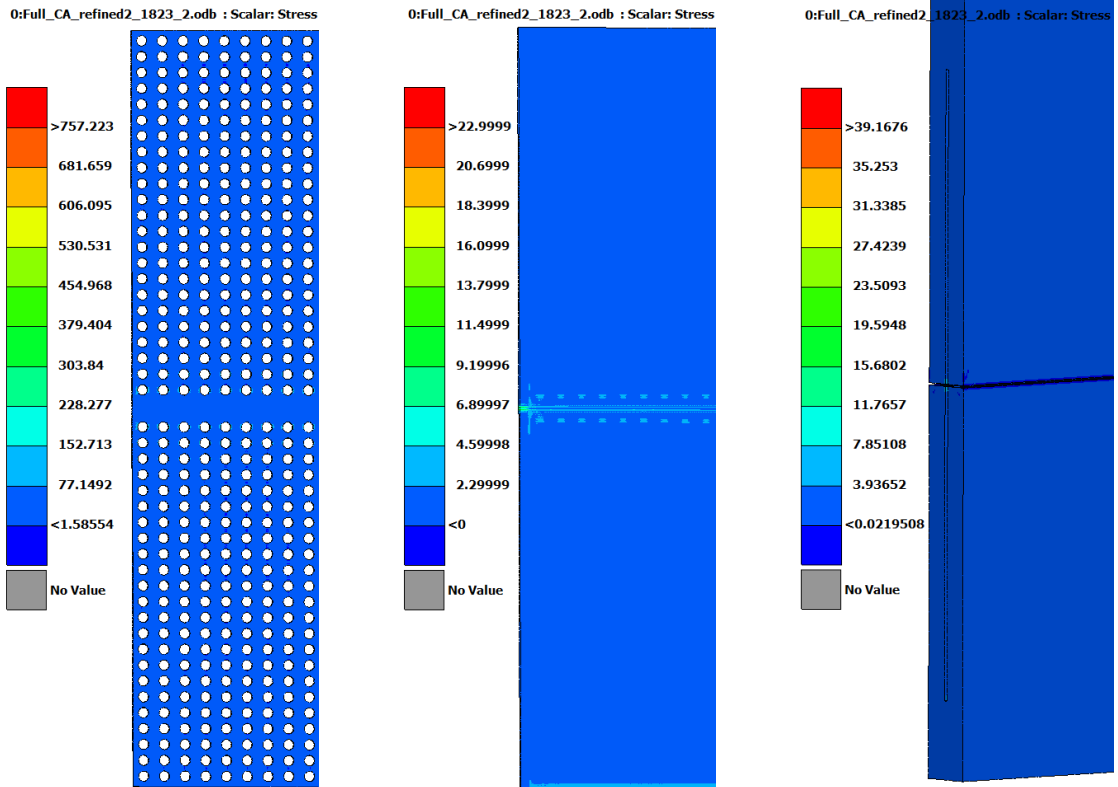


Figure A.2: Step 2

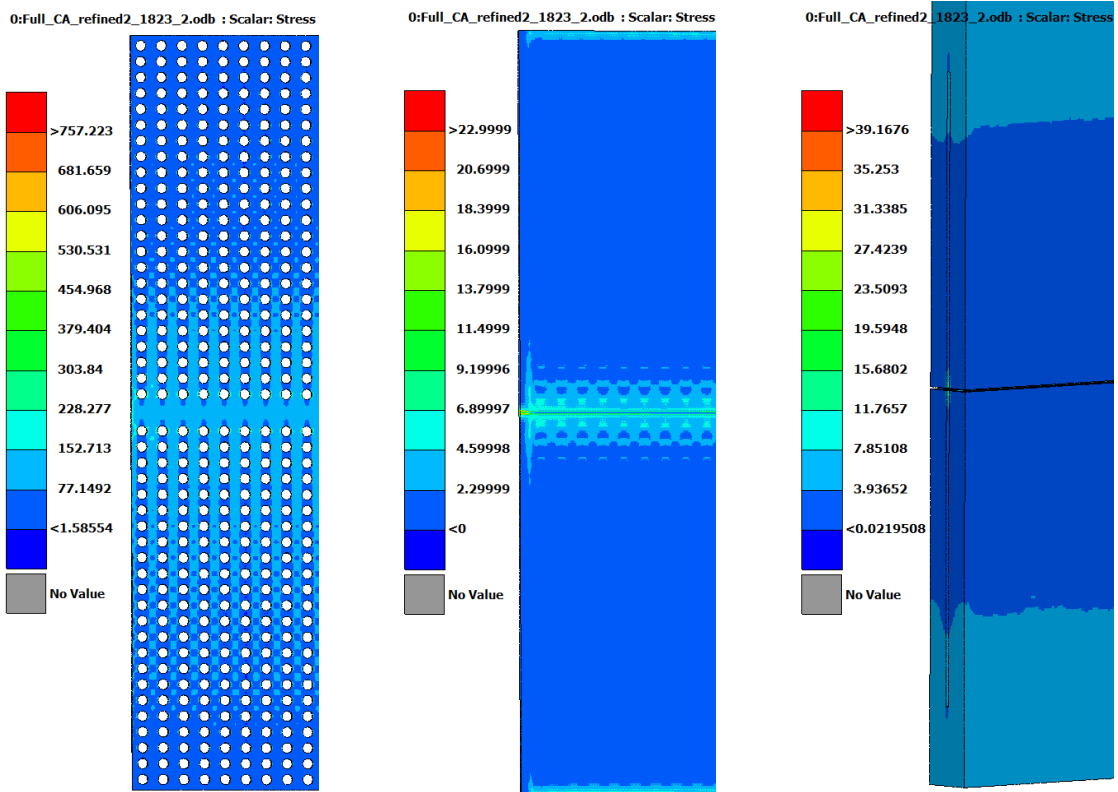


Figure A.3: Step 3

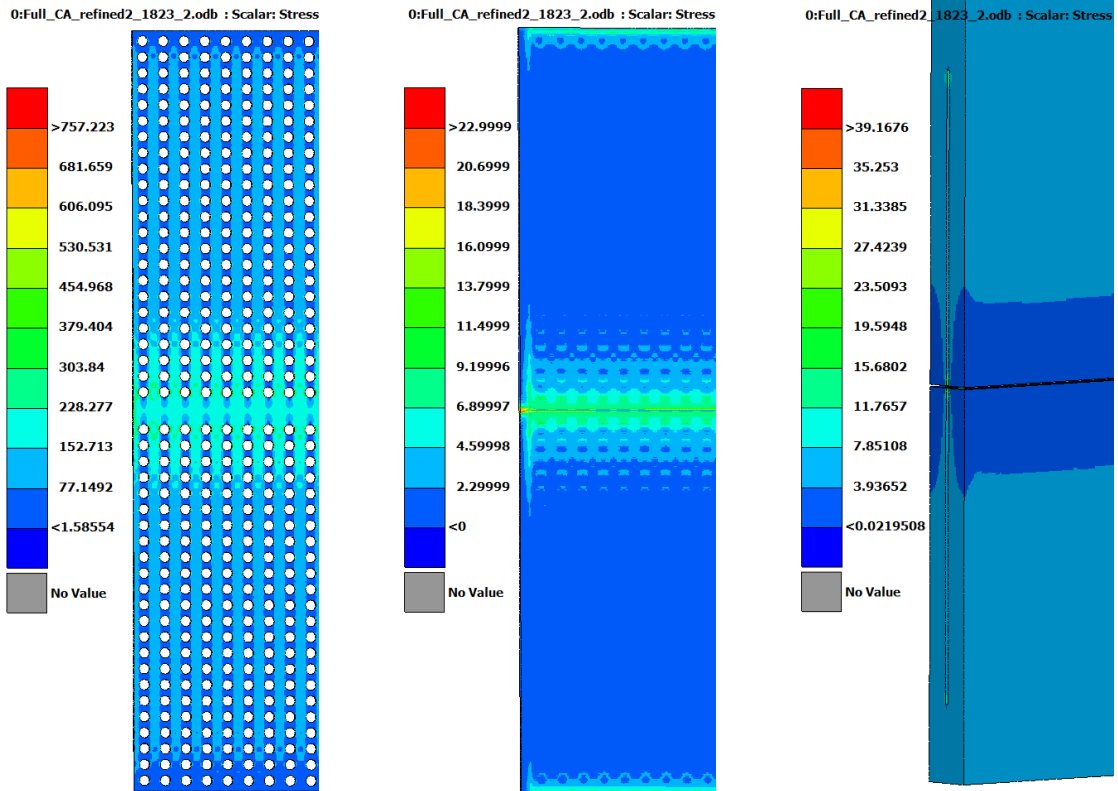


Figure A.4: Step 4

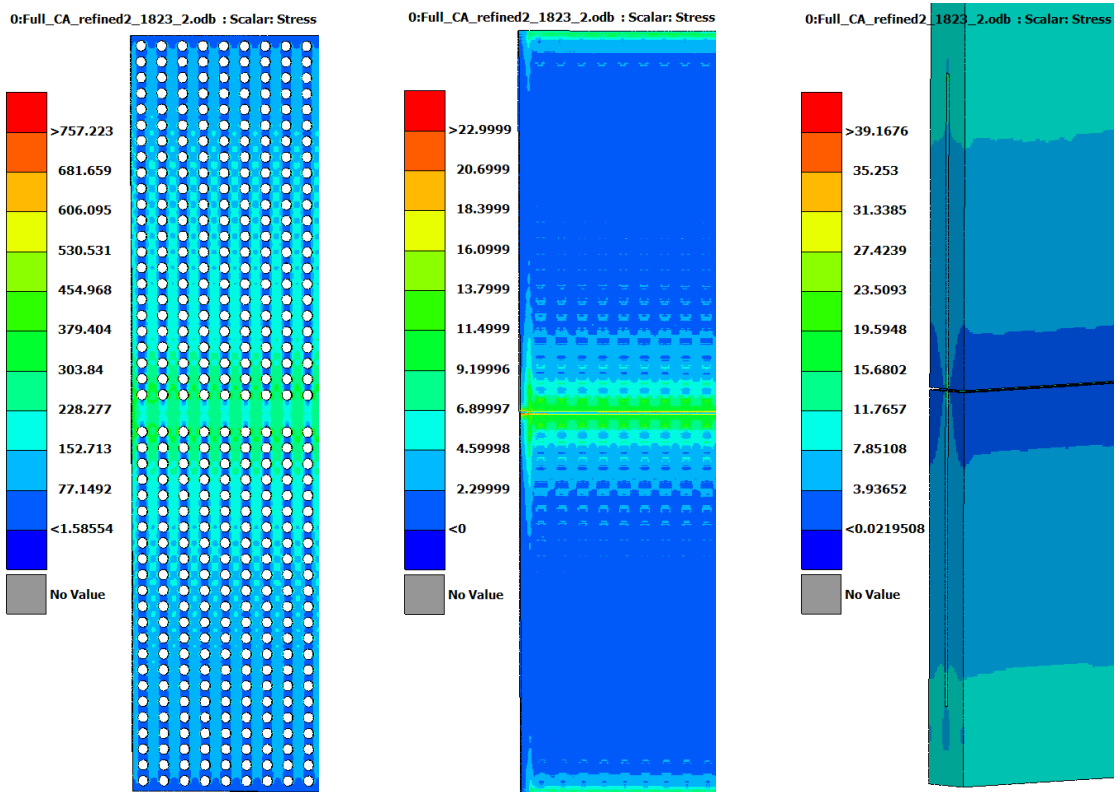


Figure A.5: Step 5

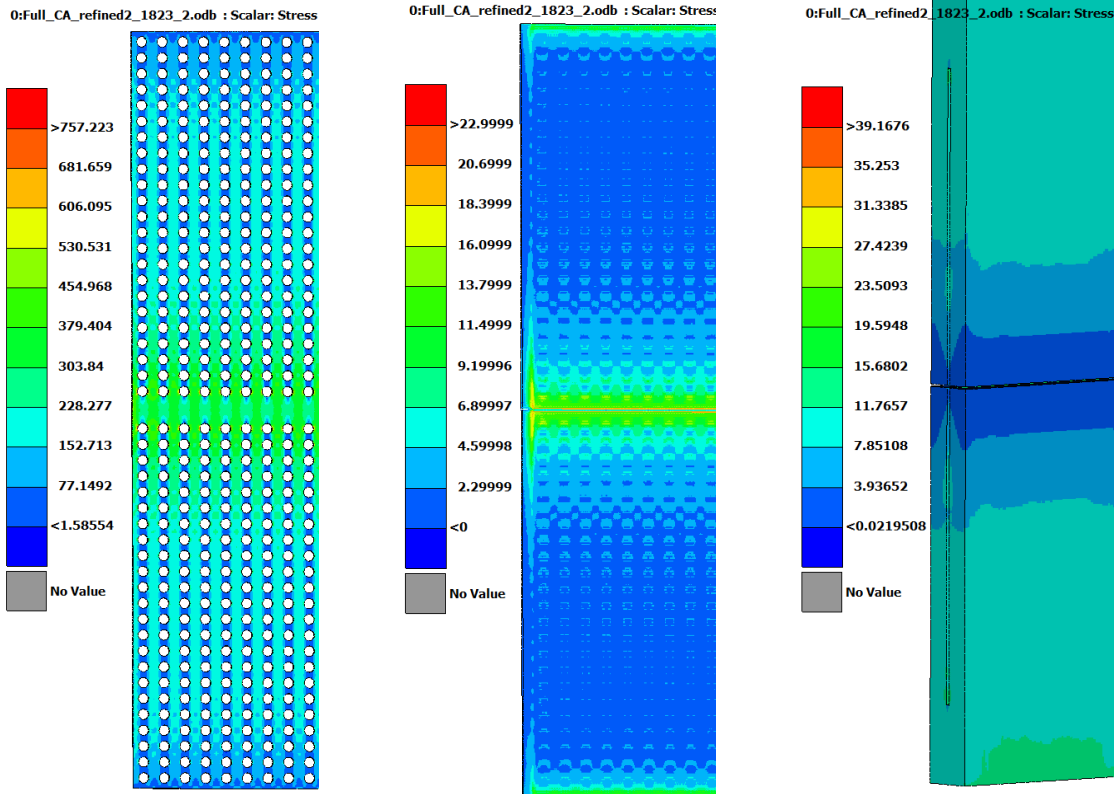


Figure A.6: Step 6

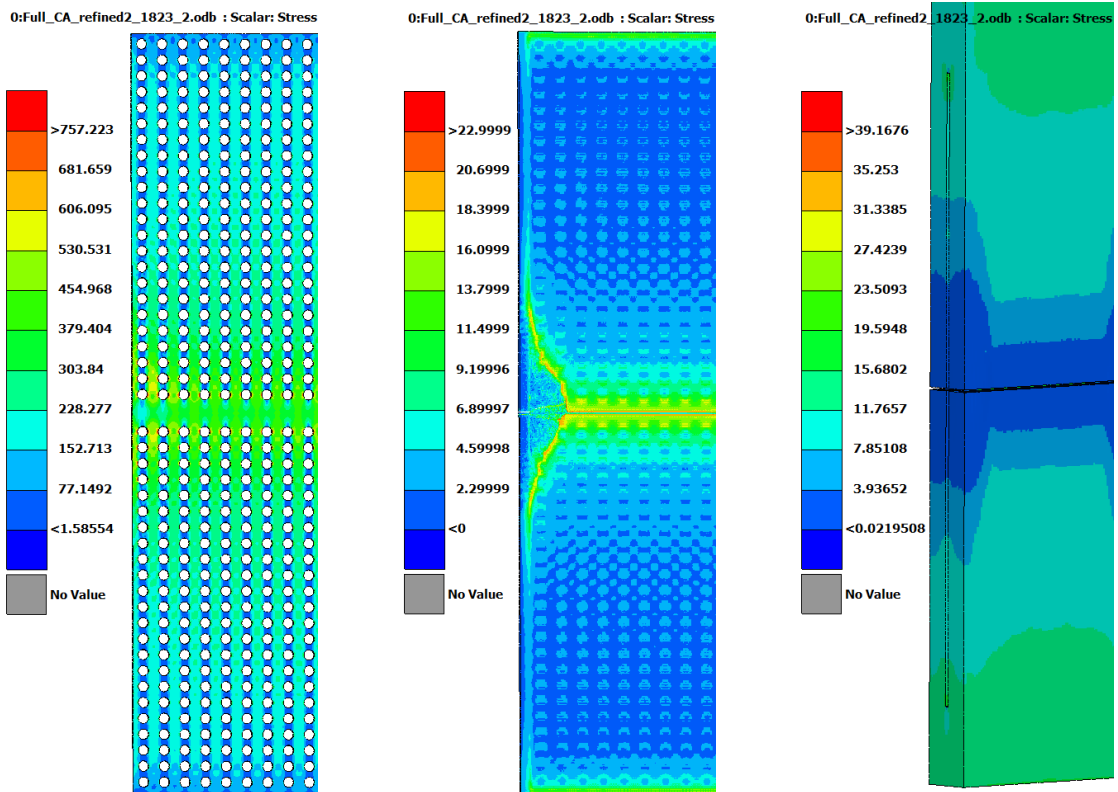


Figure A.7: Step 7

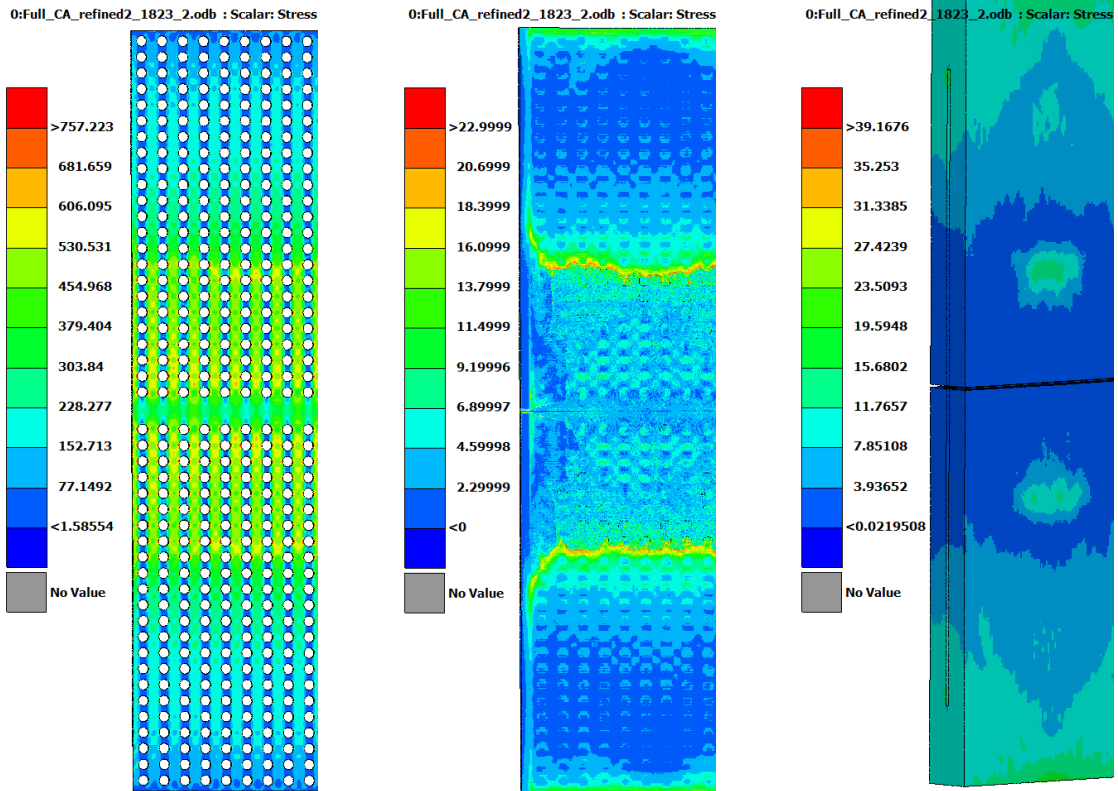


Figure A.8: Step 8

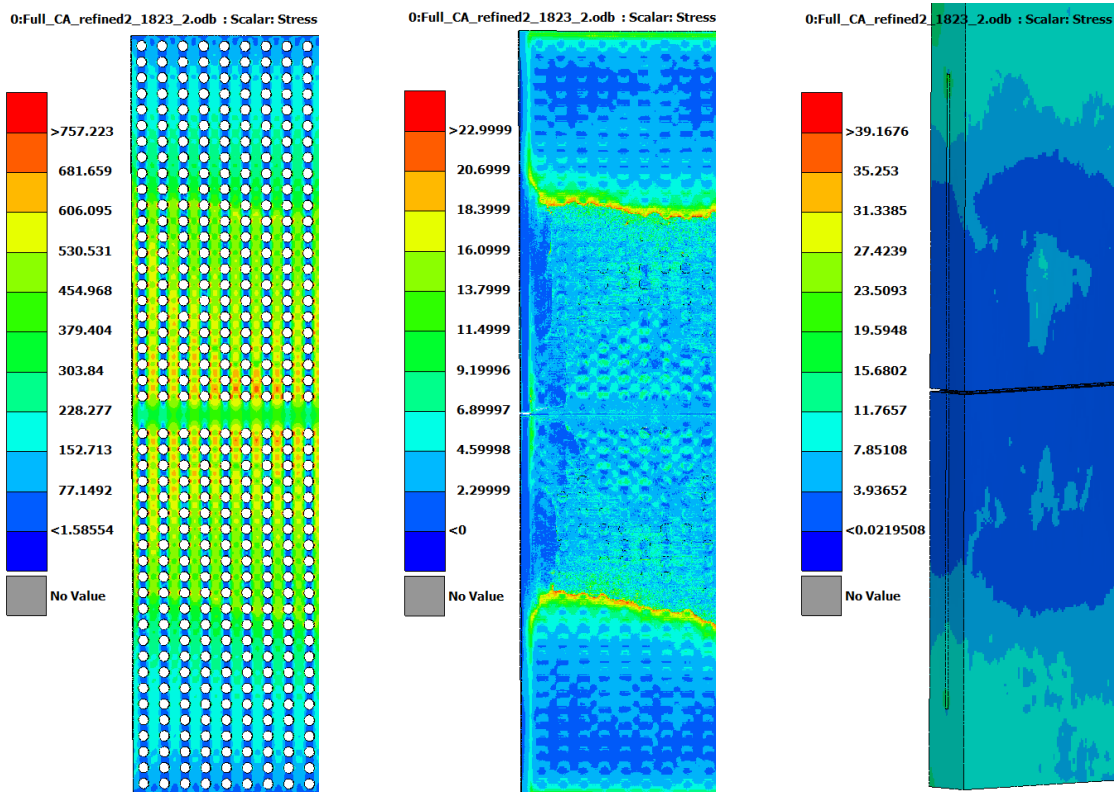


Figure A.9: Step 9

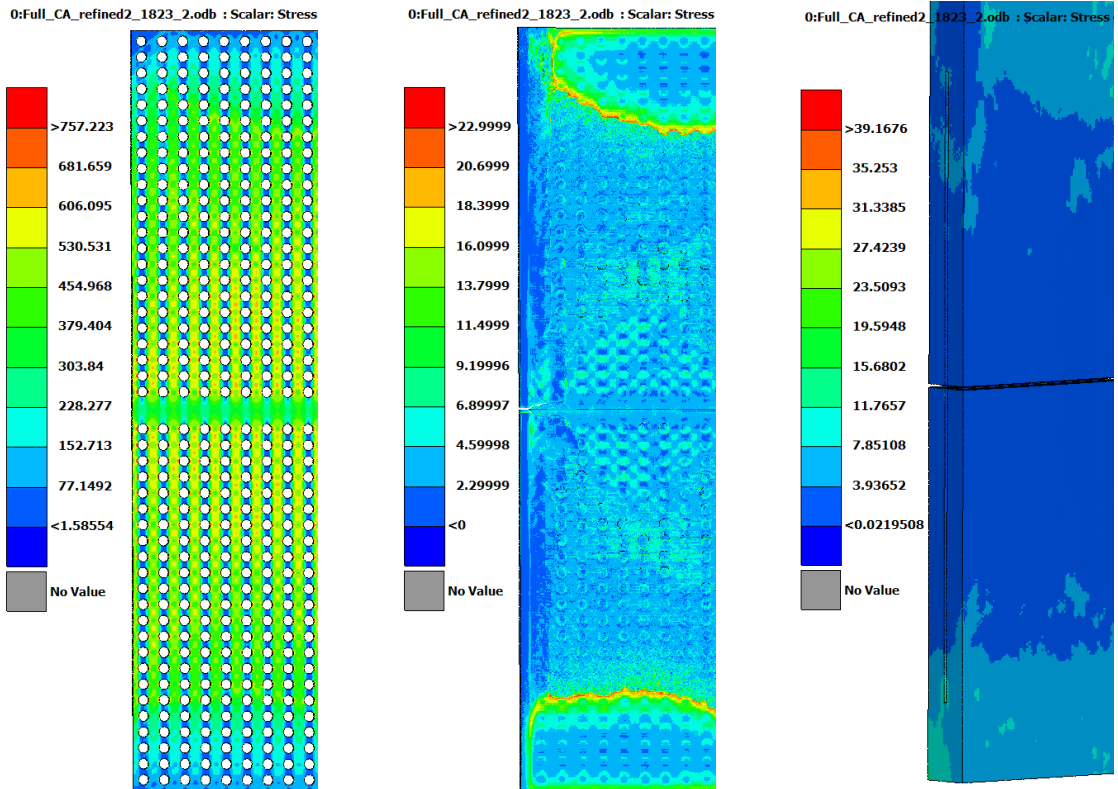


Figure A.10: Step 10

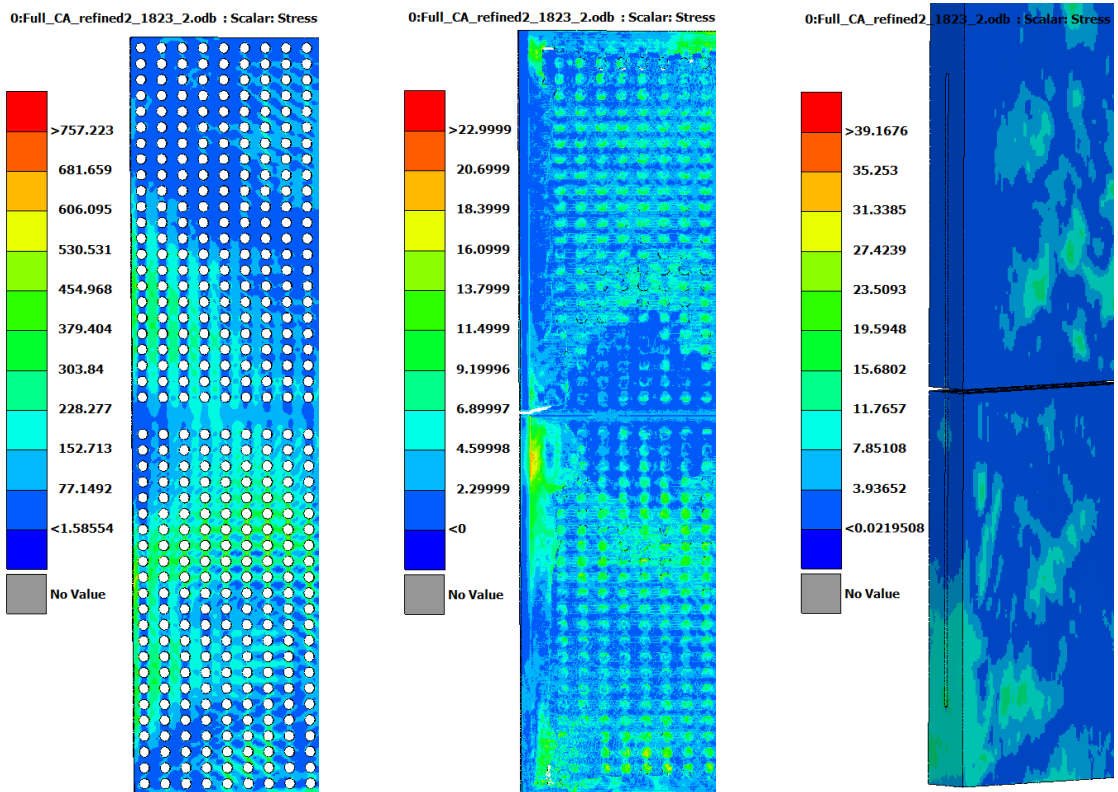


Figure A.11: Step 11

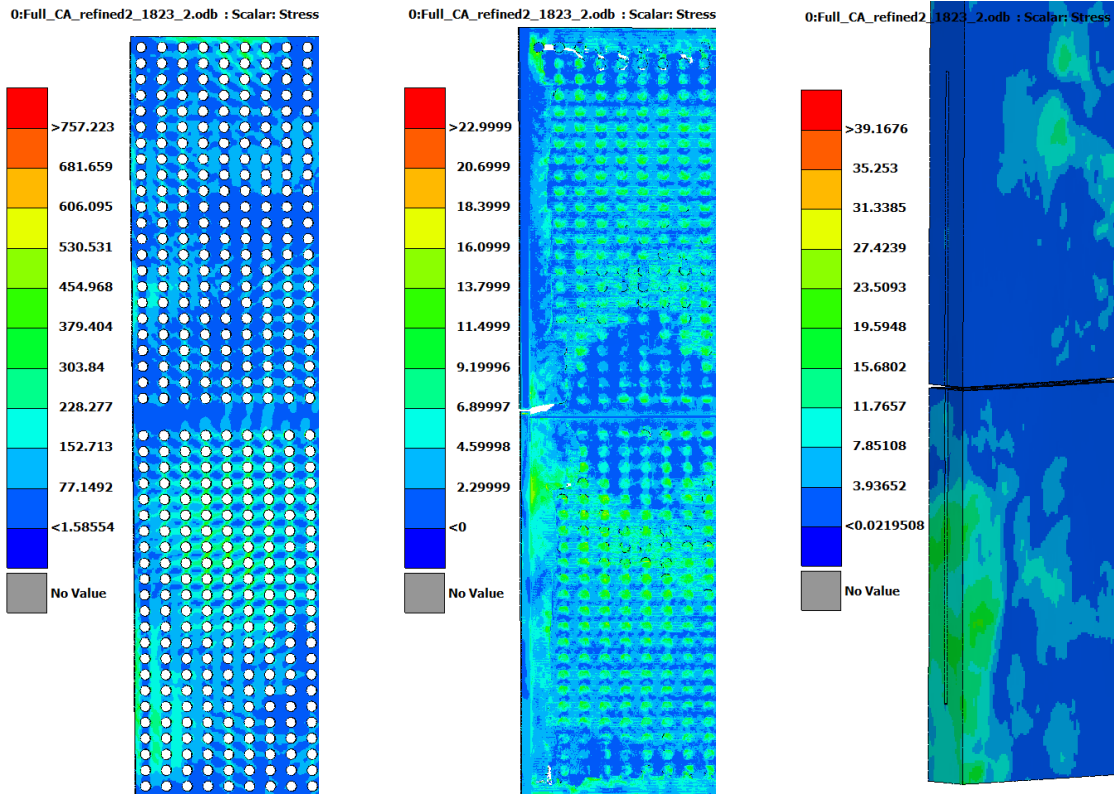


Figure A.12: Step 12

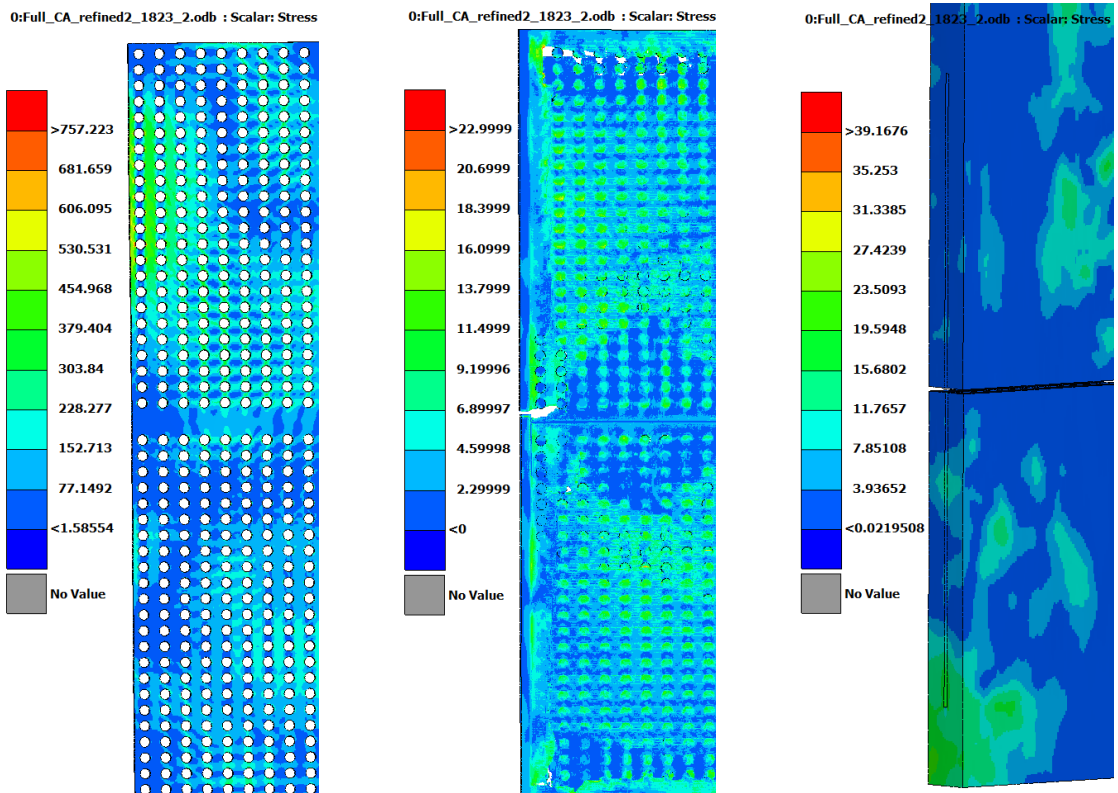


Figure A.13: Step 13